

The Pennsylvania State University  
The Graduate School  
College of Earth and Mineral Sciences

**MECHANISMS OF SINTERING AND SECOND PHASE  
FORMATION IN BAYER ALUMINA**

A Dissertation in  
Materials Science and Engineering  
by  
Tobias Frueh

© 2017 Tobias Frueh

Submitted in Partial Fulfillment  
of the Requirements  
for the Degree of

Doctor of Philosophy

September 2017

The dissertation of Tobias Frueh was reviewed and approved\* by the following:

Gary Messing

Distinguished Professor of Ceramic Science and Engineering

Thesis Advisor, Chair of Committee

James Adair

Professor of Materials Science and Engineering, Biomedical Engineering and  
Pharmacology

Optional Title Here

John Hellmann

Professor of Materials Science and Engineering

Associate Dean for Graduate Education and Research

Douglas Wolfe

Associate Professor of Materials Science and Engineering

Department Head, Advanced Coatings at the Applied Research Laboratory

Senior Scientist

\*Signatures are on file in the Graduate School.

# **Abstract**

# Table of Contents

<b>List of Figures</b>	<b>vii</b>
<b>List of Tables</b>	<b>xii</b>
<b>Acknowledgments</b>	<b>xiii</b>
<b>Chapter 1</b>	
<b>Introduction</b>	<b>1</b>
1.1 Motivation . . . . .	1
1.2 The Bayer Process . . . . .	2
1.3 Influence of Impurities and Dopants on the Sintering Behavior of Al <sub>2</sub> O <sub>3</sub> . . . . .	3
1.3.1 MgO in Al <sub>2</sub> O <sub>3</sub> . . . . .	3
1.3.2 Other Impurities in Al <sub>2</sub> O <sub>3</sub> . . . . .	4
1.3.3 Impurities in MgO-doped Al <sub>2</sub> O <sub>3</sub> . . . . .	5
1.3.4 Influence of Na <sub>2</sub> O and SiO <sub>2</sub> on the Sintering Behavior of Al <sub>2</sub> O <sub>3</sub> . . . . .	8
<b>Chapter 2</b>	
<b>The Effects of Na<sub>2</sub>O and SiO<sub>2</sub> on Liquid Phase Sintering of Bayer Al<sub>2</sub>O<sub>3</sub></b>	<b>14</b>
2.1 Introduction . . . . .	14
2.2 Experimental . . . . .	15
2.3 Results . . . . .	16
2.3.1 Effects of Na <sub>2</sub> O-doping . . . . .	16
2.3.2 Effects of Na <sub>2</sub> O/SiO <sub>2</sub> co-doping . . . . .	17
2.4 Discussion . . . . .	18
2.5 Summary . . . . .	23

<b>Chapter 3</b>	
<b>Powder Chemistry Effects on the Sintering Behavior of MgO-doped Bayer Alumina</b>	<b>36</b>
3.1 Introduction . . . . .	36
3.2 Experimental . . . . .	38
3.3 Computational Methodology . . . . .	39
3.4 Sintering and Microstructure Analysis . . . . .	41
3.5 Mechanistic Interpretation . . . . .	44
3.6 Summary and Conclusion . . . . .	49
<b>Chapter 4</b>	
<b>Dynamic development of nanometer scale grain boundaries during liquid phase sintering</b>	<b>66</b>
4.1 Introduction . . . . .	66
4.2 Experiment . . . . .	68
4.3 Grain boundary thickness in MgO-free alumina . . . . .	69
4.4 The equilibrium film thickness model . . . . .	71
4.5 Calculation of the theoretical Equilibrium Film Thicknesses . . . . .	72
4.6 High-resolution TEM . . . . .	76
4.7 The effect of changes in powder chemistry . . . . .	77
4.7.1 Na <sub>2</sub> O/SiO <sub>2</sub> ratio . . . . .	77
4.7.2 MgO-doped Bayer alumina . . . . .	78
4.8 Conclusion . . . . .	78
<b>Chapter 5</b>	
<b>Second phase formation in Bayer alumina</b>	<b>92</b>
5.1 Introduction . . . . .	92
5.2 Experimental . . . . .	94
5.3 Results . . . . .	94
5.3.1 Influence of MgO on the formation of $\beta$ -Al <sub>2</sub> O <sub>3</sub> . . . . .	95
5.3.2 MgO-doped Bayer alumina . . . . .	95
5.3.2.1 Number frequency of $\beta$ -Al <sub>2</sub> O <sub>3</sub> grains . . . . .	95
5.3.2.2 Size of $\beta$ -Al <sub>2</sub> O <sub>3</sub> grains . . . . .	96
5.3.3 Interpretation and mechanisms of formation . . . . .	97
5.4 Summary . . . . .	99
<b>Chapter 6</b>	
<b>A Critique of the Master Sintering Curve Analysis of Sintering Processes</b>	<b>111</b>
6.1 Introduction . . . . .	111

6.2	Experimental Procedure . . . . .	114
6.3	Results and Discussion . . . . .	116
6.3.1	The effect of forming on $Q$ . . . . .	116
6.3.2	MSC at high densities . . . . .	117
6.3.3	Quantification of the MSC shape . . . . .	118
6.3.4	Influence of powder chemistry . . . . .	119
6.3.5	Limitations of the MSC analysis . . . . .	119
6.3.6	Practical use of the MSC analysis . . . . .	121
6.4	Summary . . . . .	122
<b>Chapter 7</b>		
	<b>Summary and Future Work</b>	<b>135</b>
7.1	Introduction . . . . .	135
7.2	More Declaration . . . . .	135
<b>Bibliography</b>		<b>137</b>

# List of Figures

1.1	SIMS maps of $\text{Al}_2\text{O}_3$ doped with 500 ppm MgO (a) and 1000 ppm $\text{SiO}_2$ (b). Samples were sintered for 8 h at 1650°C [1]. . . . .	12
1.2	SIMS maps of $\text{Al}_2\text{O}_3$ co-doped with 500 ppm MgO and 1000 ppm $\text{SiO}_2$ and sintered at 1650°C for 8h. (a) shows the distribution of $\text{SiO}_2$ , (b) the distribution of MgO in the same samples [1]. . . . .	13
2.1	SEM image of as-received chemically purified Bayer $\text{Al}_2\text{O}_3$ powder used in this study. . . . .	27
2.2	Dilatometer curves of as-received and singly $\text{Na}_2\text{O}$ -doped samples heated at 10°C/min to 1525°C. . . . .	28
2.3	Densification kinetics of Bayer $\text{Al}_2\text{O}_3$ doped with different $\text{Na}_2\text{O}$ concentrations and sintered at 1525°C. . . . .	29
2.4	Microstructures of as-received and singly 529 ppm $\text{Na}_2\text{O}$ doped samples after 30 min, 3 h and 8 h at 1525°C. . . . .	30
2.5	Dilatometer curves of as-received, singly $\text{SiO}_2$ -doped, and $\text{Na}_2\text{O}/\text{SiO}_2$ -doped Bayer $\text{Al}_2\text{O}_3$ heated at 10°C/min to 1525°C. . . . .	31
2.6	Densification kinetics of Bayer $\text{Al}_2\text{O}_3$ doped with different concentrations of $\text{Na}_2\text{O}$ and $\text{SiO}_2$ at 1525°C. . . . .	32
2.7	Microstructures of Bayer $\text{Al}_2\text{O}_3$ doped with a) 603 ppm $\text{SiO}_2$ and b) 529 ppm $\text{Na}_2\text{O}$ and 603 ppm $\text{SiO}_2$ after heating at 1525°C for 8h.	33
2.8	Micrographs of a sample doped with 1029 ppm $\text{Na}_2\text{O}$ after sintering at 1525°C for 3 h. The micrographs were recorded using a) a secondary electron detector and b) a backscattered electron detector. The arrows point at the platelet shaped $\beta$ -alumina grains that form in samples doped with $\text{Na}_2\text{O}$ . The samples were not thermally etched.	34

2.9	Liquidus projection of the Al <sub>2</sub> O <sub>3</sub> -SiO <sub>2</sub> -Na <sub>2</sub> O ternary phase diagram. The red solid lines are isoplethal cuts representing the samples investigated in this study. The red dashed line is the 1525°C isotherm where α-Al <sub>2</sub> O <sub>3</sub> and liquid are in equilibrium. The blue dash-dot line and green dotted line are eutectic lines at which α-Al <sub>2</sub> O <sub>3</sub> and liquid is in equilibrium with β-Al <sub>2</sub> O <sub>3</sub> or mullite, respectively. . . . .	35
3.1	SEM image of 380 ppm MgO-doped specialty alumina powder used in this work. . . . .	54
3.2	Dilatometer curves of a) 380 ppm MgO-doped and b) MgO-free [2] specialty alumina samples with different Na <sub>2</sub> O/SiO <sub>2</sub> levels heated at 10°C/min to 1525°C. . . . .	55
3.3	Densification kinetics of specialty processed alumina containing different amounts Na <sub>2</sub> O and SiO <sub>2</sub> and a) 380 ppm MgO sintered at 1450°C, b) 380 ppm MgO sintered at 1525°C, and c) 2 ppm MgO sintered at 1525°C [2]. . . . .	56
3.4	Microstructures of 380 ppm MgO-doped specialty alumina samples with different Na <sub>2</sub> O and SiO <sub>2</sub> concentrations sintered at 1525°C for 8 h. . . . .	57
3.5	Sintering trajectories (grain size vs. relative density) for 380 ppm MgO-doped specialty alumina samples with different Na <sub>2</sub> O and SiO <sub>2</sub> concentrations. . . . .	58
3.6	Grain boundary of a sample containing 529 ppm Na <sub>2</sub> O, 603 ppm SiO <sub>2</sub> , and 2 ppm MgO after 3 h at 1525°C. . . . .	59
3.7	Grain boundaries of samples containing 560 ppm Na <sub>2</sub> O, 582 ppm SiO <sub>2</sub> , and 380 ppm MgO after a) 0 h and b) 3 h at 1525°C. . . . .	60
3.8	EDS of grain boundaries of samples containing 560 ppm Na <sub>2</sub> O, 582 ppm SiO <sub>2</sub> , and 380 ppm MgO after a) 0 h and b) 3 h at 1525°C showing the Si distribution. After 0 h Si shows a stronger segregation to the grain boundaries than after 3 h. . . . .	61
3.9	EDS line scan across a grain boundary of a sample containing 560 ppm Na <sub>2</sub> O, 582 ppm SiO <sub>2</sub> , and 380 ppm MgO after sintering at 1525°C for a) 0 h and b) 3 h. . . . .	62
3.10	Comparison of the formation energy of alpha-Al <sub>2</sub> O <sub>3</sub> with an Mg-cluster ( $E_{Form}^{Mg}$ ), Si-cluster ( $E_{Form}^{Si}$ ) and Mg+Si-cluster ( $E_{Form}^{Mg+Si}$ ) as a function of temperature. The formation energy difference ( $\Delta E_{Form}$ ) between the structures was calculated from Eq. REF to compare the formation energy values and show that it is energetically favorable to form Mg+Si-clusters over Si-clusters and Mg-clusters. . . . .	63

3.11	EDS maps of different oxides in 380 ppm MgO-doped specialty alumina samples after sintering at 1525°C for a-d) 0 h and e-h) 3 h.	64
3.12	Na <sub>2</sub> O concentration (ICP measurements) of 380 ppm MgO-doped specialty alumina samples with 560 ppm Na <sub>2</sub> O as a) function of sintering temperature and b) as a function of sintering time at 1525 °C. . . . .	65
4.1	Increase in concentration of liquid phase as a function of temperature for MgO-free powder samples with 529 ppm Na <sub>2</sub> O and different SiO <sub>2</sub> concentrations. . . . .	80
4.2	Relative density as a function of temperature and hold time determined from dilatometry for MgO-free powder samples with 529 ppm Na <sub>2</sub> O and different SiO <sub>2</sub> concentrations. . . . .	81
4.3	Liquid phase concentration as a function of relative density for MgO-free powder samples with 529 ppm Na <sub>2</sub> O and different SiO <sub>2</sub> concentrations. . . . .	82
4.4	Grain size - density trajectories as a function of Na <sub>2</sub> O and SiO <sub>2</sub> concentration for MgO-free alumina. . . . .	83
4.5	Change in Na/Al ion ratio in the liquid phase during sintering of samples with Na <sub>2</sub> O/SiO <sub>2</sub> ratios > 0.5. . . . .	84
4.6	Development of the electrostatic potential as a function of relative density. For MgO-free powder samples with 529 ppm Na <sub>2</sub> O and different SiO <sub>2</sub> concentrations. . . . .	85
4.7	Contributions to the equilibrium film thickness as a function of film thickness for MgO-free powder samples with 529/603 ppm Na <sub>2</sub> O/SiO <sub>2</sub> at a relative density of 93%. . . . .	86
4.8	Calculated equilibrium film thickness for MgO-free powder samples at different chemistries as a function of relative density. . . . .	87
4.9	Calculated grain boundary thicknesses as a function of relative density for MgO-free powder samples. The trajectories labeled with 529/603 ppm Na <sub>2</sub> O/SiO <sub>2</sub> , 529/203 ppm Na <sub>2</sub> O/SiO <sub>2</sub> , and 529 ppm Na <sub>2</sub> O/SiO <sub>2</sub> were calculated based on the liquid phase concentration and sintering stage. The equilibrium film thickness was calculated based on Clarke's model. The calculated grain boundary thicknesses are compared to measured grain boundary thicknesses (data points a: 1000/1000 ppm Na <sub>2</sub> O/SiO <sub>2</sub> , b) 529/603 ppm Na <sub>2</sub> O/SiO <sub>2</sub> , c) 529/203 ppm Na <sub>2</sub> O/SiO <sub>2</sub> after heating at 1525°C for 3 h). . . . .	88
4.10	TEM images of MgO-free powder samples with a) 529/203 ppm Na <sub>2</sub> /SiO <sub>2</sub> , b) 529/603 ppm Na <sub>2</sub> /SiO <sub>2</sub> , c) 1000/1000 ppm Na <sub>2</sub> /SiO <sub>2</sub> , and d) 29/103 ppm Na <sub>2</sub> /SiO <sub>2</sub> after sintering at 1525°C for 3 h. . . . .	89

4.11	TEM image of a MgO-free powder sample with 29/603 ppm Na <sub>2</sub> O/SiO <sub>2</sub> .	90
4.12	TEM images of MgO-doped (380 ppm) powder samples with a) 60/82 ppm Na <sub>2</sub> O/SiO <sub>2</sub> , b) 60/582 ppm Na <sub>2</sub> O/SiO <sub>2</sub> , and c) 560/582 ppm Na <sub>2</sub> O/SiO <sub>2</sub> . After heating at 1525°C for 3 h. . . . .	91
5.1	SEM micrographs of $\beta$ -Al <sub>2</sub> O <sub>3</sub> grains in a-c) Bayer alumina with 560 ppm Na <sub>2</sub> O, 82 ppm SiO <sub>2</sub> , and 380 ppm MgO after 3 h at 1525°C and d) Bayer alumina with 29 ppm Na <sub>2</sub> O, 103 ppm SiO <sub>2</sub> , and 502 ppm MgO after 3 h at 1525°C. The samples in a) and b) were not etched and the samples in c) and d) were etched. a), c), and d) were obtained using a secondary electron detector, and b) was obtained using a backscattered electron detector. . . . .	101
5.2	Formation of $\beta$ -Al <sub>2</sub> O <sub>3</sub> in MgO-free powder samples as a function of a) MgO concentration and b) Na <sub>2</sub> O concentration in samples after 3 h at 1525°C. . . . .	102
5.3	Formation of $\beta$ -Al <sub>2</sub> O <sub>3</sub> a function of a) Na <sub>2</sub> O concentration, b) SiO <sub>2</sub> concentration for different Na <sub>2</sub> O concentrations, and c) of the Na <sub>2</sub> O/SiO <sub>2</sub> ratio in MgO-doped (380 ppm) powder samples. In c) the black diamonds are samples with 82 ppm SiO <sub>2</sub> and the blue squares are samples with 182 and 582 ppm SiO <sub>2</sub> . . . . .	103
5.4	Kinetics of $\beta$ -Al <sub>2</sub> O <sub>3</sub> formation for different powder chemistries of MgO-doped powder samples (380 ppm MgO). . . . .	104
5.5	Micrographs showing $\beta$ -Al <sub>2</sub> O <sub>3</sub> grains (red circles) in Bayer alumina samples with a) 1000 ppm MgO, 1000 ppm SiO <sub>2</sub> , 29 ppm Na <sub>2</sub> O, b) 2 ppm MgO, 1000 ppm SiO <sub>2</sub> , 1000 ppm Na <sub>2</sub> O, c) 1000 ppm MgO, 1000 ppm SiO <sub>2</sub> , 1000 ppm Na <sub>2</sub> O after 3 h at 1525°C. . . . .	105
5.6	Micrographs showing $\beta$ -Al <sub>2</sub> O <sub>3</sub> grains (red circles) in MgO-doped (380 ppm) Bayer alumina samples with 82 ppm SiO <sub>2</sub> and a) 185 ppm Na <sub>2</sub> O, b) 560 ppm Na <sub>2</sub> O, and c) 1060 ppm Na <sub>2</sub> O after sintering at 1525°C for 3 h. . . . .	106
5.7	Micrographs showing $\beta$ -Al <sub>2</sub> O <sub>3</sub> grains (red circles) in MgO-doped (380 ppm) Bayer alumina samples with a) 185/182 ppm Na <sub>2</sub> O/SiO <sub>2</sub> and b) 560/182 ppm Na <sub>2</sub> O/SiO <sub>2</sub> after sintering at 1525°C for 3 h. .	107
5.8	Micrographs showing $\beta$ -Al <sub>2</sub> O <sub>3</sub> grains (red circles) in MgO-doped (380 ppm) Bayer alumina samples with 82 ppm SiO <sub>2</sub> and 560 ppm Na <sub>2</sub> O after sintering at 1525°C for a) 0 h, b) 1 h, and c) 8 h. . . .	108
5.9	XRD pattern of a sample with 1060 ppm Na <sub>2</sub> O, 82 ppm SiO <sub>2</sub> , and 380 ppm MgO after sintering at 1525°C for 5 h. The red arrows indicate the peaks that can be assigned to $\beta$ -Al <sub>2</sub> O <sub>3</sub> . The other peaks can be assigned to $\alpha$ -Al <sub>2</sub> O <sub>3</sub> . . . . .	109

5.10	Micrograph showing $\beta$ -Al <sub>2</sub> O <sub>3</sub> grains (red circles) in an ultra high purity powder sample with 502 ppm Na <sub>2</sub> O, 2 ppm MgO, and 11 ppm SiO <sub>2</sub> after sintering at 1525°C for 0 h . . . . .	110
6.1	Dilatometry curves of non-aqueous slip cast CT3000LS-SG samples heated at a) 5°C/min, b) 10°C/min, and c) 20°C/min to 1525°C measured parallel to (z-direction) and perpendicular to (x/y-direction) the capillary force acting during slip casting. . . . .	124
6.2	Development of the shrinkage anisotropy factor for shrinkage, $k$ , during densification of non-aqueous slip cast samples as a function of relative density for CT3000LS-SG samples heated at different rates. . . . .	125
6.3	Development of the relative density corrected for shrinkage anisotropy as a function of temperature for non-aqueous slip cast CT3000LS-SG samples heated at different rates. . . . .	126
6.4	Mean residuals of the MSC curves assuming different values for $Q$ for non-aqueous slip cast CT3000LS-SG samples. . . . .	127
6.5	MSC curves of CT3000LS-SG samples prepared by non-aqueous slip casting using a) the $Q$ -value obtained by accounting for shrinkage anisotropy ( $Q=550$ kJ/mol) and b) using $Q$ -value when shrinkage anisotropy was uncorrected for ( $Q = 625$ kJ/mol). . . . .	128
6.6	MSC curves and $Q$ -values of CT3000LS-SG samples obtained from the minimum mean residuals for samples prepared by different forming techniques and accounting for shrinkage anisotropy. . . . .	129
6.7	Densification of dry pressed CT3000LS-SG samples at different heating rates, b) mean residuals as a function of $Q$ , and c) MSC for $Q = 700$ kJ/mol obtained from the minimum mean residuals, showing divergence at densities >90%. . . . .	130
6.8	$Q$ -values for dry pressed CT3000LS-SG samples as a function of relative density obtained from iso-density analysis. . . . .	131
6.9	Development of the microstructural parameters, summarized in the $C$ parameter, as a function of relative density for a dry pressed CT3000LS-SG sample. . . . .	132
6.10	MSCs and $Q$ -values for CT3000LS-SG samples prepared by non-aqueous slip casting with different Na <sub>2</sub> O concentrations. . . . .	133
6.11	Equivalent time/temperature diagram for CT3000LS-SG samples prepared by non-aqueous slip casting heated at 10°C/min. The contours may be used to predict heat treatments requirements to achieve a desired density. . . . .	134

# List of Tables

2.1	Physical and chemical characteristics of the as-received Bayer Al <sub>2</sub> O <sub>3</sub> powder used in this study. . . . .	25
2.2	Calculated compositions and amounts of liquid in as-received, singly doped and co-doped samples at 1525°C ( $\alpha = \alpha\text{-Al}_2\text{O}_3$ , $\beta = \beta\text{-Al}_2\text{O}_3$ , L = liquid, M = mullite). . . . .	26
3.1	Physical and chemical characteristics of the as-received 380 ppm MgO-doped specialty alumina powder used in this study. . . . .	51
3.2	Calculated compositions and amounts of liquid in 380 ppm MgO-doped specialty alumina samples of different chemistries at 1450°C and 1525 °C. . . . .	52
3.3	Lattice parameters and equilibrium energy ( $E_0$ ) compared to previous first-principles and experimental values. . . . .	53
5.1	Estimated amount of $\beta\text{-Al}_2\text{O}_3$ in MgO-doped (380 ppm) Bayer alumina samples after 3 h at 1525°C. . . . .	100
6.1	$Q$ values obtained by MSC analysis for different alumina powders. .	123

# **Acknowledgments**

I would like to acknowledge how wonderful my girlfriend is. Without her I would be constantly lost in my life.

# **Dedication**

I dedicate this work to William G. and Hannah B. Marker.

# Chapter 1

## Introduction

### 1.1 Motivation

$\text{Al}_2\text{O}_3$  is arguably the most extensively used and researched ceramic material with a total estimated market of 2.8 million tons per year. The applications for  $\text{Al}_2\text{O}_3$  vary drastically such as high temperature refractories, technical ceramics, high voltage insulators, and functional fillers. Bayer feedstocks make a majority of the synthetic and specialty aluminas used in  $\text{Al}_2\text{O}_3$  applications, such as aluminum trihydrate ( $\text{Al}(\text{OH})_3$ ), smelter grade  $\text{Al}_2\text{O}_3$  and others. Bayer process aluminas typically have a purity between 99.0 - 99.9% and contain impurities such as,  $\text{Na}_2\text{O}$ ,  $\text{CaO}$ ,  $\text{Fe}_2\text{O}_3$ , and  $\text{SiO}_2$  that originate from the bauxite ore and/or Bayer process reagents (e.g.,  $\text{NaOH}$ ). However, even with the focus being on purities between 99.0-99.9%, the vast majority of research has focused on ultra-high purity ( $\geq 99.99\%$ ) aluminas derived from specialty feedstocks, such as ammonium alum ( $\text{NH}_4\text{Al}(\text{SO}_4)_2 \cdot 12\text{H}_2\text{O}$ ), boehmite ( $\gamma\text{-AlOOH}$ ) and aluminum chloride ( $\text{AlCl}_3$ ). These high purity powders ( $\geq 99.99\%$  purity) are typically one to two orders of magnitude higher in cost than Bayer process aluminas (99.0 - 99.9% purity). Therefore, an overwhelming majority of the global market share, over 90%, use aluminas derived from the Bayer processes.

Research conducted on ultra-high purity aluminas can provide the best platform for understanding and conducting fundamental research but does not explore the types and amounts of impurities seen in teh typical Bayer aluminas. Different grades of Bayer  $\text{Al}_2\text{O}_3$  powders are made that range in the amount and type of impurities. Additionally,  $\text{MgO}$  is added to commerical alumina powders because it

is known for its beneficial effects during sintering.

The purpose of this thesis is to provide an in-depth investigation of how the chemistry of commercial Bayer alumina powder affects the sintering mechanisms, densification, grain growth, and the nucleation and growth of second phases. Specifically, this dissertation will focus on understanding the effects and cross effects of MgO, Na<sub>2</sub>O and SiO<sub>2</sub> on Bayer process aluminas and how the impurities effect the densification and microstructure evolution as well as, provide insight into the fundamental mechanisms that are responsible for changes in sintering behavior. Furthermore, a model is developed to describe the dynamic development of grain boundaries during densification as a function of powder chemistry. It is crucial to understand the structure and chemistry of grain boundaries during sintering, as grain boundary diffusion is the dominant mechanism for mass transport. The methodology developed to analyze sintering behavior, mechanisms, and grain boundaries during densification will serve as a model for investigating and tailoring the mechanisms of sintering in ceramic powders as a function of powder chemistry. Finally, the Master Sintering Curve approach is evaluated as a tool to evaluate the sinterability of ceramic powders.

## 1.2 The Bayer Process

The Bayer process is a hydrothermal precipitation process. An aqueous solution of caustic soda (NaOH) is used to digest the bauxite mineral ( $\text{AlOOH} \cdot x\text{Fe}_2\text{O}_3 \cdot y\text{SiO}_2$ ) at pressures up to 40 bar and temperatures up to 230°C. Bauxite and NaOH form NaAl(OH)<sub>4</sub>, which dissolves as a complex, while Fe<sub>2</sub>O<sub>3</sub>, SiO<sub>2</sub> and other accessory minerals separate as red mud because they are not soluble under these conditions. The temperature of the sodium aluminate solution is decreased to 50-70°C and Al(OH)<sub>3</sub> seed crystals are added to cause the Al(OH)<sub>3</sub> in the solution to precipitate. The Al(OH)<sub>3</sub> is then heat treated and calcinated at 1100-1200 °C to form  $\alpha$ -Al<sub>2</sub>O<sub>3</sub>.

The main components of bauxite ore are SiO<sub>2</sub> and Fe<sub>2</sub>O<sub>3</sub> and trace amounts are thus present in the final product. SiO<sub>2</sub> is also used in the milling media to grind the calcinate the powder and thus SiO<sub>2</sub> impurities may originate from the milling media [3]. Na<sub>2</sub>O impurities are introduced through the digestion of the bauxite in NaOH and the precipitation of the Al(OH)<sub>3</sub> crystals from the NaAl(OH)<sub>4</sub> solution [3]. The Al(OH)<sub>3</sub> powder surface is washed to remove the NaOH, however,

small amounts of NaOH or rather Na<sub>2</sub>O remain on the powder surface or are entrapped in the alumina grains. Other impurities such as gallium, calcium and magnesium originate from accessory minerals in the bauxite.

## **1.3 Influence of Impurities and Dopants on the Sintering Behavior of Al<sub>2</sub>O<sub>3</sub>**

### **1.3.1 MgO in Al<sub>2</sub>O<sub>3</sub>**

Since the work by Coble, showing that MgO doping produces high-density translucent alumina [4–6], numerous research has been completed to try and understand the underlying mechanisms. Initially the research by Coble concluded, that the abnormal grain growth is prevented by spinel particles that precipitate and pin the grain boundaries. Jorgensen [7, 8] used a solute-drag mechanism to explain the effect MgO had on the sintering of Al<sub>2</sub>O<sub>3</sub>. The solute-drag mechanism was based on the theory for metal systems that was proposed and refined by Lücke and Detert [9] and Cahn [10]. The mechanism suggests that MgO solutes segregate in the grain boundaries and thus controls the grain growth kinetics. When in the initial sintering stage with no grain growth, Jorgensen suggested that MgO decreases the sintering kinetics by lowering the diffusion coefficient and surface energy. Then during the later sintering stages, the segregated MgO increases the sintering kinetics by lowering the mobility of the grain boundaries by decreasing the rate of grain growth and thus leading to enhanced densification. The change in sintering kinetics was proposed by Johnson and Coble [11] to be due to the formation of a solid solution of MgO in Al<sub>2</sub>O<sub>3</sub>, which causes a change in grain growth and pore elimination. More recently, the role of MgO was proposed to be due to a segregation and precipitation mechanism by Zou et al. [12]. When MgO in Al<sub>2</sub>O<sub>3</sub> exceeds the maximum solubility of MgO in the Al<sub>2</sub>O<sub>3</sub> lattice and grain boundaries the excess MgO and Al<sub>2</sub>O<sub>3</sub> forms spinel precipitates on the grain boundaries which reduces the grain boundary mobility and inhibits grain growth. However, Zou et al. [12] continues by proposing, that when MgO in the Al<sub>2</sub>O<sub>3</sub> is below the solubility limit of the crystal and grain boundaries Schottky defects are formed:



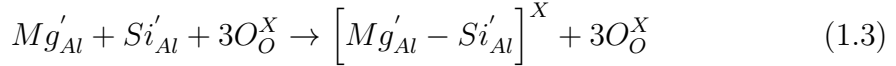
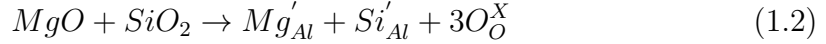
The densification and grain growth are enhanced by the formation of the Schottky defects by the increased concentration of point defects that facilitates diffusion and hence promotes the sintering. They suggest that the required MgO concentration to form spinel decreases with increasing grain size. This is explained by the fact that the total area of the grain-boundary interface decreases with increasing grain size, and hence the maximum concentration of MgO in the Al<sub>2</sub>O<sub>3</sub> grain boundaries changes.

### 1.3.2 Other Impurities in Al<sub>2</sub>O<sub>3</sub>

With Coble's discovery [4–6], there has been a high interest in understanding how small concentrations of other dopants or impurities such as Na<sub>2</sub>O, CaO, Fe<sub>2</sub>O<sub>3</sub>, and SiO<sub>2</sub> affect the sintering kinetics, density and microstructure of alumina. Bae and Baik [2, 13] showed that as long as the impurity content stayed below 10 ppm there was no abnormal grain growth in ultra pure Al<sub>2</sub>O<sub>3</sub>. Previous research has shown a correlation between the presence of a liquid phase and abnormal grain growth suggesting that the impurity content in commercial alumina powders (purity 99.7–99.8%) are high enough to form a liquid phase during sintering, if glass-forming impurities are present [1, 3, 14–17]. Using transmission electron microscopy (TEM) Hansen and Philips [18] studied a 99.8% pure alumina powder, and their TEM images showed the presence of a thin glassy film in grain boundaries of sintered samples. Research has shown that the formation of a liquid phase during sintering can happen even in 99.98% pure alumina and thus cause abnormal grain growth can only be prevented by adding beneficial sintering additives like MgO [19]. Bae and Baik [13] were able to show that a liquid forms during sintering by co-doping Al<sub>2</sub>O<sub>3</sub> with SiO<sub>2</sub> as soon as the solubility of SiO<sub>2</sub> and CaO in Al<sub>2</sub>O<sub>3</sub> is exceeded. They estimated that the solubility of SiO<sub>2</sub> and CaO in Al<sub>2</sub>O<sub>3</sub> is 100 and 20 ppm, and that discontinuous grain growth sets in after a critical thickness of the amorphous grain boundary has formed.

### 1.3.3 Impurities in MgO-doped Al<sub>2</sub>O<sub>3</sub>

As discussed above a very small amounts of impurities are sufficient for the formation of liquid phases during sintering, which exhibit a deleterious effect on the sintering of alumina. Therefore, for a better fundamental understanding of the role of MgO in Al<sub>2</sub>O<sub>3</sub> the presence of other impurities should be considered. MgO is commonly used as an additive for the sintering of commercial aluminas because it prohibits the deleterious effect of the liquid phase forming impurities during sintering and facilitates the formation of a fine and homogeneous microstructure. From the literature, many explanations have been proposed to explain the effect of MgO on the sintering behavior of Al<sub>2</sub>O<sub>3</sub> [3] [20]. The solute-drag mechanism and the pinning-by-particle-precipitation mechanism are commonly accepted interpretations of the role of MgO regardless of the presence of other impurities [21, 22]. However, another possible mechanism is that the liquid film by itself lowers the grain boundary mobility [23]. This is due to the fact that MgO doping provides a uniform wetting of all grain boundaries causing slow isotropic grain growth whereas the undoped cases only basal planes are wetted. It was suggested by Bea and Baik [24] the kinetics of dissolution precipitation mass transport are changed by modifying the viscosity because MgO acts as a glass modifier in intergranular films. Still other interpretations suggest that MgO changes the solubility of other oxides in alumina. Handwerker et al. [15] suggested that the co-dissolving MgO and SiO<sub>2</sub> increases the solubility of SiO<sub>2</sub> because of strain and charge compensation which was further supported by the work of Gavrilov et al. [1]. They used high resolution scanning secondary mass spectrometry (SIMS) to investigate the distribution of impurities in sintered Al<sub>2</sub>O<sub>3</sub> shown in Figure 1.1 and Figure 1.2. The SIMS maps of sintered Al<sub>2</sub>O<sub>3</sub> singly doped with (a) 500 ppm MgO or with (b) 1000 ppm SiO<sub>2</sub> are shown in Figure 1.1, respectively. Areas of high dopant concentrations appear bright, and in both cases it can be seen that the dopants segregate to the grain boundaries. They showed in the SIMS maps in Figure 1.2 that co-doping Al<sub>2</sub>O<sub>3</sub> with 500 ppm MgO and 1000 ppm SiO<sub>2</sub>, leads both dopants to segregate to the grain boundaries, but with a substantially higher MgO and SiO<sub>2</sub> concentration towards the grain center. The authors claim that the solubility of MgO and SiO<sub>2</sub> in Al<sub>2</sub>O<sub>3</sub> is increased by co-doping via the following defect compensation mechanism:



Coble and Roy [25] proposed a similar reaction to explain a higher solubility of  $TiO_2$  in  $Al_2O_3$  when an equimolar amount of  $MgO$  is added. Gavrilov et al. [1] concluded the formation of a liquid phase during sintering is prevented by  $MgO$  increasing the solubility of glass forming impurities in  $Al_2O_3$ . However, they note that other background-impurities might influence the solubility of  $MgO$  in  $Al_2O_3$  as well.

More recently in literature, general explanations for microstructure evolution in ceramics and metals has been explored. The impurities or dopants were proposed to form thermodynamically stable grain boundary phases known as "complexions" and show transitions during sintering [20–22, 25]. They distinguish six complexions which can occur ordered or amorphous and depend on the thickness of the adsorbed layer: clean, monolayer, bilayer, multilayer, nanolayer and wetted. They further state that the type of complexion depends on impurity type, temperature, impurity concentration, and orientation of adjacent crystals and that the mobility of the grain boundaries is determined by the type of complexion. After the impurity solubility is exceeded in the crystal the impurities remain in the grain boundaries. The grain boundaries can then supersaturate during sintering because of the reduction of grain boundary area due to grain growth. The authors argue that there are only 2 ways for the excess impurities to reduce the free energy of the system. The first is by the formation of a new phase and the second is by the transition to another complexion [26]. These two possibilities are competing and which event will occur depends on the activation energy. Different complexions may co-exist in a microstructure since crystal planes of different orientation have different grain boundaries or interface energies and the type and number of complexions coexisting depends mainly on the temperature. Another reason to consider for the formation of different complexions in the same microstructure is due to the inhomogeneous impurity distribution. The authors interpreted the microstructure development of  $Al_2O_3$  with different impurities using this concept.  $SiO_2$  in  $Al_2O_3$  does not have a preferred crystal plane on which it can form precipitations with low interfacial

energy. However, CaO impurities in  $\text{Al}_2\text{O}_3$  can form calcium hexaluminate, which shows epitaxy on the basal planes of  $\alpha\text{-Al}_2\text{O}_3$  and has a low interfacial energy. Therefore also has the activation energy for formation on the basal planes but the activation energy is too high for crystal planes with other orientations. Therefore, the authors' theory proposes that complexion transitions are preferred on the basal planes compared to all other planes which leads to anisotropic and abnormal grain growth. This phenomena is often observed in CaO containing alumina because the activation energy for precipitation is high for all crystal orientations and therefore this system is interpreted to prefer complexion transitions rather than the formation of a new phase. It is stated that the grain growth is enhanced with complexions that have higher grain boundary mobilities formed upon heating. For MgO in  $\text{Al}_2\text{O}_3$ , their theory states that this system behaves isotropic and spinel precipitates are formed which prevents the formation of complexion transitions even though the activation for precipitation is low, or the precipitations occur uniformly throughout the microstructure. However, this model is not applied to densification and only describes the stable microstructure of dense ceramics and metals. Furthermore, the model does not explain how different chemistries and grain boundary structures affect the rate-limiting sintering mechanisms.

Kang et al. [26–29] uses the activation energy and driving force of atoms to cross the grain boundaries to explain the microstructure evolution in metals and ceramics. According to the authors interpretation equiaxed microstructure and normal grain growth happens if the critical driving force for appreciable grain boundary migration is zero and the grains grow "rough". The factors such as temperature, dopant concentration, and oxygen partial pressure, determine the critical driving force for appreciable grain boundary migration. If the critical driving force is zero then the step free energy has to be zero. Meaning the additional surface energy created during nucleation and growth of grains (the ledges of the nucleus) is zero. Thus the grains grow faceted if the critical driving force is not zero and abnormal grain growth occurs when the maximum driving force, i.e. the driving force for the largest grains to grow, is larger than the critical driving force. However, if the maximum driving force is a lot larger than the critical driving force meaning that the driving force of many grains is larger than the critical driving force, than grains start growing fast and abnormally but form a microstructure that looks like a normally grown microstructure, and this is defined as pseudo-normal grain growth.

Grain growth becomes stagnant if the maximum driving force is smaller than the critical driving force and thus the microstructure does not change. Parameters such as partial pressure, temperature, dopants, and impurities for different materials systems were investigated by Kang et al. but they only explained the microstructure evolution qualitatively with a described model, and the majority of observations from experiments were fitted into the model rather than predicted by the model. For example, it is concluded that MgO lowers the step free energy of alumina since the addition of MgO to alumina results in a homogeneous and equiaxed microstructure [26, 29]. However, it is not explained why MgO lowers the step free energy, and why MgO is the only material that lowers the step free energy in that manner. Furthermore the model only takes into account the microstructural evolution in already dense bodies, and does not address densification.

### **1.3.4 Influence of Na<sub>2</sub>O and SiO<sub>2</sub> on the Sintering Behavior of Al<sub>2</sub>O<sub>3</sub>**

Despite the extensive interest in the effects that Na<sub>2</sub>O has on the sintering of alumina only a few studies have been published. The effect of adding 1 wt.% Na<sub>2</sub>O to high purity alumina powder was published by Sumita and Bowen (Sumitomo, AKP-HP) [30]. However, after sintering at 1400°C for 2 h, they determined, using inductively coupled plasma (ICP), that only ~8 ppm Na<sub>2</sub>O was present and did not add any additional details to explain the large discrepancy between the doping concentration and the amount after sintering. The effect of 1 wt.% of different additives on the sintering of 99.3% alumina (Alcoa A-11) was studied by Smothers and Reynolds [31]. They showed that grain growth is inhibited and sintering is retarded by Na<sub>2</sub>CO<sub>3</sub> or NaF. Cahoon and Christensen [32] also reported a deleterious effect of Na<sub>2</sub>O on the sintering of alumina. They added between 300 ppm and 5.9 wt.% Na<sub>2</sub>O to their alumina powder (Alcoa A-14, no purity specifications given) and heated the samples in a 5 days cycle (2 days heating, 3 days cooling) to temperatures between 1600°C and 1835°C for 1 h. They showed an inhibition of abnormal grain growth and a retardation of sintering with increasing Na<sub>2</sub>O as well as cracking of their samples and inferior compressive strengths. Their suggestion was that the formation of  $\beta$ - or  $\zeta$ -Al<sub>2</sub>O<sub>3</sub> caused these effects. They also reported a "moderately deleterious effect" of SiO<sub>2</sub> on the sintering of Al<sub>2</sub>O<sub>3</sub>. They

reported that concentrations of  $\text{SiO}_2$  as low as 0.1 wt.% can inhibit abnormal grain growth and that with increasing  $\text{SiO}_2$  this effect is enhanced. When co-doping  $\text{Al}_2\text{O}_3$  with  $\text{Na}_2\text{O}$  and  $\text{SiO}_2$  they found that the deleterious effects of  $\text{Na}_2\text{O}$  were moderated. The effect of doping  $\text{Al}_2\text{O}_3$  with  $\text{Na}_2\text{O}$  and  $\text{SiO}_2$  on densification and microstructure evolution was studied by Louet et al. [33] for the Bayer process alumina (Rhone-Poulenc, P172SB), containing 550 ppm  $\text{Na}_2\text{O}$ , 770 ppm  $\text{SiO}_2$ , 1010 ppm  $\text{MgO}$ , 600 ppm  $\text{CaO}$  and 115 ppm  $\text{Fe}_2\text{O}_3$ . The levels of  $\text{Na}_2\text{O}$  and  $\text{SiO}_2$  were adjusted by adding  $\text{CH}_3\text{COOH-Na}$  and silica gel. They measured the concentrations of samples after sintering for 2 h at 1540°C while adding  $\text{Na}_2\text{O}$  using ICP and saw they had less than 50 wt.% of their targeted amount. The difference was explained by stating "Na has a very low vaporization temperature (882.9°C) and may easily evaporate from this liquid phase" [33]. Unfortunately, there was no attempt to verify this contention, even though, the effect of  $\text{Na}_2\text{O}$  concentrations as high as 1510 ppm were studied. It was concluded from this work that the doping of  $\text{Na}_2\text{O}$  causes the sintering process to slow and decreases the sintering density from 98 to 97 % when the  $\text{Na}_2\text{O}$  concentration goes from 550 ppm to 1150 ppm. The authors reported a drop in grain size from 4-5  $\mu\text{m}$  to 3  $\mu\text{m}$  when the concentration of  $\text{Na}_2\text{O}$  was greater than 1000 ppm. They then noted that high levels of  $\text{Na}_2\text{O}$  result in a homogenous, fine microstructure. This work also reported that in the presence of  $\text{Na}_2\text{O}$ , increasing  $\text{SiO}_2$  concentration from 770 ppm to as high as 1500 ppm causes anisotropy of the grains but does not affect the final density. The authors' work stated that increasing  $\text{SiO}_2$  concentratnion leads to abnormal grain growht but does not effect the average grain size. However, their presented micrographs show an increase in grain size with increasing  $\text{SiO}_2$  concentration but no abnormal grain growth. The authors' did note that the interperting the results in terms of what is caused by  $\text{Na}_2\text{O}$  or  $\text{SiO}_2$  impurities is difficult because the as-received powder has a large number and high concentrations of several impurities. The effects of different  $\text{SiO}_2$ - and  $\text{Na}_2\text{O}$  concentrations on the sintering behaviour of alumina was also investigated by Compson et al. [3]. They chose four commercial alumina powders that were 99.8 wt.% pure and had similar specific surface areas, particle diameter and particle distributions. The four commercial powders only varied in their impurity concentrations. Specifically, the  $\text{Na}_2\text{O}$  and  $\text{SiO}_2$  concentrations varied from 0.02 to 0.1% and 0.01 to 0.04%, respectively. They showed that the four powders exhibited different shrinkage, sintering and densification behavior in

the temperature range from 1150°C to 1500°C using dilatometry. From their work, they concluded that SiO<sub>2</sub> has a deleterious effect on the sintering of Al<sub>2</sub>O<sub>3</sub>, but they could not detect an influence of Na<sub>2</sub>O.

**This completed thesis consists of the studying the main tasks:**

1. Effects of Na<sub>2</sub>O and SiO<sub>2</sub> on liquid phase sintering of Bayer Al<sub>2</sub>O<sub>3</sub>
2. Powder chemistry effects on the sintering behavior of MgO-doped Bayer Al<sub>2</sub>O<sub>3</sub>
3. Dynamic development of nanometer scale grain boundaries during liquid phase sintering
4. Second phase formation in Bayer Al<sub>2</sub>O<sub>3</sub>
5. A critique of the master sintering curve analysis of sintering processes

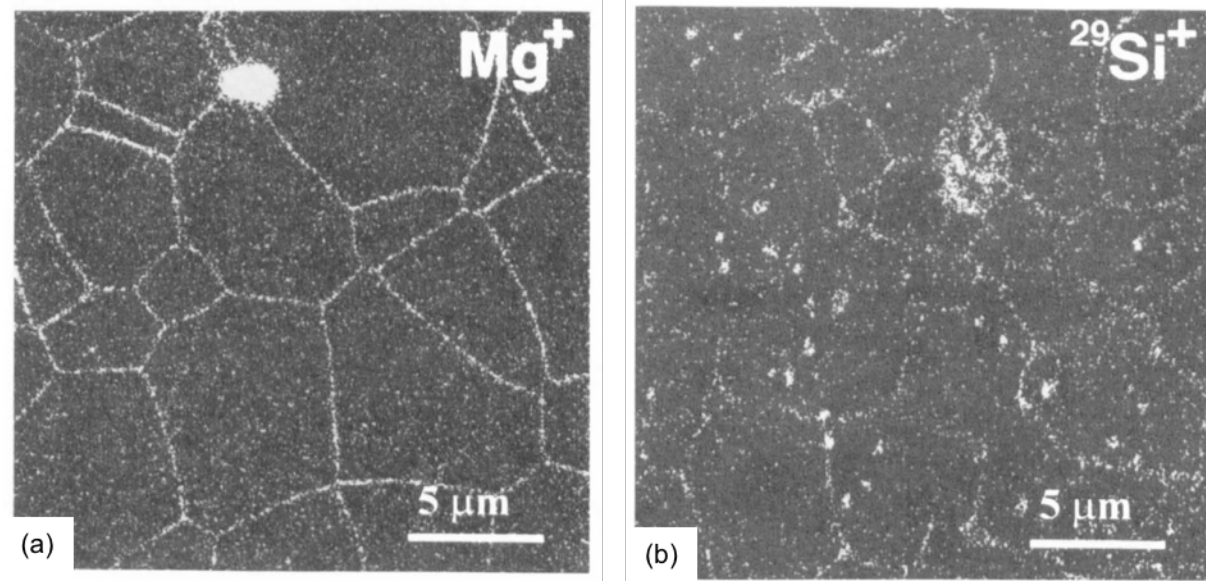


**Figure 1.1.** SIMS maps of  $\text{Al}_2\text{O}_3$  doped with 500 ppm  $\text{MgO}$  (a) and 1000 ppm  $\text{SiO}_2$  (b). Samples were sintered for 8 h at  $1650^\circ\text{C}$  [1].

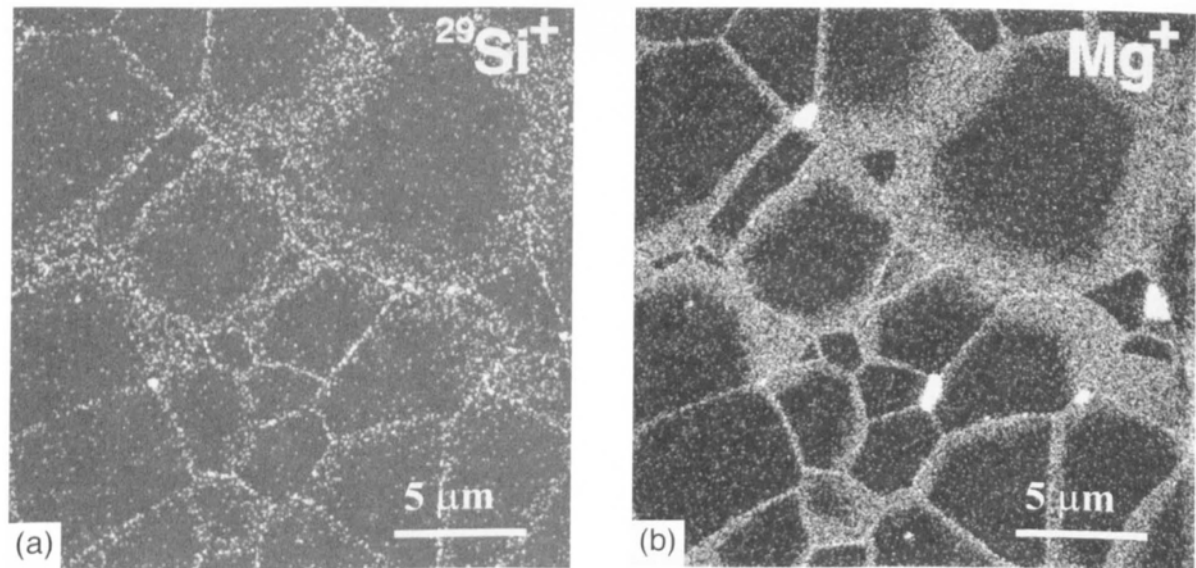


**Figure 1.2.** SIMS maps of  $\text{Al}_2\text{O}_3$  co-doped with 500 ppm  $\text{MgO}$  and 1000 ppm  $\text{SiO}_2$  and sintered at 1650°C for 8h. (a) shows the distribution of  $\text{SiO}_2$ , (b) the distribution of  $\text{MgO}$  in the same samples [1].

# **Chapter 2 |**

# **The Effects of Na<sub>2</sub>O and SiO<sub>2</sub>**

# **on Liquid Phase Sintering of Bayer**

# **Al<sub>2</sub>O<sub>3</sub>**

## **2.1 Introduction**

Al<sub>2</sub>O<sub>3</sub> is arguably the most extensively used and researched ceramic material because it is used in many large volume applications such as high temperature refractories, technical ceramics, high voltage insulators, and functional fillers. The majority of Al<sub>2</sub>O<sub>3</sub> applications use synthetic or specialty aluminas derived from Bayer feedstocks, such as aluminum trihydrate (Al(OH)<sub>3</sub>), smelter grade Al<sub>2</sub>O<sub>3</sub> and others. Bayer process aluminas are typically 99.0 - 99.9% pure and contain Na<sub>2</sub>O, CaO, Fe<sub>2</sub>O<sub>3</sub>, and SiO<sub>2</sub> impurities that originate from the bauxite ore and/or Bayer process reagents (e.g., NaOH). The vast majority of research on the sintering of Al<sub>2</sub>O<sub>3</sub>, however, focuses on ultra-high purity ( $\geq 99.99\%$ ) aluminas derived from specialty feedstocks, such as ammonium alum (NH<sub>4</sub>Al(SO<sub>4</sub>)<sub>2</sub>·12H<sub>2</sub>O), boehmite ( $\gamma$ -AlOOH) and aluminum chloride (AlCl<sub>3</sub>). While ultra-high purity aluminas provide the purest platform from which to conduct fundamental sintering research, that research does not usually explore the types and amounts of impurities typical of Bayer aluminas. Commercial Bayer Al<sub>2</sub>O<sub>3</sub> powders exist in a range of reactive grades that differ in the amount and types of these impurities. Therefore, the evaluation of specialty reactive aluminas, within the context of previous work on ultra-high purity aluminas, is a valuable contribution to industrial users and bridges

fundamental sintering research with ultra-high purity aluminas.

## 2.2 Experimental

A chemically purified 0.4  $\mu\text{m}$  median particle size Bayer process  $\text{Al}_2\text{O}_3$  powder (Almatis, Inc., Leetsdale, PA, USA) with only 2 ppm  $\text{MgO}$  was used to study the sintering of near  $\text{MgO}$ -free Bayer  $\text{Al}_2\text{O}_3$  (Figure 2.1). The powder was chemically purified by the manufacturer so that impurity levels similar to commercial high purity Bayer process aluminas were obtained after doping with  $\text{Na}_2\text{O}$  and/or  $\text{SiO}_2$ . The physical and chemical characteristics of the as-received powder are shown in Table 2.1. Chemical analysis of the as-received  $\text{Al}_2\text{O}_3$  was performed by inductively coupled plasma (ICP) emission spectroscopy (iCap 6000, Thermo Fischer Scientific, Inc., Waltham, MA, USA) after  $\text{Al}_2\text{O}_3$  samples were acid digested in a microwave digestion unit in a Teflon<sup>TM</sup> sample holder. It should be noted that the as-received Bayer  $\text{Al}_2\text{O}_3$  contained impurity levels of 90 ppm  $\text{Fe}_2\text{O}_3$ , 62  $\text{CaO}$ , and 22 ppm  $\text{TiO}_2$ . The  $\text{Na}_2\text{O}$  and  $\text{SiO}_2$  reported after doping include the impurity concentrations in the as-received powder (29 ppm  $\text{Na}_2\text{O}$  and 103 ppm  $\text{SiO}_2$ ).

The  $\text{Al}_2\text{O}_3$  powders were doped with up to 1000 ppm  $\text{Na}_2\text{O}$  using sodium acetate ( $\text{NaC}_2\text{H}_3\text{O}_2 \cdot 3\text{H}_2\text{O}$ , ACS grade, BDH, West Chester, PA, USA), based on the procedure reported by Louet et al. [33]. The  $\text{Al}_2\text{O}_3$  powders were dispersed in a solution of sodium acetate dissolved in de-ionized water. The suspension was stirred on a magnetic stir plate for 5 h at room temperature, and held at 80°C for 24 h while stirring until the mixture was too viscous to stir, and then dried at 100°C for 24 h.

Samples were doped with up to 500 ppm  $\text{SiO}_2$  by first dissolving tetraethyl orthosilicate (TEOS,  $\text{Si}(\text{OC}_2\text{H}_5)_4$ , 98%, Aldrich Chemical Company, Inc., Milwaukee, WI, USA) in 200 proof ethanol with a few drops of de-ionized water to hydrolyze the TEOS and immediately mixed at room temperature for 5 h with either the as-received or  $\text{Na}_2\text{O}$ -doped  $\text{Al}_2\text{O}_3$  powder. The mixture was subsequently stirred at 70°C for an additional 12 h. The powder was then dried at 100°C for 2 h, followed by crushing in a mortar and pestle, and sieving to -106  $\mu\text{m}$  (US Standard 140 mesh).

Samples were prepared for sintering studies by uniaxially dry pressing the powders at 170 MPa and then cold isostatic pressing at 200 MPa (CIP, Autoclave

Engineers, Erie, PA, USA) to obtain cylindrical samples (3.0-3.5 mm long by 12.7 mm diameter or 8.5-10 mm long by 6 mm diameter) with green densities of 59.0%  $\pm$  0.5% of theoretical density. To investigate the sintering process, dry pressed 8.5-10 mm long by 6 mm diameter cylinders were heated at 10°C/min to 1525°C in a thermomechanical analyzer (TMA, Linseis PT1600, Robbinsville, NJ, USA). The kinetics of sintering and grain growth were evaluated on 3.0-3.5 mm long by 12.7 mm diameter samples heated at 10°C/min to 1200 °C then 5°C/min to 1525°C followed by sintering at 1525°C for up to 8 h. The density of three samples of each condition was measured by the Archimedes method according to ASTM standard B962-15 [?] and the average density reported for each sintering time and temperature. For microstructure analysis, samples were first polished to a surface finish of 1  $\mu$ m and then thermally etched in air at 1425°C for 40 min. Average grain sizes were measured on SEM (ESEM, Quanta 200, FEI Company, Hillsboro, OR, USA) micrographs using a linear intercept method (ASTM Standard E112-96) [?].

## 2.3 Results

### 2.3.1 Effects of Na<sub>2</sub>O-doping

The doping experiments were designed to uniformly distribute Na<sub>2</sub>O and SiO<sub>2</sub> on the surfaces of the Al<sub>2</sub>O<sub>3</sub> particles. Upon heating the dopant NaC<sub>2</sub>H<sub>3</sub>O<sub>2</sub>·3H<sub>2</sub>O first dehydrates and then decomposes to form Na<sub>2</sub>CO<sub>3</sub> above 385°C [34]. Using a video recorder, we observed that anhydrous sodium acetate melts and rapidly spreads on the surface of an Al<sub>2</sub>O<sub>3</sub> substrate at  $\sim$ 420°C. Na<sub>2</sub>CO<sub>3</sub> melts at 851°C and subsequently decomposes to Na<sub>2</sub>O [34]. As a result of the rapid wetting of the Na<sub>2</sub>O precursor on the Al<sub>2</sub>O<sub>3</sub> substrate we conclude that Na<sub>2</sub>O is uniformly distributed on the powder surface by the acetate doping process.

Figure 2.2 shows the shrinkage behavior of Bayer Al<sub>2</sub>O<sub>3</sub> doped with different Na<sub>2</sub>O concentrations during heating to 1525°C at 10°C/min. The as-received Al<sub>2</sub>O<sub>3</sub> (intrinsic impurities: 29 ppm Na<sub>2</sub>O, 103 ppm SiO<sub>2</sub>) begins to shrink at  $\sim$ 1050 °C, whereas shrinkage begins at 1100°C for samples doped with 1029 ppm Na<sub>2</sub>O. The difference in density at the beginning of densification continues throughout the heating cycle. However, above  $\sim$ 1350°C the densification rate of the Na<sub>2</sub>O doped samples surpasses that of the as-received sample. Overall, the Na<sub>2</sub>O-doped samples

are 2.5% less dense than the as-received  $\text{Al}_2\text{O}_3$  after heating to 1525°C.

Figure 2.3 shows the influence of  $\text{Na}_2\text{O}$  concentration on the densification kinetics at 1525°C. Clearly, the degree of densification decreases with increasing  $\text{Na}_2\text{O}$  concentration for up to 30 min with the  $\text{Na}_2\text{O}$ -doped samples being as much as 2% less dense than the as-received  $\text{Al}_2\text{O}_3$ . However, after  $\geq 30$  min at 1525°C densification is independent of  $\text{Na}_2\text{O}$  content and all samples are 97.5-98.0% dense after  $\geq 3$  h.

The microstructures of as-received samples (29 ppm  $\text{Na}_2\text{O}$ ) and samples doped with 529 ppm  $\text{Na}_2\text{O}$  sintered for 30 min, 3 h and 8 h at 1525°C are compared in Figure 2.4. It is seen that higher  $\text{Na}_2\text{O}$  concentration does not affect the average grain size for all hold times. Microstructures of as-received samples are predominantly equiaxed with a small number of faceted grains, whereas samples doped with  $\text{Na}_2\text{O}$  appear to have an increasing number of faceted grain boundaries with increasing  $\text{Na}_2\text{O}$  concentration. A few tabular grains of up to  $60 \mu\text{m}$  were seen in both as-received and  $\text{Na}_2\text{O}$ -doped samples after 8 h at 1525°C (see Figure 2.4c and 2.4f). Those faceted grains are larger in the as-received powder samples compared to  $\text{Na}_2\text{O}$ -doped samples, whereas the  $\text{Na}_2\text{O}$ -doped samples show more large tabular grains than samples from the as-received powder.

### 2.3.2 Effects of $\text{Na}_2\text{O}/\text{SiO}_2$ co-doping

As seen in Figure 2.5, the presence of 603 ppm  $\text{SiO}_2$  significantly retards densification of as-received alumina. Starting at  $\sim 1250^\circ\text{C}$ , all of the  $\text{SiO}_2$ -doped samples densify less than as-received and singly  $\text{Na}_2\text{O}$ -doped samples. The densification rate of the  $\text{SiO}_2$ -doped samples from 1250 to 1525°C is slower than the as-received alumina.  $\text{SiO}_2$  reduces the linear shrinkage by  $\sim 3.0\%$  and thus the samples are 8.7% less dense than the as-received  $\text{Al}_2\text{O}_3$  after 8 h at 1525°C.

The densification kinetics of the  $\text{Al}_2\text{O}_3$  powders doped with different amounts of  $\text{Na}_2\text{O}$  (154 and 529 ppm) and  $\text{SiO}_2$  (203 and 603 ppm) are compared in Figure 2.6. It is seen that the addition of  $\text{SiO}_2$  significantly reduces sintered density for all hold times. For example, samples containing as much as 603 ppm  $\text{SiO}_2$  have densities of 81.5% after 0 h and 93.8% after 8 h at 1525°C, whereas the as-received and singly  $\text{Na}_2\text{O}$ -doped  $\text{Al}_2\text{O}_3$  samples are 98% dense after 3 h at 1525°C.

Figure 2.6 shows the effect of  $\text{Na}_2\text{O}$  on the densification of  $\text{SiO}_2$ -doped samples.

For hold times < 1 h, samples doped with 529 ppm Na<sub>2</sub>O and 203 ppm SiO<sub>2</sub> are ~ 1.5% denser than samples doped with 154 ppm Na<sub>2</sub>O and 203 ppm SiO<sub>2</sub>. A difference in Na<sub>2</sub>O concentration does not affect the final density of samples containing 203 ppm SiO<sub>2</sub> (96.5 - 97.0%) after 3 h at 1525°C. For higher SiO<sub>2</sub> concentrations (603 ppm), singly SiO<sub>2</sub> doped samples are 1 - 2.5% less dense than samples co-doped with 529 ppm Na<sub>2</sub>O and 603 ppm SiO<sub>2</sub> for all hold times at 1525°C.

The average grain sizes of the as-received and Na<sub>2</sub>O-doped samples are nominally the same and increase from 1.6  $\mu\text{m}$  to 2.5  $\mu\text{m}$  after 30 min and 8 h at 1525°C, respectively. There was little grain growth (1.4  $\mu\text{m}$  to 2.1  $\mu\text{m}$ ) in singly SiO<sub>2</sub>-doped samples (603 ppm) after 30 min and 8 h at 1525°C, respectively. In samples co-doped with 529 ppm Na<sub>2</sub>O and 603 ppm SiO<sub>2</sub> the average grain size is 1.6  $\mu\text{m}$  for hold times between 30 min and 8 h at 1525°C. The limited grain growth is attributed primarily to the large fraction of porosity. Micrographs of 603 ppm SiO<sub>2</sub> singly doped and 529 ppm Na<sub>2</sub>O and 603 ppm SiO<sub>2</sub> co-doped samples heated for 8 h after heating for 8 h at 1525°C are compared in Figure 2.7. Both samples are only 92-94% dense and thus it was difficult to prepare polished micrographs without some grain pull-out.

## 2.4 Discussion

To understand the above effects, we first note from the Al<sub>2</sub>O<sub>3</sub>-Na<sub>2</sub>O phase diagram [35] that Na<sub>2</sub>O is insoluble in  $\alpha$ -Al<sub>2</sub>O<sub>3</sub>. A few platelet shaped grains with high aspect ratios were observed in the microstructures of sintered Na<sub>2</sub>O-doped samples (Figure 2.8). Due to their morphology and literature reports, [36–40] it is assumed that these grains are a type of  $\beta$ -Al<sub>2</sub>O<sub>3</sub>. Four types of  $\beta$ -Al<sub>2</sub>O<sub>3</sub> exist; two of them,  $\beta$ -Al<sub>2</sub>O<sub>3</sub> (Na<sub>2</sub>O·11Al<sub>2</sub>O<sub>3</sub>) and  $\beta''$ -Al<sub>2</sub>O<sub>3</sub> (Na<sub>2</sub>O·5Al<sub>2</sub>O<sub>3</sub>), form in the binary system Na<sub>2</sub>O-Al<sub>2</sub>O<sub>3</sub> [41, 42]. The determination of which type of  $\beta$ -Al<sub>2</sub>O<sub>3</sub> forms and the conditions of formation were not the subject of this work, so these analyses were not performed.

Sodium aluminate (NaAlO<sub>2</sub>) is reported to form at temperatures as low as 900°C, [43] and  $\beta''$ -Al<sub>2</sub>O<sub>3</sub> (Na<sub>2</sub>O·5Al<sub>2</sub>O<sub>3</sub>) can be synthesized at temperatures as low as 1100 °C [?, ?, 44]. Therefore, we hypothesize that either sodium aluminate or  $\beta''$ -Al<sub>2</sub>O<sub>3</sub> forms before the onset of densification and that the presence of the

second phases on the surface of the Al<sub>2</sub>O<sub>3</sub> particles retards the initial shrinkage of Na<sub>2</sub>O-doped samples at  $\sim$ 1050°C. However, we did not observe any  $\beta$ -Al<sub>2</sub>O<sub>3</sub> type grains in the samples at this temperature. Alternatively, as discussed below, Na<sub>2</sub>O may interact with the 103 ppm of intrinsic SiO<sub>2</sub> in the sample.

We hypothesize that the initial grain boundaries in the as-received Al<sub>2</sub>O<sub>3</sub> are wetted with the intrinsic impurities such as Na<sub>2</sub>O, CaO, TiO<sub>2</sub> and SiO<sub>2</sub>. Doping with Na<sub>2</sub>O and SiO<sub>2</sub> changes the relative grain boundary chemistries and the properties of the respective grain boundary liquids. In the presence of a grain boundary liquid, densification occurs by a solution-precipitation sintering process, and thus, the rate of densification is controlled by either interface reaction between the grain boundary liquid and Al<sub>2</sub>O<sub>3</sub> grains, or by the diffusion of Al<sup>3+</sup> through the liquid grain boundary film. Al<sup>3+</sup> diffusion is rate-limiting at 1525°C since it has been shown for molten glass systems that Al<sup>3+</sup> has lower ionic diffusion rates than O<sup>2-</sup> [45]. For diffusion-controlled densification, the densification rate is given by [46, 47]

$$\frac{d\left(\frac{\Delta\rho}{\rho}\right)}{dt} = \frac{A\delta D_l C_0 \gamma_{l\nu} \Omega}{kT} r_s^{-4} \quad (2.1)$$

and for interface reaction-controlled densification, the densification rate is given by

$$\frac{d\left(\frac{\Delta\rho}{\rho}\right)}{dt} = \frac{B K C_0 \gamma_{l\nu} \Omega}{kT} r_s^{-2} \quad (2.2)$$

where  $A$  and  $B$  are geometric factors,  $\delta$  is the thickness of the liquid film,  $D_l$  is the diffusion coefficient of Al<sup>3+</sup> in the liquid,  $C_o$  is the equilibrium solute concentration,  $K$  the interface reaction constant,  $\gamma_{l\nu}$  is the liquid surface tension,  $\Omega$  is the molecular volume of the solid,  $r_s$  is the particle radius,  $k$  is the Boltzmann constant and  $T$  is absolute temperature.

Equations 2.1 and 2.2 can be used to gain insights into the rate-limiting densification mechanisms during liquid phase sintering by evaluating their ratio [46, 47]

$$\alpha = \frac{A\delta D_l}{B K} r_s^{-2} \quad (2.3)$$

In general, for  $\alpha > 1$ , densification is controlled by the interface reaction, since  $D_l$  is relatively high. For  $\alpha < 1$ , densification is controlled by diffusion, and for  $\alpha = 1$  both mechanisms contribute equally to densification [47]. Since the product

of the grain boundary thickness and the diffusion coefficient greatly influences the rate-determining mechanism,  $\delta D_l$  and the interface reaction constant  $K$  were examined in more detail.

Because the main impurities in Bayer aluminas are  $\text{SiO}_2$  and  $\text{Na}_2\text{O}$ , the  $\text{Al}_2\text{O}_3$ - $\text{SiO}_2$ - $\text{Na}_2\text{O}$  ternary phase diagram [35] was utilized to evaluate the effects of dopant type and concentration on solubility of  $\text{Al}_2\text{O}_3$  in the grain boundary liquid. It is assumed that the system approaches thermodynamic equilibrium upon holding at 1525°C, and thus the equilibrium composition of the liquid at 1525°C can be calculated from the ternary phase diagram (Figure 2.9). For simplification, we considered only  $\text{Al}_2\text{O}_3$ ,  $\text{SiO}_2$  and  $\text{Na}_2\text{O}$  for the analysis, and assumed that all impurities/dopants are located in the grain boundaries. It was stated earlier that  $\text{Na}_2\text{O}$  is not soluble in  $\text{Al}_2\text{O}_3$ , and it has been reported in the literature that  $\text{SiO}_2$  segregates at the grain boundaries in  $\text{Al}_2\text{O}_3$  [48]. Figure 2.9 shows the liquidus projection of the  $\text{Al}_2\text{O}_3$ - $\text{SiO}_2$ - $\text{Na}_2\text{O}$  ternary phase diagram. The red solid lines connecting the  $\text{Al}_2\text{O}_3$  end member to the  $\text{Na}_2\text{O}$ - $\text{SiO}_2$  side are binary cuts through the ternary (isoplethal sections) and correspond to some of the  $\text{Na}_2\text{O}/\text{SiO}_2$  ratios investigated in this study. The red dashed line is the isotherm at 1525°C for the part of the phase diagram where  $\alpha$ - $\text{Al}_2\text{O}_3$  and liquid are in equilibrium. The blue dash-dot line and the green dotted line are eutectic lines along which  $\beta$ - $\text{Al}_2\text{O}_3$  or mullite is stable with  $\alpha$ - $\text{Al}_2\text{O}_3$  and a liquid. The isotherm and the eutectic lines are important for determining the stable phases and the composition of the liquid in the samples. If a binary cut intersects the isotherm (red dashed line) only  $\alpha$ - $\text{Al}_2\text{O}_3$  and liquid are stable phases at 1525°C and the intersection point determines the composition of the liquid. If a binary cut intersects one of the two marked eutectic lines (blue dash-dot or green dotted) a third phase ( $\beta$ - $\text{Al}_2\text{O}_3$  or mullite) is stable in those samples, and the composition of the liquid at 1525°C is determined by the intersection point of the respective intersected eutectic line with the isotherm at 1525°C.

The  $\text{Al}_2\text{O}_3$ - $\text{SiO}_2$ - $\text{Na}_2\text{O}$  phase diagram demonstrates that a small amount of liquid is stable at 1525°C for all compositions investigated. Note that these overall compositions are all very close to the  $\text{Al}_2\text{O}_3$  end member ( $\sim 99.8\%$   $\text{Al}_2\text{O}_3$ ) and  $\text{Na}_2\text{O}$  and  $\text{SiO}_2$  are insoluble in  $\text{Al}_2\text{O}_3$ . Isoplethal sections (red solid lines in Figure 2.9) can be used to determine the stability and equilibrium composition of a liquid since the volume fractions of  $\text{Na}_2\text{O}$  and  $\text{SiO}_2$  are known. Lambotte

and Chartrand [35] calculated isoplethal sections of the ternary phase diagram, and based on their calculations, the solubility of  $\text{Al}_2\text{O}_3$  in the liquid at 1525°C in the samples was estimated based on the respective  $\text{Na}_2\text{O}:\text{SiO}_2$  ratios (assuming a constant liquid density of 2.45 g/cm [?, 49]). Likewise, the volume fractions of liquid and solid phases can be estimated since the doping and impurity concentrations of  $\text{SiO}_2$  and  $\text{Na}_2\text{O}$  are known. Table 2.2 summarizes the stable phases, the liquid compositions, and the total amount of liquid in the as-received and doped samples. Stable liquids at 1525°C are predicted for liquid compositions with  $\text{Na}_2\text{O}:\text{SiO}_2$  ratios between 0.25 and 0.5. As described above, for higher  $\text{Na}_2\text{O}$  concentrations in the samples (global  $\text{Na}_2\text{O}:\text{SiO}_2$  ratio > 0.5),  $\alpha$ - $\text{Al}_2\text{O}_3$ ,  $\beta$ - $\text{Al}_2\text{O}_3$  and a liquid with a  $\text{Na}_2\text{O}:\text{SiO}_2$  ratio of 0.5 are stable. For sample compositions with higher  $\text{SiO}_2$  concentrations (global  $\text{Na}_2\text{O}:\text{SiO}_2$  ratio < 0.25)  $\alpha$ - $\text{Al}_2\text{O}_3$ , mullite and a liquid with a  $\text{Na}_2\text{O}:\text{SiO}_2$  ratio of 0.25 are stable. Since the global  $\text{Na}_2\text{O}:\text{SiO}_2$  ratio in most of the samples investigated in this work is either > 0.5 or < 0.25, the liquid in those samples had compositions of 0.5 or 0.25, respectively. As the  $\text{Na}_2\text{O}:\text{SiO}_2$  ratio in the liquid increases from 0.25 to 0.5 the solubility of  $\text{Al}_2\text{O}_3$  in the liquid increases from 18.4 vol.% to 21.6 vol.% [35]. The increased  $\text{Al}_2\text{O}_3$  solubility leads to higher densification rates and higher densities in  $\text{Na}_2\text{O}/\text{SiO}_2$  co-doped samples compared to singly  $\text{SiO}_2$ -doped samples, regardless of the rate-limiting process.

Assuming fully dense samples and the liquid volume fractions reported in Table 2.2, we calculated the grain boundary thickness  $\delta$  using:

$$\delta = 2 \frac{V_g \phi}{S_g (1 - \phi)} \quad (2.4)$$

where  $\phi$  is the liquid volume fraction and  $V_g$  and  $S_g$  are the volume and the surface area based on the average grain size, respectively. For as-received and singly  $\text{Na}_2\text{O}$ -doped samples the grain boundary thickness is < 0.3 nm for all observed grain sizes. For  $\text{Na}_2\text{O}/\text{SiO}_2$ -co-doped samples (603 ppm  $\text{SiO}_2$ ) the grain boundary thickness is between 0.8 and 1.8 nm for grain sizes of 1  $\mu\text{m}$  and 2.5  $\mu\text{m}$ , respectively. The calculated grain boundary thickness of singly  $\text{SiO}_2$ -doped samples is similar to that of as-received samples, since mullite is predicted to form in the  $\text{Al}_2\text{O}_3\text{-SiO}_2\text{-Na}_2\text{O}$  system for low  $\text{Na}_2\text{O}$  concentrations at 1525°C. However, mullite may not form in Bayer process  $\text{Al}_2\text{O}_3$  due to the presence of other impurities, such as  $\text{CaO}$ , which, similar to  $\text{Na}_2\text{O}$ , lowers the eutectic temperature and acts as a network modifier

in the glass. Therefore, the grain boundary thicknesses of singly  $\text{SiO}_2$ -doped and  $\text{Na}_2\text{O}/\text{SiO}_2$  co-doped samples are expected to be similar at  $\sim 1.8$  nm. The amount of liquid in the samples and, therefore, the grain boundary thickness, is governed mainly by the amount of glass forming species in the samples, i.e.  $\text{SiO}_2$ .

The diffusion coefficient of  $\text{Al}^{3+}$  through the liquid grain boundary phase can be calculated with the Eyring relation

$$D_l = \frac{kT}{\eta\lambda} \quad (2.5)$$

where  $\eta$  is the viscosity of the grain boundary liquid and  $\lambda$  is the jump distance of the diffusion species, taken as the ionic diameter of an  $\text{Al}^{3+}$  ( $1.07$  Å). Using viscosity data (range of  $20$  -  $400$  Pa\*s) from the literature [50], we estimated the diffusion coefficients to be  $\sim 1 \times 10^{-7}$  and  $\sim 5 \times 10^{-9}$  cm $^2$ /s for  $\text{Na}_2\text{O}/\text{SiO}_2$  co-doped and singly  $\text{SiO}_2$ -doped samples, respectively.

Although we can calculate values for grain boundary thickness ( $\delta$ ) and viscosity ( $\eta$ ), an exact  $\alpha$ -ratio cannot be determined using Equation 2.3 because we do not know the interface reaction constant ( $K$ ). Nevertheless, assuming a reasonable  $K$  value from the literature ( $K = 5 \times 10^{-8}$  m/s) [47] and assuming that the A/B ratio (A and B being geometrical factors) is on the order of 1, we estimated  $\alpha$  to be  $\sim 10^{-2}$  and  $\sim 1$  for singly  $\text{SiO}_2$ -doped samples (603 ppm  $\text{SiO}_2$ ) and  $\text{Na}_2\text{O}/\text{SiO}_2$  co-doped samples (529/603 ppm), respectively. Thus, we conclude that at  $1525^\circ\text{C}$  densification of Bayer aluminas with low  $\text{Na}_2\text{O}/\text{SiO}_2$  concentration ratios is governed by diffusion, whereas densification of Bayer aluminas with high  $\text{Na}_2\text{O}/\text{SiO}_2$  concentration ratios can be governed by either diffusion or interface reaction.

The enhanced densification of  $\text{Na}_2\text{O}/\text{SiO}_2$  co-doped samples compared to singly  $\text{SiO}_2$ -doped is attributed to two factors; the increased solubility of  $\text{Al}_2\text{O}_3$  in the liquid grain boundary phase, and the enhanced diffusion of  $\text{Al}^{3+}$  ( $\sim 5 \times 10^{-9}$  to  $\sim 1 \times 10^{-7}$  cm $^2$ /s) through the liquid grain boundary. This effect of enhanced densification of  $\text{Na}_2\text{O}/\text{SiO}_2$  co-doped samples compared to singly  $\text{SiO}_2$ -doped samples is observed in both the dilatometry curves and the densification kinetics data shown in Figure 2.2 and Figure 2.6, respectively.

It should be noted that a particular challenge for thermal processing studies with soda-based ceramics is  $\text{Na}_2\text{O}$  volatilization at relatively lower temperature than the sintering temperature. Soda by itself is highly volatile at temperatures

< 1000°C and the evaporation of soda from Na<sub>2</sub>O containing technical ceramics such as sodium niobates [51] and  $\beta$ -Al<sub>2</sub>O<sub>3</sub> during sintering is often reported. For example,  $\beta$ -Al<sub>2</sub>O<sub>3</sub> (Na<sub>2</sub>O·11Al<sub>2</sub>O<sub>3</sub>) has an appreciable Na<sub>2</sub>O vapor pressure at temperatures > 1400°C [?], and when heated in air to > 1500°C,  $\beta$ -Al<sub>2</sub>O<sub>3</sub> converts to  $\alpha$ -Al<sub>2</sub>O<sub>3</sub> by volatilization of Na<sub>2</sub>O [?, 52]. Therefore, Na<sub>2</sub>O evaporation from the samples during heating should be considered as samples might have somewhat lower Na<sub>2</sub>O concentrations than assumed for the above calculations. Thus, for samples with low Na<sub>2</sub>O:SiO<sub>2</sub> ratios, the liquid grain boundary phase may contain somewhat less Na<sub>2</sub>O and the grain boundary thickness may be somewhat less than calculated. However, for singly Na<sub>2</sub>O-doped samples and for co-doped samples with high Na<sub>2</sub>O:SiO<sub>2</sub> ratios (e.g. Na<sub>2</sub>O  $\geq$  529 ppm for samples with 603 ppm SiO<sub>2</sub>) the composition of the grain boundary liquid and the grain boundary thickness is not expected to change very much if Na<sub>2</sub>O volatilizes. Consequently, even with Na<sub>2</sub>O volatilization, the proposed sintering mechanisms do not change. The evaporation of Na<sub>2</sub>O from Bayer Al<sub>2</sub>O<sub>3</sub> samples will be further discussed in future work.

## 2.5 Summary

High concentrations of Na<sub>2</sub>O in Bayer process Al<sub>2</sub>O<sub>3</sub> powders inhibit densification in the initial sintering stage and retard densification up to the final sintering stage compared to powders with low Na<sub>2</sub>O concentrations. However, Na<sub>2</sub>O shows no adverse effect on the final density after longer hold times ( $\geq$  3 h at 1525°C). The addition of SiO<sub>2</sub> to Bayer process Al<sub>2</sub>O<sub>3</sub> powders substantially retards densification, starting at  $\sim$ 1250°C, and samples containing as much as 603 ppm SiO<sub>2</sub> are 4% less dense than samples containing 103 ppm SiO<sub>2</sub>, even after hold times as long as 8 h at 1525°C. Co-doping with Na<sub>2</sub>O and SiO<sub>2</sub> increases densification by 1 - 2.5% relative density relative to singly SiO<sub>2</sub>-doped samples. The observed differences in sintering behavior can be explained by a liquid phase sintering model. Diffusion and solubility of Al<sub>2</sub>O<sub>3</sub> in the SiO<sub>2</sub>-based liquid in the grain boundaries is low at the temperatures used in this study, which explains the substantial retardation of densification by SiO<sub>2</sub>. As predicted from the phase diagram Na<sub>2</sub>O increases the solubility of Al<sub>2</sub>O<sub>3</sub> in the siliceous grain boundary phase. As predicted from viscosity data Na<sub>2</sub>O enhances diffusion of Al<sup>3+</sup> through the liquid grain boundary phase. Both factors contribute to the enhanced densification rates of samples with

high  $\text{Na}_2\text{O}/\text{SiO}_2$  ratios compared to samples with low  $\text{Na}_2\text{O}/\text{SiO}_2$  ratios.

**Table 2.1.** Physical and chemical characteristics of the as-received Bayer Al<sub>2</sub>O<sub>3</sub> powder used in this study.

BET (m <sup>2</sup> /g)	7.4
D <sub>50</sub> (μm)	0.4
D <sub>90</sub> (μm)	1.5
	ICP (ppm)
Al <sub>2</sub> O <sub>3</sub>	99.96 %
SiO <sub>2</sub>	103
Na <sub>2</sub> O (total)	29
Fe <sub>2</sub> O <sub>3</sub>	90
CaO	62
TiO <sub>2</sub>	22
MgO	2

**Table 2.2.** Calculated compositions and amounts of liquid in as-received, singly doped and co-doped samples at 1525°C ( $\alpha = \alpha\text{-Al}_2\text{O}_3$ ,  $\beta = \beta\text{-Al}_2\text{O}_3$ , L = liquid, M = mullite).

Global dopant concentration		Global Na <sub>2</sub> O:SiO <sub>2</sub> ratio	Na <sub>2</sub> O:SiO <sub>2</sub> ratio in Liquid	Composition of liquid (mol %)			Amount of liquid (vol. %)	Stable phases
ppm (wt.)	ppm (mol)			Na <sub>2</sub> O	SiO <sub>2</sub>	Al <sub>2</sub> O <sub>3</sub>		
Na <sub>2</sub> O/SiO <sub>2</sub>	Na <sub>2</sub> O/SiO <sub>2</sub>							
As-received								
29/103	48/175	0.27	0.25	17.9	63.4	19.7	0.03%	$\alpha + L$
154/103-	253/175-							
1029/103	1693/175	1.45-9.67	0.5	26.1	52.3	21.6	0.03%	$\alpha + L + \beta$
29/603	48/1023	0.05	0.25	16.3	65.3	18.4	0.03%	$\alpha + L + M$
154/603	253/1023	0.25	0.25	16.3	65.3	18.4	0.16%	$\alpha + L$
279/603	459/1023	0.45	0.45	24.5	54.6	20.8	0.19%	$\alpha + L$
529/603	870/1023	0.85	0.5	26.1	52.3	21.6	0.22%	$\alpha + L + \beta$
1029/603	1693/1023	1.65	0.5	26.1	52.3	21.6	0.22%	$\alpha + L + \beta$

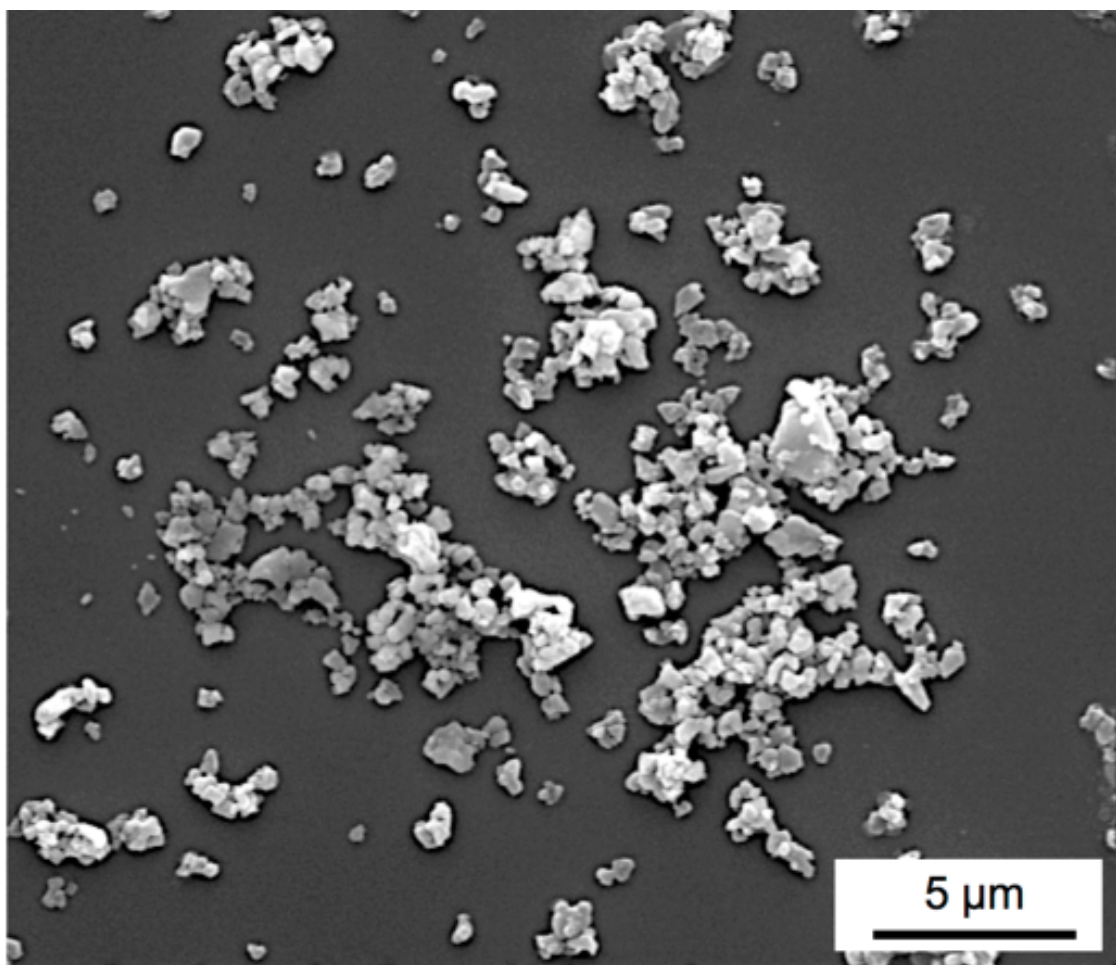


**Figure 2.1.** SEM image of as-received chemically purified Bayer  $\text{Al}_2\text{O}_3$  powder used in this study.

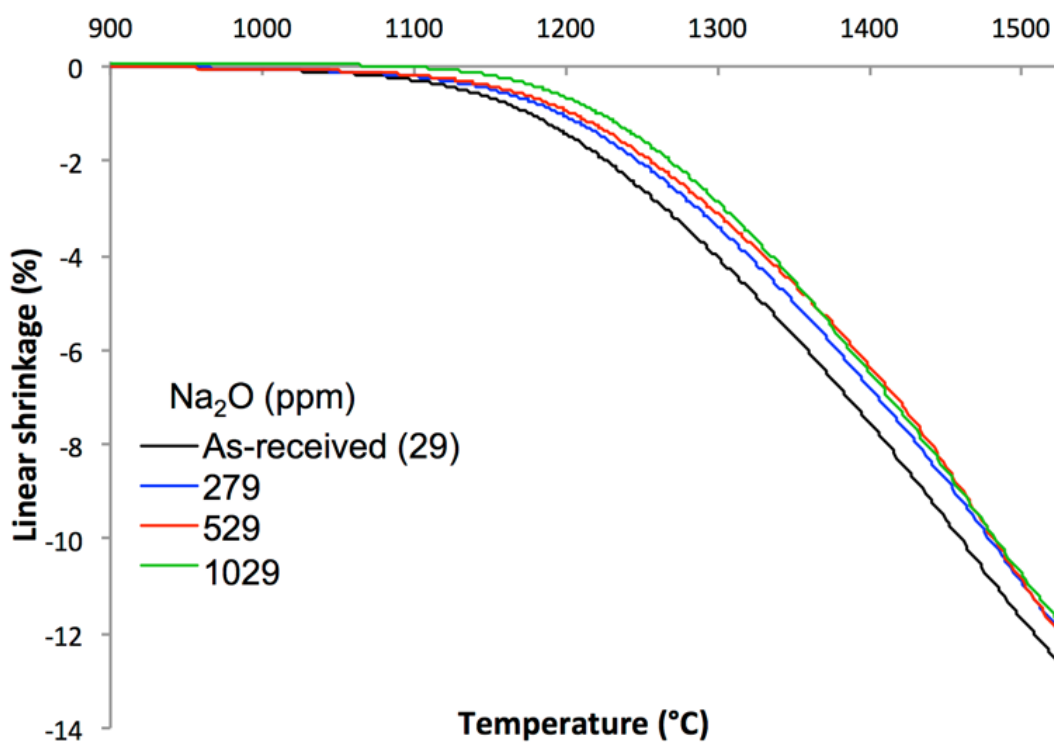


**Figure 2.2.** Dilatometer curves of as-received and singly  $\text{Na}_2\text{O}$ -doped samples heated at  $10^\circ\text{C}/\text{min}$  to  $1525^\circ\text{C}$ .

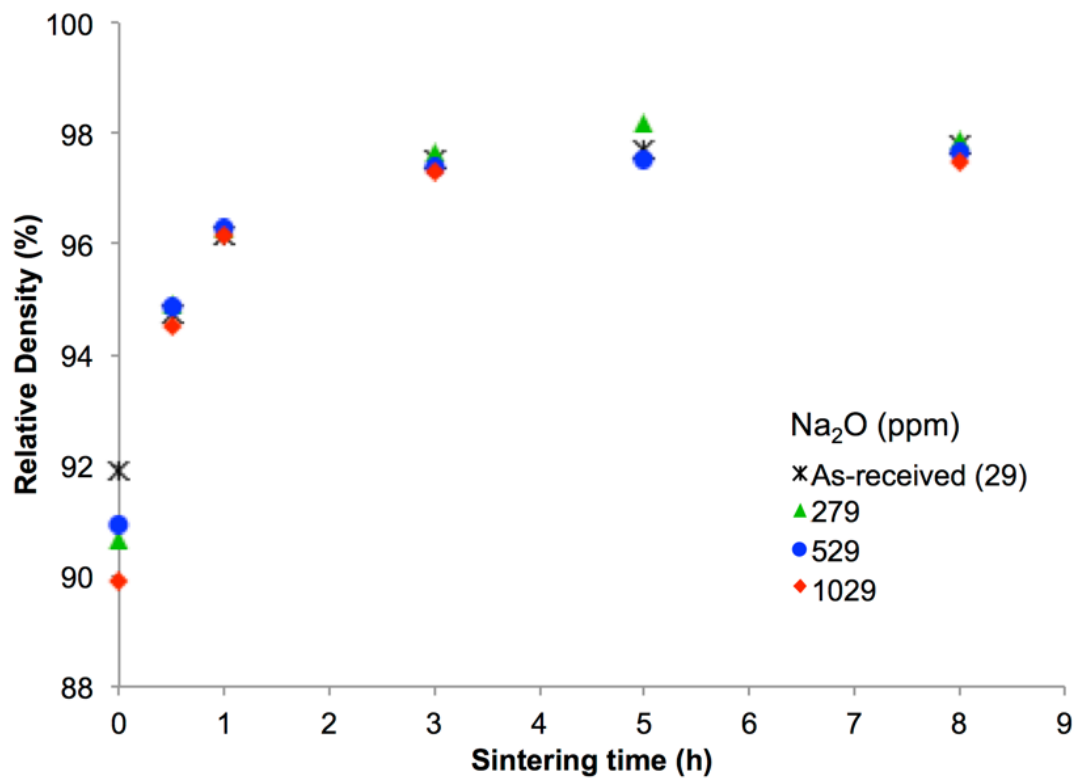


**Figure 2.3.** Densification kinetics of Bayer  $\text{Al}_2\text{O}_3$  doped with different  $\text{Na}_2\text{O}$  concentrations and sintered at  $1525^\circ\text{C}$ .

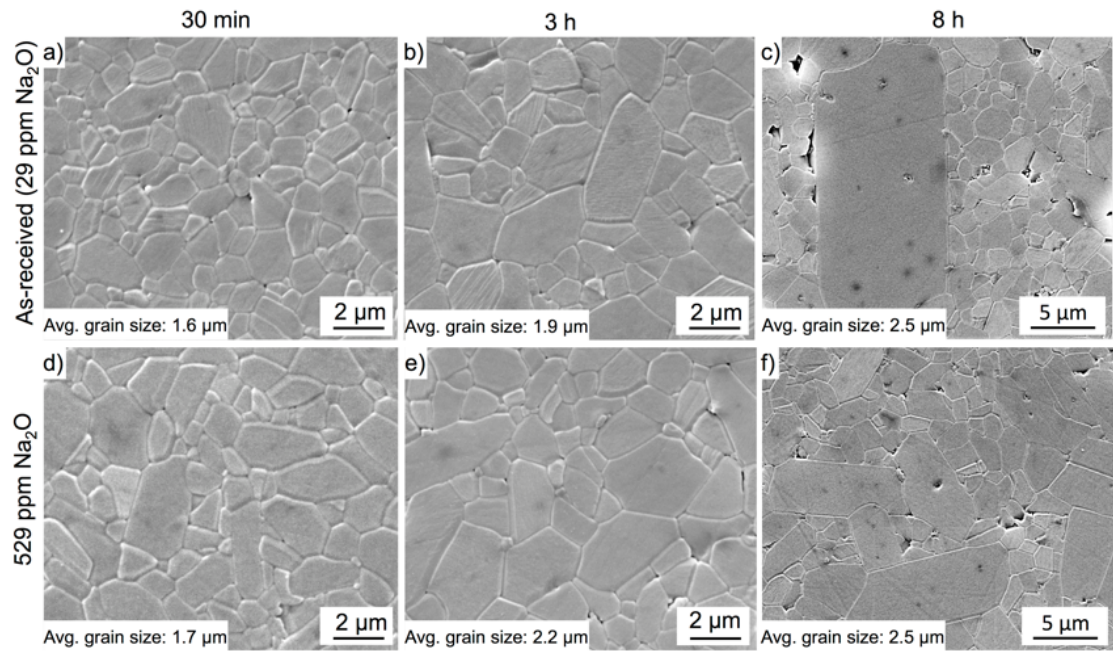


**Figure 2.4.** Microstructures of as-received and singly 529 ppm  $\text{Na}_2\text{O}$  doped samples after 30 min, 3 h and 8 h at 1525°C.

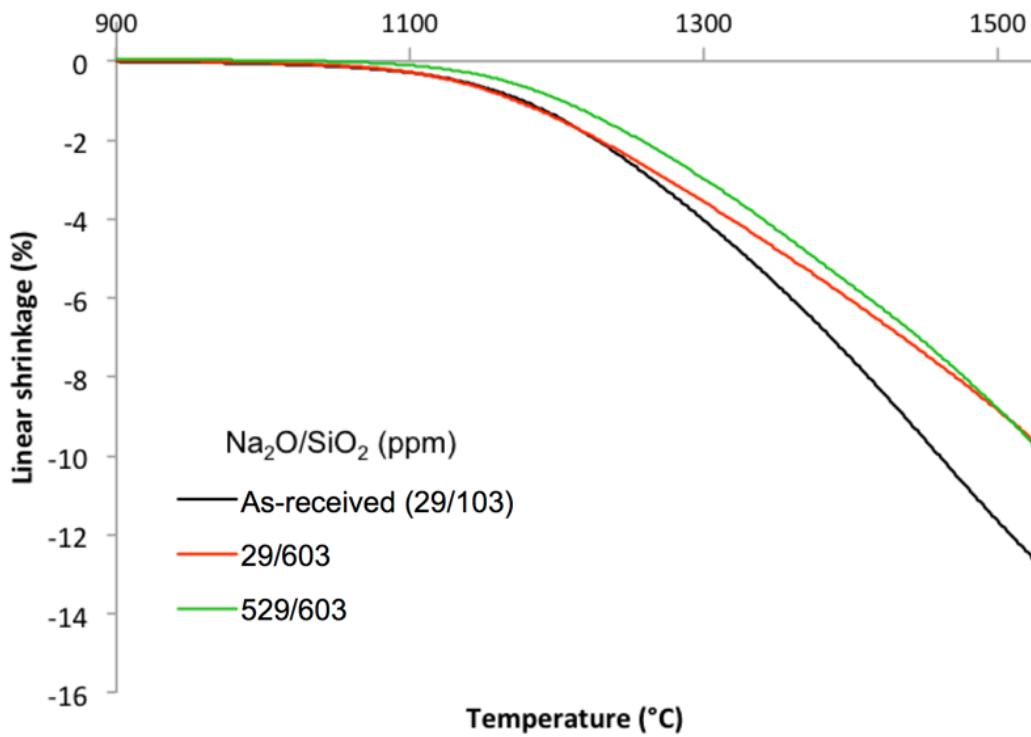


**Figure 2.5.** Dilatometer curves of as-received, singly SiO<sub>2</sub>-doped, and Na<sub>2</sub>O/SiO<sub>2</sub>-doped Bayer Al<sub>2</sub>O<sub>3</sub> heated at 10°C/min to 1525°C.

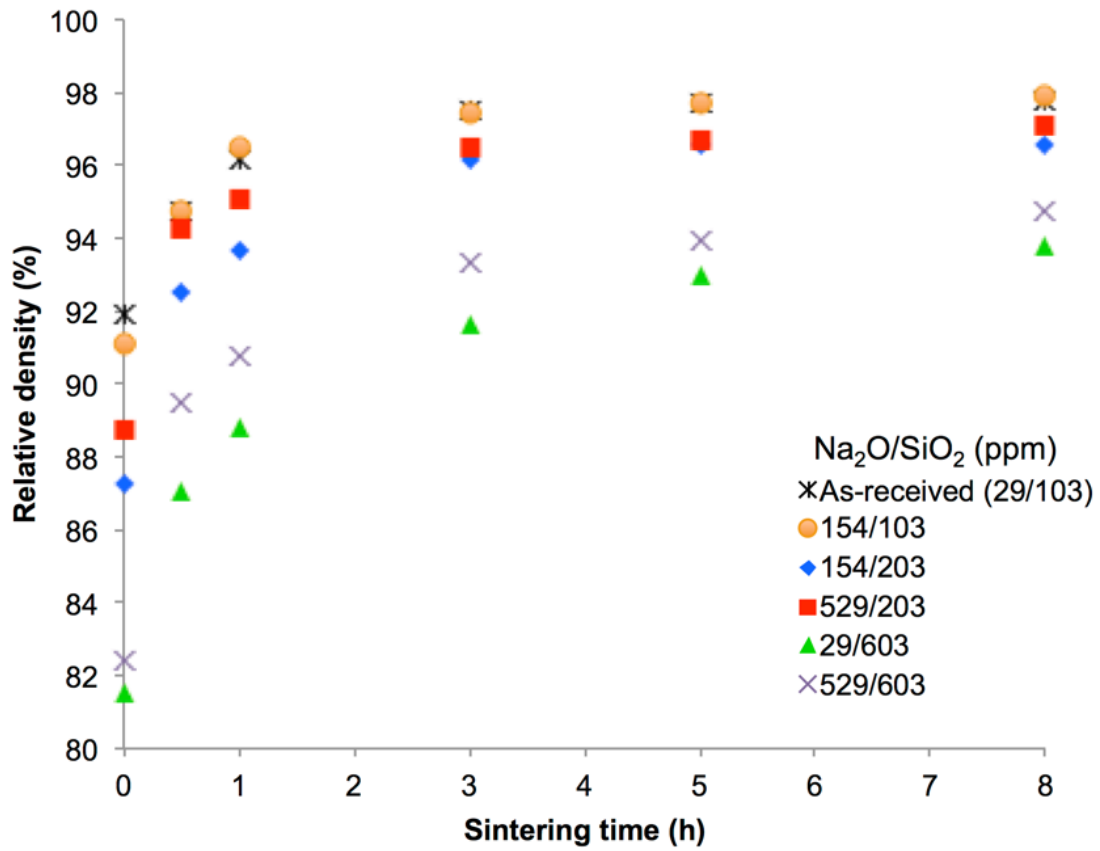


**Figure 2.6.** Densification kinetics of Bayer  $\text{Al}_2\text{O}_3$  doped with different concentrations of  $\text{Na}_2\text{O}$  and  $\text{SiO}_2$  at  $1525^\circ\text{C}$ .

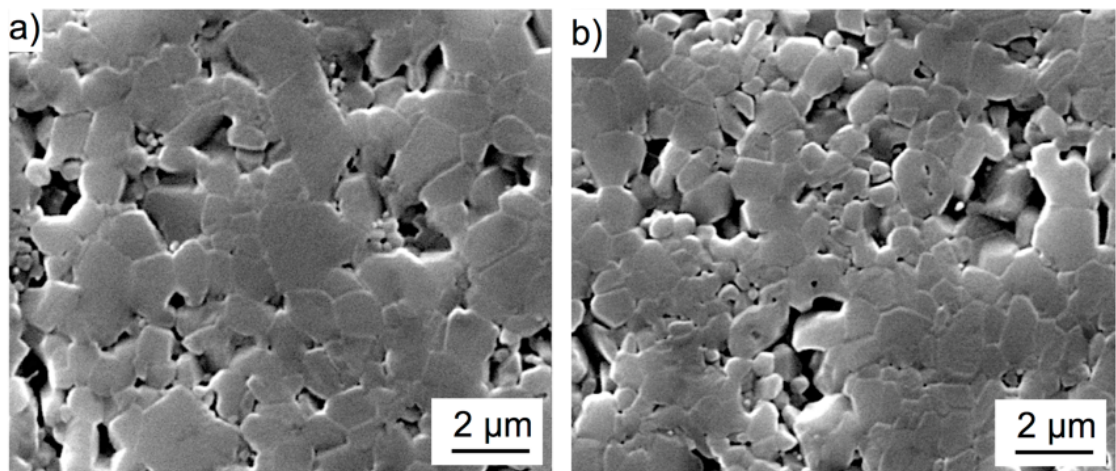


**Figure 2.7.** Microstructures of Bayer  $\text{Al}_2\text{O}_3$  doped with a) 603 ppm  $\text{SiO}_2$  and b) 529 ppm  $\text{Na}_2\text{O}$  and 603 ppm  $\text{SiO}_2$  after heating at  $1525^\circ\text{C}$  for 8h.

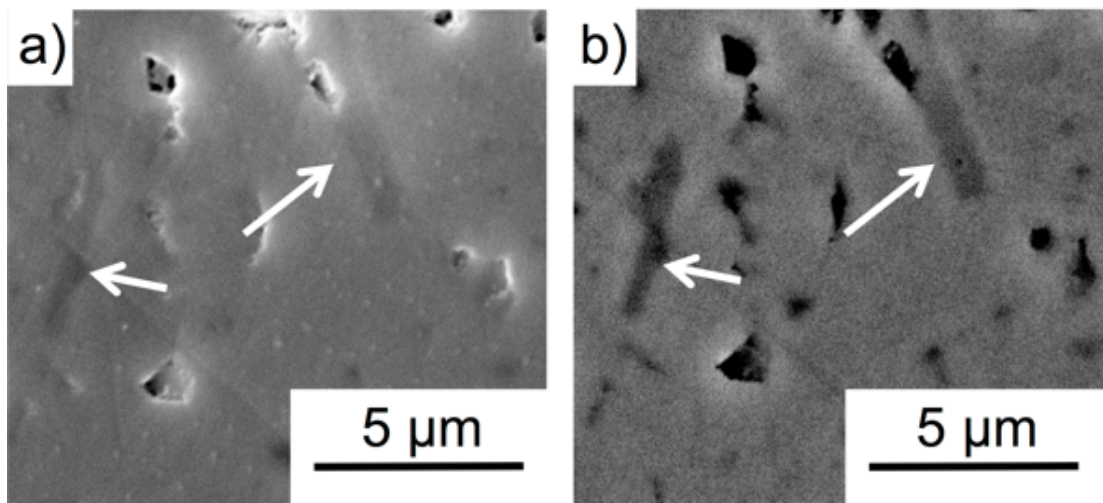


**Figure 2.8.** Micrographs of a sample doped with 1029 ppm  $\text{Na}_2\text{O}$  after sintering at  $1525^\circ\text{C}$  for 3 h. The micrographs were recorded using a) a secondary electron detector and b) a backscattered electron detector. The arrows point at the platelet shaped  $\beta$ -alumina grains that form in samples doped with  $\text{Na}_2\text{O}$ . The samples were not thermally etched.

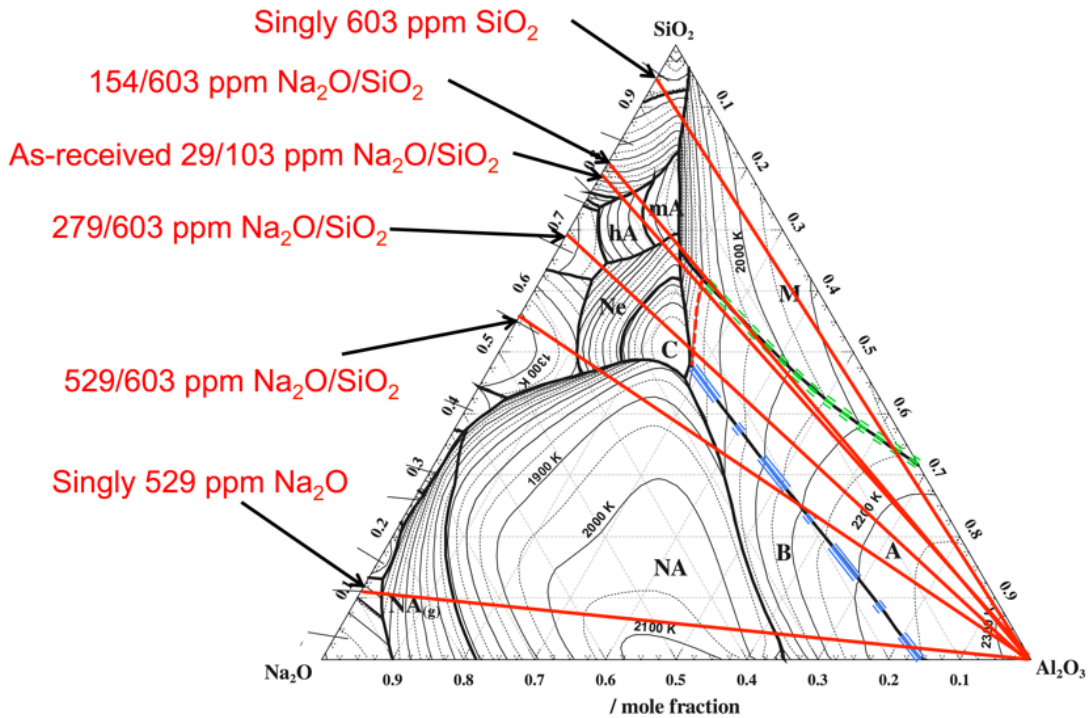


**Figure 2.9.** Liquidus projection of the  $\text{Al}_2\text{O}_3$ - $\text{SiO}_2$ - $\text{Na}_2\text{O}$  ternary phase diagram. The red solid lines are isoplethal cuts representing the samples investigated in this study. The red dashed line is the 1525°C isotherm where  $\alpha$ - $\text{Al}_2\text{O}_3$  and liquid are in equilibrium. The blue dash-dot line and green dotted line are eutectic lines at which  $\alpha$ - $\text{Al}_2\text{O}_3$  and liquid is in equilibrium with  $\beta$ - $\text{Al}_2\text{O}_3$  or mullite, respectively.

# **Chapter 3 | Powder Chemistry Effects on the Sintering Behavior of MgO- doped Bayer Alumina**

## **3.1 Introduction**

Specialty aluminas are generally defined as a calcined or sintered alumina made from a Bayer processed feedstock. These aluminas have specific characteristics to improve their performance in commercial applications, such as defined primary crystal size, surface area, density and shrinkage, and chemical purities in the range of 99.0 - 99.8%. The remaining 1.0 - 0.2% consists of the intentionally added MgO dopant, and impurities such as Na<sub>2</sub>O, CaO, Fe<sub>2</sub>O<sub>3</sub>, and SiO<sub>2</sub> that originate from the bauxite ore or the Bayer process itself. It is well known that trace (ppm) amounts of dopants or impurities can have a significant influence on the sintering of alumina [2, 14, 24]. Since Coble's discovery of MgO doping to produce high-density translucent alumina, there has been high academic and commercial interest in understanding how small concentrations of dopants and impurities characteristic of specialty alumina affect sintering [8, 33, 53–55].

In chapter 2, the influence of Na<sub>2</sub>O and SiO<sub>2</sub> on the sintering of MgO-free specialty alumina was investigated [?]. Na<sub>2</sub>O was shown to initially retard the densification of MgO-free specialty alumina samples, but no effect was observed after extended sintering time (> 30 min) at 1525°C, whereas the addition of SiO<sub>2</sub> to MgO-free specialty alumina formed a liquid phase and significantly retarded

densification throughout the entire sintering process.  $\text{Na}_2\text{O}$  addition to  $\text{SiO}_2$ -doped samples increased the densification rate and degree of densification compared to singly  $\text{SiO}_2$ -doped samples. Based on phase equilibria, the solubility of  $\text{Al}_2\text{O}_3$  in the liquid phase was shown to increase as the  $\text{Na}_2\text{O}$  concentration in the liquid grain boundary phase increases. Furthermore, a higher  $\text{Na}_2\text{O}$  concentration decreases the viscosity of the liquid phase, which further increases the densification rate. Hence, samples with high  $\text{Na}_2\text{O}/\text{SiO}_2$  ratios ( $\geq 0.5$ ) showed higher densities than samples with lower  $\text{Na}_2\text{O}/\text{SiO}_2$  ratios.

$\text{MgO}$  is commonly added to commercial alumina powders because it is known to improve sintering. Several reasonable mechanistic explanations for the beneficial effect of  $\text{MgO}$  include solute-drag, particle-pinning, modification of defect chemistry, increase of surface diffusivity, modification of a liquid phase, and modification of interfacial properties [24]. A model that takes into account the redistribution of  $\text{MgO}$  and  $\text{SiO}_2$  during the sintering of high purity alumina was reported by Handwerker et al. [15] They proposed that  $\text{MgO}$  changes the segregation behavior of glass forming impurities such as  $\text{SiO}_2$  by increasing their solubility in  $\text{Al}_2\text{O}_3$ . This mechanism was supported by the work of Gavrilov et al. [1] who demonstrated by high resolution secondary ion mass spectrometry that the dopants segregate strongly to grain boundaries when high purity  $\text{Al}_2\text{O}_3$  is singly doped with either  $\text{SiO}_2$  or  $\text{MgO}$ , but show a higher solubility in  $\text{Al}_2\text{O}_3$  when co-doped with  $\text{MgO}$  and  $\text{SiO}_2$  due to a defect mechanism in which  $\text{Mg}^{2+}$  and  $\text{Si}^{4+}$  occupy  $\text{Al}^{3+}$  sites and compensate for each other's charge and strain. This model is of particular interest since it considers the direct interaction of  $\text{MgO}$  and  $\text{SiO}_2$ ; an impurity known to negatively affect alumina densification.

In this chapter we report how  $\text{Na}_2\text{O}$  and  $\text{SiO}_2$  influence the sintering of 99.8 - 99.9% pure specialty alumina doped with 380 ppm  $\text{MgO}$ . Dilatometry and sintering kinetics of  $\text{MgO}$ -free specialty alumina samples with similar  $\text{Na}_2\text{O}$  and  $\text{SiO}_2$  concentrations from chapter 2 are compared to the present results to identify the stages at which  $\text{MgO}$  affects densification, and to identify key mechanisms that are responsible for the beneficial effect of  $\text{MgO}$  on the sintering of specialty alumina [?]. High-resolution transmission electron microscopy (TEM) and energy dispersive spectroscopy (EDS) measurements show the distribution of dopants/impurities on grain boundaries. First-principles calculations based on the density functional theory (DFT) were carried out to estimate the relative thermodynamic stability of

MgO, SiO<sub>2</sub>, and MgO+SiO<sub>2</sub> in the alumina lattice.

## 3.2 Experimental

A chemically purified MgO-doped specialty alumina powder (Almatis, Inc., Leetsdale, PA, USA) was chosen for this study. Earlier we studied the influence of SiO<sub>2</sub> and Na<sub>2</sub>O on the sintering of MgO-free specialty alumina using a powder with similar physical and chemical characteristics as the powder used in this study [?]. Since the sample preparation procedures of the two powders were identical, the differences in sintering behavior after doping with similar Na<sub>2</sub>O and SiO<sub>2</sub> concentrations should be attributable primarily to the difference in MgO concentration and its cross effects with Na<sub>2</sub>O and SiO<sub>2</sub> [?].

Physical and chemical characteristics of the powder are shown in Table 3.1 and Figure 3.1. The powder was doped with up to 1000 ppm Na<sub>2</sub>O and 500 ppm SiO<sub>2</sub> using sodium acetate (NaC<sub>2</sub>H<sub>3</sub>O<sub>2.3</sub>H<sub>2</sub>O, ACS grade, BDH, VWR International LLC, West Chester, PA, USA) and tetraethyl orthosilicate (Si(OC<sub>2</sub>H<sub>5</sub>)<sub>4</sub>), 98%, Aldrich Chemical Company, Inc. Milwaukee, WI, USA), respectively, to obtain chemistries similar to commercial high purity specialty aluminas with different liquid volume fractions and different Na<sub>2</sub>O/SiO<sub>2</sub> ratios, as shown in Table 3.2. The detailed doping procedures are described in chapter 2.

Samples with green densities of 59.0 ± 0.5% were fabricated for sintering studies by uniaxial and cold isostatic dry pressing (CIP, Autoclave engineers, Erie, Pa, USA) at 170 MPa and 200 MPa, respectively. The dry pressed cylinders were heated at 10 °C/min to 1525 °C in a thermomechanical analyzer (TMA, Linseis PT1600, Robbinsville, NJ, USA) to record the shrinkage during heating. The kinetics of sintering of samples at 1450 °C and 1525 °C were investigated for up to 8 h. The samples were heated at 10 °C/min to 1200 °C and then at 5 °C/min to the final sintering temperature. The average grain size and density were measured by the linear intercept (ASTM Standard E112-96) [?] and Archimedes methods (ASTM standard B962-15), [?] respectively. The structure and chemistry of grain boundaries were investigated by transmission electron microscopy (TEM) and energy dispersive x-ray spectroscopy EDS using a dual aberration corrected FEI Titan [14] field emission microscope operated at 300 kV and FEI Talos (FEI, Hillsboro, OR, USA) field emission microscope at 200 kV. The EDS on both microscopes is an FEI

Super-X system consisting of four SDDs (Silicon Drift Detectors) with a solid angle of 0.9 srad. The samples for TEM and EDS were air-quenched from the sintering temperature and prepared using a focused ion beam (Quanta 200 3D Dual Beam FIB, FEI, Hillsboro, OR, USA). Grain boundaries were chosen for analysis that were oriented parallel to the TEM beam in order to accurately measure grain boundary widths in the 2D projection images and EDS profiles. Chemical analyses were performed by inductively coupled plasma (ICP) emission spectroscopy (iCap 6000, Thermo Fischer Scientific, Inc., Waltham, MA, USA) after alumina samples were acid digested in a microwave digestion unit equipped with a Teflon sample holder (MARS M, CEM Corp., Matthews, NC, USA).

### 3.3 Computational Methodology

DFT-based first-principles calculations were carried out at 0 K to investigate the thermodynamic stability of clustered defects in the  $\alpha$ -alumina structure. The energy at 0 K without the contribution of the zero-point vibrational energy  $E_0$  was obtained by an equation of state (EOS) fitting using the four-parameter Birch-Murnaghan (BM4) equation as follows [56]:

$$E_0(V) = a + bV^{-\frac{2}{3}} + cV^{-\frac{4}{3}} + dV^{-2} \quad (3.1)$$

where  $a$ ,  $b$ ,  $c$ , and  $d$  are fitting parameters. The EOS fitting is achieved through an energy-volume (E-V) curve of at least 5 different volumes based on the methodology discussed by Shang et al. [56]. The Helmholtz energy  $F(V, T)$  can be predicted as a function of temperature  $T$  and volume  $V$  via [56, 57]:

$$F(V, T) = E_0(V) + F_{vib}(V, T) + F_{T-el}(V, T) \quad (3.2)$$

where  $F_{vib}$  is the temperature-dependent vibrational contribution, and  $F_{T-el}$  is the thermal electronic contribution. At ambient pressure, the Helmholtz energy of the system is equal to the Gibbs energy.

The vibrational contribution was obtained using the Debye-Grüneisen model [56]:

$$F_{vib}(V, T) = \frac{9}{8}k_B\theta_D(V) - k_BT \left[ D \left( \frac{\theta_D(V)}{T} \right) + 3\ln \left( 1 - e^{-\theta_D(V)/T} \right) \right] \quad (3.3)$$

where  $\theta_D$  is the Debye temperature,  $T$  the temperature, and  $D[\theta_D(V)/T]$  the Debye function. The Debye temperature can be calculated by:

$$\theta_D = s \frac{(6\pi^2)^{\frac{1}{3}} \hbar}{k_B} V_0^{\frac{1}{6}} \left( \frac{B_0}{M} \right)^{\frac{1}{2}} \left( \frac{V_0}{V} \right)^\gamma \quad (3.4)$$

where  $s$  is the Debye temperature scaling factor,  $\gamma$  the Grüneisen parameter determined by the pressure derivative of bulk modulus  $B'$ ,  $B_0$  the equilibrium bulk modulus,  $M$  the atomic mass, and  $V_0$  the equilibrium volume. Here, the equilibrium properties  $V_0$ ,  $B_0$ , and  $B'$  are estimated from the EOS of Eq. 3.1. The methodology by Liu et al. [58] was used to calculate the scaling factor of  $\text{Al}_2\text{O}_3$ :

$$s(\nu) = 3^{\frac{5}{6}} \left( 4\sqrt{2} \left( \frac{1+\nu}{1-\nu} \right)^{\frac{3}{2}} + \left( \frac{1+\nu}{1-\nu} \right)^{\frac{3}{2}} \right)^{-\frac{1}{3}} \quad (3.5)$$

where  $\nu$  is the Poisson's ratio, which was calculated by Shang et al. [59]. The thermal electronic contribution was estimated based on the electronic density of states and the Fermi-Dirac statistics [57].

In the present work, the Vienna Ab-initio Simulation Package (VASP) was used to perform the first-principles calculations [60]. The projector augmented-wave (PAW) [61, 62] method was utilized to describe the electron-ion interactions with the exchange correlation functional given by the generalized gradient approximation (GGA-PW91) [63]. A sigma value of 0.2 eV and a plane wave energy cutoff of 1.3 times higher than the highest default cutoff were adopted. The Brillouin zone sampling was carried out with Blöchl corrections using a gamma centered Monkhorst-Pack (MP) scheme [62, 64]. The automated k-points grid generator in VASP was employed with a subdivision length of 80. The energy convergence criterion of the electronic self-consistency was set at  $10^{-5}$  eV/atom for all calculations.

The energies of charge, site, and mass balanced defects in  $\alpha$ -alumina were calculated for defect clusters, i.e. the defects are located next to each other, since this has been shown to be the most stable configuration [65]. The geometric arrangements of each of the clusters were chosen based on previous computational work. Multiple authors showed that a 30-40 atom supercell of  $\text{Al}_2\text{O}_3$  is sufficient to calculate non-charged defects [65–69]. Multiple authors have studied charged and clustered defects in  $\text{Al}_2\text{O}_3$  [65–69]. They showed that different geometric arrangements and supercell size result in little difference in energy and that the

impurity atoms prefer to be clustered due to the binding energy [65–69]. Using this methodology, supercells were generated in the present work with Mg and/or Si clustered, i.e. the Mg-cluster having two Mg atoms substituted for two Al atoms and an oxygen vacancy as nearest neighbors, the Si-cluster having three Si atoms substituted for three Al atoms and an Al vacancy, and the Mg+Si-cluster having one Mg and one Si substituted for two Al atoms.

### 3.4 Sintering and Microstructure Analysis

In chapter 2, it was shown that a glass phase can form during sintering of specialty alumina. Table 3.2 shows the amounts of liquid in the samples at 1525 °C estimated from the  $\text{Al}_2\text{O}_3\text{-Na}_2\text{O}\text{-SiO}_2$  and  $\text{Al}_2\text{O}_3\text{-MgO}\text{-SiO}_2$  phase diagrams based on the amount of  $\text{SiO}_2$ ,  $\text{Na}_2\text{O}$  and  $\text{MgO}$  [70]. It can be seen that the glass volume fraction increases from 0.03 vol.% for  $\text{SiO}_2$  concentrations of 82 ppm to 0.21 vol.% for  $\text{SiO}_2$  concentrations of 582 ppm at 1525 °C.

Figure 3.2 shows the dilatometry curves of MgO-doped and MgO-free [?] samples with different  $\text{Na}_2\text{O}$  and  $\text{SiO}_2$  concentrations heated at 10 °C/min to 1525°C. For samples with  $\text{SiO}_2$  concentrations of 582 ppm the estimated amount of liquid increases from 0.18 vol.% to 0.21 vol.% during heating from 1250 °C to 1525 °C, and for samples with 82 ppm  $\text{SiO}_2$  the amount of liquid phase is estimated from the phase diagram to increase from 0.026 vol.% to 0.030 vol.% during heating from 1250 °C to 1525 °C.

Figure 3.2a shows that the onset of densification of MgO-doped specialty alumina is shifted to higher temperatures for samples with higher  $\text{Na}_2\text{O}$  concentrations. Samples with 560 ppm  $\text{Na}_2\text{O}$  shrink 1% less than samples with 60 ppm  $\text{Na}_2\text{O}$  after heating to 1525 °C. In both the MgO-doped and the MgO-free powders, higher  $\text{SiO}_2$  concentrations retard densification at ~1250 °C. However, the retardation caused by higher  $\text{SiO}_2$  concentrations is less severe in the MgO-doped powder than in the MgO-free powder; e.g. already at 1300 °C, MgO-doped powder samples with 582 ppm  $\text{SiO}_2$  (after the addition of 500 ppm  $\text{SiO}_2$ ) shrink 0.2% less and are 0.5% less dense than samples with 82 ppm  $\text{SiO}_2$ , whereas samples of the MgO-free powder with 603 ppm  $\text{SiO}_2$  shrink 0.5% less and are 3.2% less dense than samples with 103 ppm  $\text{SiO}_2$ . After reaching 1525 °C the dilatometry curves show that MgO-doped samples with 582 ppm  $\text{SiO}_2$  (0.21 vol.% glass) shrink 1.8% less and

are 5.4% less dense than MgO-doped samples with 82 ppm SiO<sub>2</sub> (0.03 vol.% glass). In contrast, the retardation of densification caused by the addition of 500 ppm SiO<sub>2</sub> to the MgO-free powder results in 3.0% less linear shrinkage and 8.7% lower relative densities after heating to 1525 °C. MgO-doped (380 ppm) powder samples with 560 ppm Na<sub>2</sub>O and 582 ppm SiO<sub>2</sub> shrink ~2.5% less than samples with 60 ppm Na<sub>2</sub>O and 82 ppm SiO<sub>2</sub> after reaching 1525 °C, and MgO-free powder samples with 529 ppm Na<sub>2</sub>O and 603 ppm SiO<sub>2</sub> shrink ~3.0% less than samples with 29 ppm Na<sub>2</sub>O and 103 ppm SiO<sub>2</sub> after reaching 1525 °C.

Figure 3.3a and b show how the sintering kinetics of MgO-doped and MgO-free [?] alumina are affected by Na<sub>2</sub>O and SiO<sub>2</sub> after heating at 1450 °C and 1525 °C for up to 8 h. The density of samples with higher SiO<sub>2</sub> concentrations, i.e. higher glass concentrations, is lower for all hold times at 1450 °C and 1525 °C. At 1450 °C MgO-doped powder samples with 0.19 vol.% glass phase (582 ppm SiO<sub>2</sub>) are 6-7% less dense than samples with 0.027 vol.% glass phase (82 ppm SiO<sub>2</sub>), for all hold times (Figure 3.3a). At 1525 °C MgO-doped powder samples with 0.21 vol.% glass phase are ~11% and ~2% less dense than samples with 0.03 vol.% glass phase after heating for 0 h and 8 h, respectively, and samples with 0.03 vol.% glass phase reach densities >98% after 1 h, whereas samples with 0.066 and 0.21 vol.% glass phase are only ~96% and ~94% dense, respectively (Figure 3.3b).

The effect of Na<sub>2</sub>O concentration on densification strongly depends on glass phase concentration. In all samples a higher Na<sub>2</sub>O concentration initially retards densification. For example, after 0 h at 1450 °C the relative density of samples with 0.03 vol.% glass phase and 560 ppm Na<sub>2</sub>O is ~3% lower than the relative density of samples containing the same amount of glass phase and 60 ppm Na<sub>2</sub>O. However, there is no difference in sintered density after 3 h at either 1450 °C or 1525 °C. For samples with higher glass phase concentrations (e.g., 0.21 vol.%) the effect of Na<sub>2</sub>O on the densification is not straightforward, due to the changing Na<sub>2</sub>O/SiO<sub>2</sub> ratio from 0.1 to 0.9 (Table 3.2). Samples with 0.21 vol.% glass phase and Na<sub>2</sub>O/SiO<sub>2</sub> ratios of 0.9 are 1-2% denser than samples with 0.21 vol.% glass phase and Na<sub>2</sub>O/SiO<sub>2</sub> ratios of 0.1. However, after 30 min at 1525 °C the relative density of samples with 0.21 vol.% glass phase and Na<sub>2</sub>O/SiO<sub>2</sub> ratios of 0.9 in the glass phase is 0.9% lower than the relative density of samples with 0.21 vol.% glass phase and Na<sub>2</sub>O/SiO<sub>2</sub> ratios of 0.1 in the glass phase, and after 1 h or longer at 1525 °C there is no difference in relative density. Samples with 0.066 vol.% glass

phase are 98.3 - 98.6% dense after 8 h at 1525 °C, and samples with 0.21 vol.% glass phase are 97.1% - 97.5% dense after 8 h at 1525 °C.

Comparing the as-received MgO-free and MgO-doped powders with 0.03 vol.% glass phase shows that doping with 380 ppm MgO leads to 1% higher densities for all hold times at 1525 °C (Figure 3.3b and c) [?]. After 8 h at 1525 °C the MgO-doped samples with 0.21 vol.% glass phase are ~2% less dense than samples with 0.03 vol.% glass phase, whereas the addition of 500 ppm SiO<sub>2</sub> (total of 603 ppm SiO<sub>2</sub> and 0.22 vol.% glass) to the MgO-free powder leads to ~4% less dense samples [?]. MgO-free and MgO-doped specialty alumina samples containing 0.22 and 0.21 vol.% glass phase, respectively, and global Na<sub>2</sub>O/SiO<sub>2</sub> ratios of 0.9 show initial retardation of densification compared to samples with Na<sub>2</sub>O/SiO<sub>2</sub> ratios of 0.1, but have higher densities than samples with Na<sub>2</sub>O/SiO<sub>2</sub> ratios of 0.1 after further heating. This increased densification can be explained by the increased solubility of Al<sub>2</sub>O<sub>3</sub> into the liquid grain boundary phase and the higher diffusivity (lower viscosity of the grain boundary phase) as the Na<sub>2</sub>O/SiO<sub>2</sub> ratio increases [?, 47]. However, after hold times of 1 h or longer at 1525 °C, MgO-free powder samples with 0.22 vol.% glass phase and Na<sub>2</sub>O/SiO<sub>2</sub> ratios of 0.9 are 1% denser than samples with 0.22 vol.% glass phase and Na<sub>2</sub>O/SiO<sub>2</sub> ratios of 0.1, whereas MgO-doped powder samples with 0.21 vol.% and Na<sub>2</sub>O/SiO<sub>2</sub> ratios of 0.9 have the same densities as samples with 0.21 vol.% glass phase and Na<sub>2</sub>O/SiO<sub>2</sub> ratios of 0.1.

The microstructures of samples with different vol.% glass phase and different Na<sub>2</sub>O/SiO<sub>2</sub> ratios heated at 1525 °C for 8 h are shown in Figure 3.4. Samples with 60 ppm Na<sub>2</sub>O show mostly equiaxed grains, regardless of the glass phase concentration in the samples (Figures 3.4a and c). Samples with 560 ppm Na<sub>2</sub>O (Figures 3.4b and d) show more faceted α-Al<sub>2</sub>O<sub>3</sub> grains and appear to have a wider grain size distribution than samples with 60 ppm Na<sub>2</sub>O. These effects are more pronounced in samples with higher glass concentrations. The grain sizes of samples with 0.21 vol.% glass are less than the grain sizes of samples with 0.03 vol.% glass phase.

The average grain sizes of samples with different vol.% glass phase and different Na<sub>2</sub>O/SiO<sub>2</sub> ratios are plotted as a function of relative density in Figure 3.5. Grain growth starts when the final sintering stage is reached, between 85 and 92% relative density. Samples with 0.03 vol.% glass phase and 60 ppm Na<sub>2</sub>O show a three-fold increase in grain size, from 0.5 μm to ~1.5 μm, when the relative density increases

from 68% to 99%, and samples with 0.03 vol.% glass phase and 560 ppm Na<sub>2</sub>O have a somewhat larger grain size of 2.2  $\mu\text{m}$  at 99% relative density. When relative densities of ~99% are reached in samples with 0.03 vol.% glass, the grain size increases to 3.1 - 3.4  $\mu\text{m}$  when heated at 1525 °C for 8 h. Samples with higher glass concentrations have a similar trajectory up to 92% density. However, at densities >92 % grain growth is enhanced in samples with higher glass concentrations, and at 97 - 97.5% density higher glass phase concentrations of 0.21 and 0.17 vol.% lead to a larger grain size of 2.6 and 2.4  $\mu\text{m}$ , respectively, compared to samples with 0.03 vol.% glass phase (~1.5  $\mu\text{m}$  grain size).

### 3.5 Mechanistic Interpretation

If the mechanism of MgO increasing the solubility of SiO<sub>2</sub> in alumina, as proposed by Handwerker et al., [15] is responsible for the improved sintering behavior of alumina, then the amount of liquid phase in MgO-doped alumina should be less than calculated and less than in MgO-free samples, and, the grain boundary thickness in MgO-doped alumina should be less than in MgO-free powder. The reduced grain boundary thickness in MgO-doped alumina should lead to an change in grain boundary chemistry and different sintering behavior after this co-dissolution has occurred compared to MgO-free alumina.

Comparing the dilatometry curves and sintering kinetics of MgO-doped and MgO-free specialty alumina powders with different chemistries indicates that there are two stages at which MgO affects densification. At 1250 °C increased glass phase content retards densification, and at the same stage there is an enhancement of densification due to MgO. This suggests that there is a direct interaction between the glass phase and MgO at this stage, where MgO mitigates the negative effect of the glass phase, probably by modifying the properties of the liquid grain boundary phase. The Al<sub>2</sub>O<sub>3</sub>-SiO<sub>2</sub>-MgO phase diagram suggests that MgO increases the solubility of Al<sub>2</sub>O<sub>3</sub> in the liquid, and MgO can lower the viscosity of the glass melt, [50] which results in higher diffusion coefficients. The enhanced diffusion associated with the lower viscosity and higher solubility of Al<sub>2</sub>O<sub>3</sub> in the glass phase can explain why MgO positively affects the sintering of alumina at stages when SiO<sub>2</sub> would negatively affect densification.

The second stage at which MgO affects densification is after 1 h at 1525 °C.

MgO-free powder samples with 0.22 vol.% glass phase and Na<sub>2</sub>O/SiO<sub>2</sub> ratios of 0.9 have 1-2% higher relative densities than samples with 0.22 vol.% glass phase and Na<sub>2</sub>O/SiO<sub>2</sub> ratios of 0.1 for all hold times at 1525 °C. In previous work we calculated an expected grain boundary thickness of 1.3 nm for samples with 0.22 vol.% glass phase after 3 h at 1525 °C, based on the observed grain size of 1.6 μm. The addition of 500 ppm Na<sub>2</sub>O increases the Na<sub>2</sub>O/SiO<sub>2</sub> ratio from 0.1 to 0.9, which modifies the liquid grain boundary phase and enhances densification [?]. Figure 3.6 shows a high-resolution TEM image of a grain boundary of a MgO-free powder [?] sample (2 ppm MgO) with 0.22 vol.% glass phase and a Na<sub>2</sub>O/SiO<sub>2</sub> ratio of 0.9 after 3 h at 1525 °C. It can be seen that the measured grain boundary thickness of 1.7 nm is close to the grain boundary thickness calculated based on the amount of glass phase in the sample. MgO-doped powder samples with 0.21 vol.% glass phase and Na<sub>2</sub>O/SiO<sub>2</sub> ratios of 0.9 have 1-2% higher densities than samples with 0.21 vol.% glass phase and Na<sub>2</sub>O/SiO<sub>2</sub> ratios of 0.1 for most hold times at 1450 °C and for hold times < 30 min at 1525 °C. This difference in densification behavior is similar to the densification behavior of MgO-free powder samples, which suggests the presence of a liquid phase that is modified by Na<sub>2</sub>O, as seen in the MgO-free alumina samples.

Figure 3.7a shows a high resolution TEM image of a grain boundary in an MgO-doped alumina sample with 0.21 vol.% glass phase and a Na<sub>2</sub>O/SiO<sub>2</sub> ratio of 0.9 after 0 h at 1525 °C. The measured grain boundary thickness of ~1.4 nm for this sample is in agreement with the theoretically estimated [?] grain boundary thickness. However, after 1 h or longer at 1525 °C, samples with 0.21 vol.% glass and Na<sub>2</sub>O/SiO<sub>2</sub> ratios of 0.9 have the same densities as samples with 0.21 vol.% glass and Na<sub>2</sub>O/SiO<sub>2</sub> ratios of 0.1, and the grain boundary thicknesses of those samples after 3 h at 1525 °C are ~0.3 nm (Figure 2.7b) and substantially thinner than the calculated grain boundary thicknesses of 1.4 nm.

The thinner grain boundary suggests that the addition of MgO causes a reduction of the amount of liquid phase in the grain boundaries after longer time at 1525 °C. In the literature it is reported that excess liquid phase, after an equilibrium grain boundary thickness [71] is reached, can accumulate in triple pockets. However, we did not observe any triple pockets in the 380 ppm MgO-doped samples with 0.21 vol.% glass. Therefore, the impurities and dopants that formed the liquid phase after 0 h have to be distributed elsewhere in the sample after 3 h at 1525

°C. Since  $\text{SiO}_2$ -containing second phases, such as mullite or cordierite, were not observed in the samples, we hypothesize that  $\text{SiO}_2$  and  $\text{MgO}$  form a solid solution in  $\alpha$ -alumina, as proposed by Handwerker et al. [15]. This co-dissolution mechanism would significantly reduce the total amount of  $\text{SiO}_2$  and, therefore, the liquid phase content in the samples and in the grain boundaries.

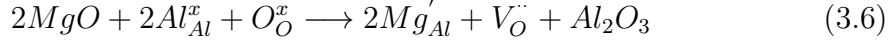
The EDS maps in Figure 2.8 show the distribution of Si around a grain boundary in  $\text{MgO}$ -doped samples with a calculated glass concentration of 0.21 vol.% after 0 h and 3 h at 1525 °C. Figure 2.9 shows the corresponding EDS line scans for Si and Mg across the grain boundaries. It can be seen that after 0 h at 1525 °C  $\text{SiO}_2$  and  $\text{MgO}$  are strongly concentrated in the grain boundaries, and a chemical grain boundary thickness,  $\delta_{chem}$ , of  $\sim 1.7$  nm is estimated (Figures 2.8a and 2.9a), which is close to the structural grain boundary thickness of 1.4 nm measured from the high resolution TEM image (Figure 2.7a). After 3 h at 1525 °C  $\text{MgO}$  and  $\text{SiO}_2$  are still concentrated on the grain boundary, however, the chemical grain boundary thickness,  $\delta_{chem}$ , is  $\sim 3.2$  nm (Figure 2.8b and 2.9b) and substantially thicker than the observed structural grain boundary thickness,  $\delta_{str}$ , of  $\sim 0.3$  nm (Figure 2.7b). This difference in structural and chemical grain boundary thickness after 3 h supports the argument that  $\text{MgO}$  and  $\text{SiO}_2$  form a solid solution in the alumina lattice in the near grain boundary region. If we assume that equal amounts of  $\text{MgO}$  and  $\text{SiO}_2$  dissolve into the alumina lattice to form the proposed defect complex, and that all  $\text{MgO}$  in the sample is consumed by this process, then 380 ppm  $\text{SiO}_2$  must be removed from the amorphous grain boundary phase. This would leave 202 ppm  $\text{SiO}_2$  in the grain boundaries to form the amorphous film with a calculated grain boundary thickness of 0.5 nm, which is close to the observed grain boundary thickness of 0.3 nm [?].

To further evaluate whether  $\text{MgO}$  and  $\text{SiO}_2$  form a solid solution in  $\alpha$ -alumina we conducted first-principles calculations based on density functional theory to gain insight into the thermodynamic stability of  $\text{Mg}^{2+}$  and  $\text{Si}^{4+}$  by themselves and together in the  $\alpha$ -alumina structure. To ensure the accuracy of the calculations, the lattice parameters and energy of the  $\alpha$ -alumina structure without any substitutions are compared with previous experiments and calculations in Table 3.3. It can be seen that the calculated lattice parameters match well with experimental values and lattice parameters from previous first-principles calculations [65, 72–76]. The difference between the present and past first-principles calculations can be attributed

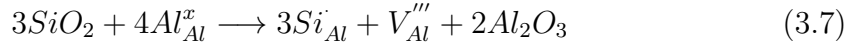
to the different input parameters used.

We calculated the energy of a unit cell of the  $\tilde{\text{I}}$ -alumina structure with substitutions according to the following balanced equations:

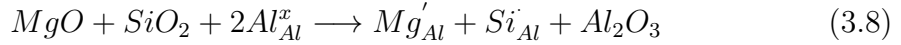
Mg-Cluster:



Si-Cluster:



Mg+Si-Cluster:



Defect simulations of aliovalent cation substitutions in alumina [65] showed that the dominant compensation mechanisms for  $\text{Mg}^{2+}$  and  $\text{Si}^{4+}$  by themselves in alumina are the formation of oxygen and aluminum vacancies, respectively (Eq. 3.6 and 3.7). In Eq. 3.8  $\text{Mg}^{2+}$  and  $\text{Si}^{4+}$  compensate for each other's charge and the formation of vacancies or interstitials is unnecessary to account for dissolution in the alumina lattice. The calculations were carried out for clustered defects since they are lower in energy than isolated defects [65]. The structures were relaxed and the formation energies as a function of temperature with bulk  $\text{Al}_2\text{O}_3$  as the reference state are plotted in Figure 3.10. It can be seen that the formation energy for the Mg+Si-cluster,  $E_{\text{Form}}^{\text{Mg+Si}}$ , is lower than the formation energies of the Mg-cluster,  $E_{\text{Form}}^{\text{Mg}}$ , and the Si-cluster,  $E_{\text{Form}}^{\text{Si}}$ , which indicates that the Mg+Si-cluster is more stable than the Mg-cluster and the Si-cluster. Since two  $\text{Mg}^{2+}$  ions and three  $\text{Si}^{4+}$  ions are necessary to form the Mg-cluster and Si-cluster, respectively, but only one  $\text{Mg}^{2+}$  and one  $\text{Si}^{4+}$  are required to form the Mg+Si-cluster, the formation energies of the clusters can be compared by

$$\Delta E_{\text{Form}} = E_{\text{Form}}^{\text{Mg+Si}} - \left( \frac{1}{3}E_{\text{Form}}^{\text{Si}} + \frac{1}{2}E_{\text{Form}}^{\text{Mg}} \right) \quad (3.9)$$

The formation energy difference,  $\Delta E_{\text{Form}}$ , is plotted in Figure 3.10 and it can be seen that  $\Delta E_{\text{Form}}$  is negative at all temperatures, which means that the Mg+Si-

cluster is more energetically favored to form than the Mg-cluster or Si-cluster. This indicates that MgO and SiO<sub>2</sub> have a higher co-solubility in  $\alpha$ -alumina than MgO or SiO<sub>2</sub> by themselves. In  $\alpha$ -alumina the Al<sup>3+</sup> cation sites are 6-fold coordinated and Al<sup>3+</sup> has an effective ionic radius of 53.5 pm, while the radii of Mg<sup>2+</sup> and Si<sup>4+</sup> are 72 pm and 40 pm, respectively. Therefore, Mg<sup>2+</sup> and Si<sup>4+</sup> can compensate for each other's size and charge difference relative to Al<sup>3+</sup> in the  $\alpha$ -alumina lattice, which explains the lower energy of the Mg+Si-cluster. The stable phases for MgO and/or SiO<sub>2</sub> and Al<sub>2</sub>O<sub>3</sub> are spinel, cordierite, and mullite. However, we hypothesize that if both MgO and SiO<sub>2</sub> are present at low concentrations, then it is more favorable for MgO and SiO<sub>2</sub> to form a solid solution in the  $\alpha$ -alumina structure than to form a second phase or remain in the grain boundaries as a siliceous liquid phase.

The described mechanism could also influence the distribution of other oxides in the samples, such as Fe<sub>2</sub>O<sub>3</sub>, CaO, and Na<sub>2</sub>O. Figure 3.11 shows the element distribution obtained from EDS of two grain boundaries in samples sintered at 1525 °C for 0 h and 3 h, respectively. Figures 3.11a and e show the segregation of MgO to the grain boundaries after 0 h and 3 h, respectively, and it can be seen that after 0 h at 1525 °C Mg is more strongly concentrated in the grain boundary than after 3 h at 1525 °C, due to the mechanism described above. From Figures 3.11b and f it can be seen that there is no segregation of Fe<sub>2</sub>O<sub>3</sub> and we believe that Fe<sub>2</sub>O<sub>3</sub> is in solid solution in the alumina lattice, [65] since the Al<sub>2</sub>O<sub>3</sub>-Fe<sub>2</sub>O<sub>3</sub> phase diagram shows considerable solubility [77]. Figures 3.11c, d, g, and h show that there is a slightly higher Na and Ca signal coming from the grain boundaries, indicating that Na and Ca segregate to the grain boundaries and are components of the liquid grain boundary phase. Ca is more concentrated in the grain boundary after 3 h at 1525 °C, due to the narrower grain boundary thickness (Figure 3.7b).

It can be seen that the Na signal after 0 h at 1525 °C (Figure 3.11c) shows a slight segregation of Na to the grain boundary, but after 3 h at 1525 °C (Figure 3.11g) no segregation can be observed. It should also be noted that it is challenging to detect Na using EDS since the Na signal disappears quickly after the high-voltage electron beam is focused on the grain boundary. Therefore, we believe that there is still Na on the grain boundaries, even though the EDS map does not show an increased Na signal. However, since the Na signal is lower, we believe that after 3 h at 1525 °C there is less Na<sub>2</sub>O on the grain boundaries than after 0 h at 1525 °C. The reduced amount of Na might be a result of volatilization of Na<sub>2</sub>O during sintering.

Figure 3.12 shows the influence of sintering time and temperature on the  $\text{Na}_2\text{O}$  concentration, obtained by ICP analysis, during sintering for samples with target concentrations of 560 ppm  $\text{Na}_2\text{O}$ . It can be seen that there is no observable  $\text{Na}_2\text{O}$  loss as a function of temperature up to 1525 °C (Figure 3.12a), but after heating to 1600 °C there is a loss of  $\sim$ 200 ppm or a  $\sim$ 35% decrease in  $\text{Na}_2\text{O}$  concentration. After sintering at 1525 °C for 30 min the  $\text{Na}_2\text{O}$  concentration decreases by about 200 ppm, but remains constant at  $\sim$ 350 ppm when heated to 1525 °C for up to 8 h (Figure 3.12b). Between 1300 °C and 1525 °C the  $\text{Na}_2\text{O}$  concentration is constant at  $\sim$ 510 ppm, which is 50 ppm below the target level. The lower  $\text{Na}_2\text{O}$  concentration might be due to volatilization at earlier stages. During heating at 1525 °C  $\text{Na}_2\text{O}$  loss can be observed between 0 and 30 min hold time, which can explain the lower Na signal in Figure 3.11g.

As explained earlier, the described dissolution of  $\text{MgO}$  and  $\text{SiO}_2$  into the alumina lattice reduces the amount of glass phase in the grain boundaries. Since only  $\text{SiO}_2$  is removed from the glass phase and other components of the glass phase, such as  $\text{CaO}$  and  $\text{Na}_2\text{O}$  remain, the grain boundaries can supersaturate. This can eventually lead to the nucleation of second phases, which was observed for samples with lower  $\text{SiO}_2$  concentrations of 82 and 182 ppm.

## 3.6 Summary and Conclusion

The effect of  $\text{MgO}$  on the sintering of specialty alumina powders with different chemistries was analyzed by comparing the sintering kinetics of  $\text{MgO}$ -free and  $\text{MgO}$ -doped specialty aluminas with different impurity levels and ratios of  $\text{Na}_2\text{O}$  and  $\text{SiO}_2$ . TEM images of grain boundaries shows that the grain boundary thickness of  $\text{MgO}$ -doped specialty alumina is reduced during densification at 1525 °C and are thinner than observed in  $\text{MgO}$ -free specialty alumina. EDS analysis suggests that  $\text{MgO}$  and  $\text{SiO}_2$  have an increased co-solubility in the alumina lattice when present together. This co-dissolution mechanism was supported by DFT-based first-principles calculations showing that the formation energy of  $\text{MgO}$  and  $\text{SiO}_2$  together in the alumina lattice is lower than the formation energies of  $\text{MgO}$  or  $\text{SiO}_2$  by themselves in the alumina lattice. The reduced amount of  $\text{SiO}_2$  on the grain boundaries of  $\text{MgO}$ -doped alumina leads to enhanced densification compared to  $\text{MgO}$ -free alumina because  $\text{SiO}_2$  has been shown to retard densification.

The present study supports the hypothesis of Handwerker et al. [15] and high resolution SIMS observations of Gavrilov et al. [1] that the key mechanism responsible for the beneficial effect of MgO on the sintering of alumina is the reduction of amorphous phase in the grain boundaries by increasing the solubility of SiO<sub>2</sub> in the alumina lattice.

**Table 3.1.** Physical and chemical characteristics of the as-received 380 ppm MgO-doped specialty alumina powder used in this study.

BET ( $\text{m}^2/\text{g}$ )	7.3
$D_{50}$ ( $\mu\text{m}$ )	0.4
$D_{90}$ ( $\mu\text{m}$ )	1.4
	ICP (ppm)
$\text{Al}_2\text{O}_3$	99.92 %
$\text{SiO}_2$	82
$\text{Na}_2\text{O}$	60
$\text{Fe}_2\text{O}_3$	140
$\text{CaO}$	51
$\text{TiO}_2$	8
MgO	380

**Table 3.2.** Calculated compositions and amounts of liquid in 380 ppm MgO-doped specialty alumina samples of different chemistries at 1450°C and 1525 °C.

Na <sub>2</sub> O/SiO <sub>2</sub> concentration		Global Na <sub>2</sub> O/SiO <sub>2</sub> ratio	Na <sub>2</sub> O:SiO <sub>2</sub> ratio in the liquid	Vol. % of liquid in sample	
ppm by wt.	ppm by mole			1450 °C	1525 °C
60/82 - 560/82	99/139 - 921/139	0.7 - 6.6	0.5	0.027	0.030
185/182 - 560/182	304/309 - 921/309	1.0 - 3.0	0.5	0.060	0.066
60/582	99/987	0.1	0.1	0.19	0.21
560/582	921/987	0.9	0.5	0.19	0.21

**Table 3.3.** Lattice parameters and equilibrium energy ( $E_0$ ) compared to previous first-principles and experimental values.

Reference	$E_0$ (eV/atom)	$a$ (Å)	$b$ (Å)	$c$ (Å)
This work	-7.48	4.76	4.76	12.99
Calc [72–76]	-7.48	4.78	4.78	13.00
Expt [65]		4.76	4.76	13.00

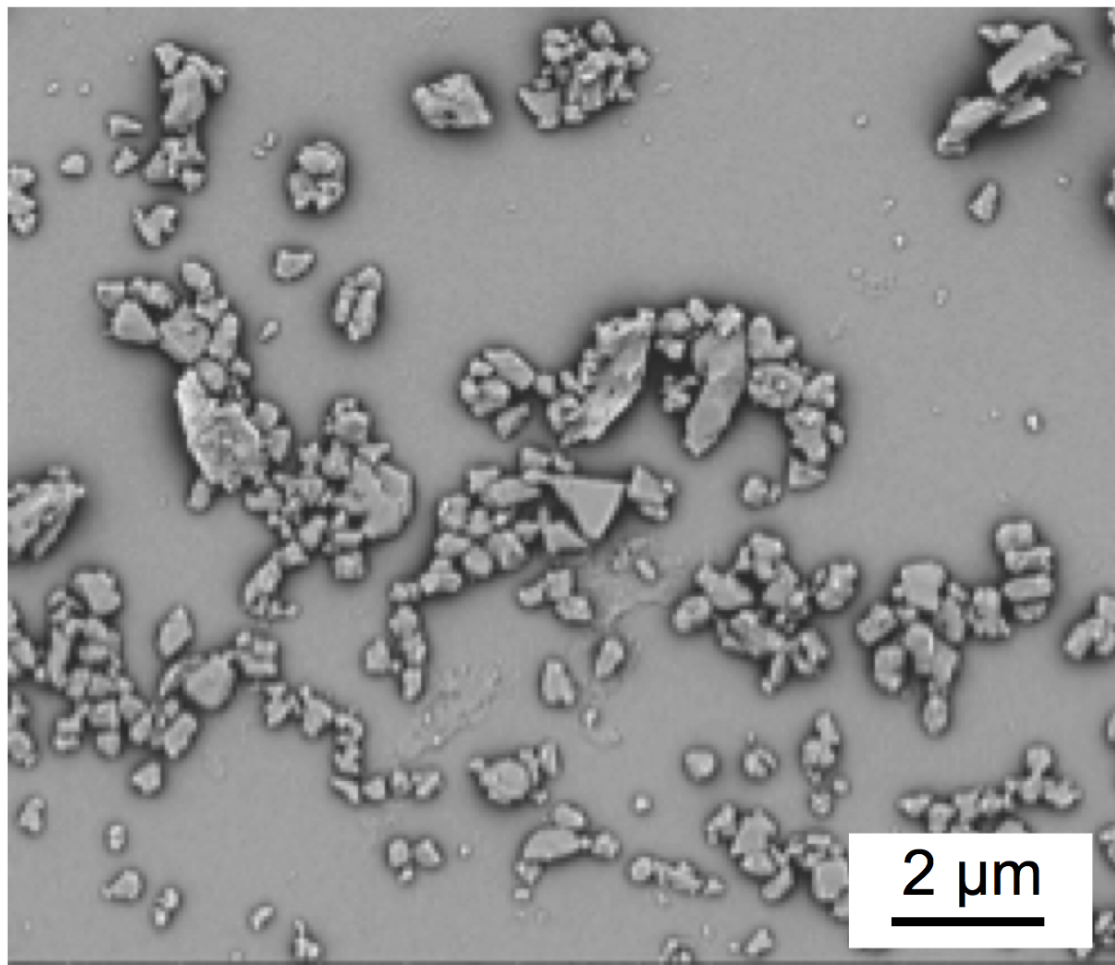


**Figure 3.1.** SEM image of 380 ppm MgO-doped specialty alumina powder used in this work.

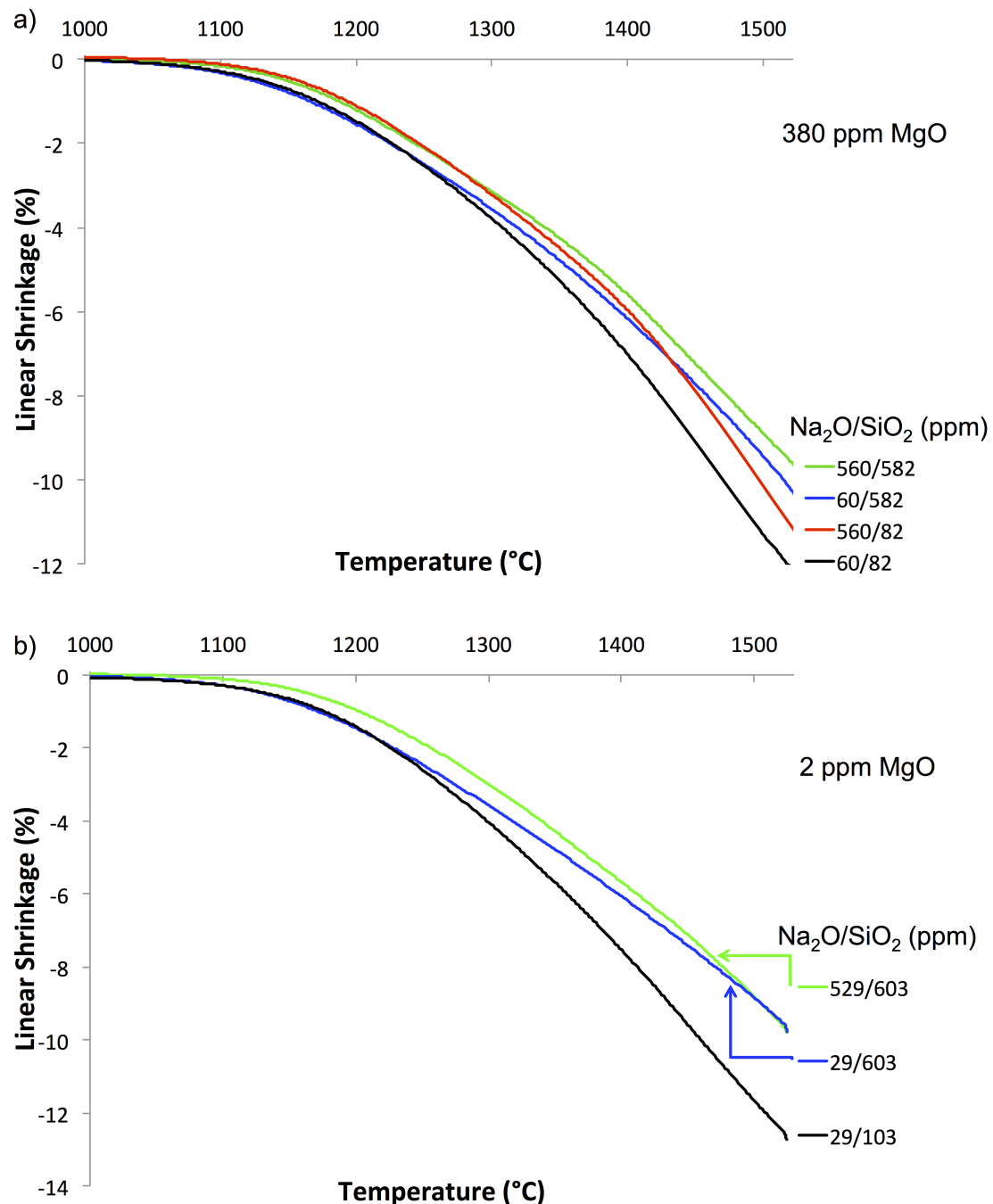


**Figure 3.2.** Dilatometer curves of a) 380 ppm MgO-doped and b) MgO-free [2] specialty alumina samples with different  $\text{Na}_2\text{O}/\text{SiO}_2$  levels heated at 10°C/min to 1525°C.

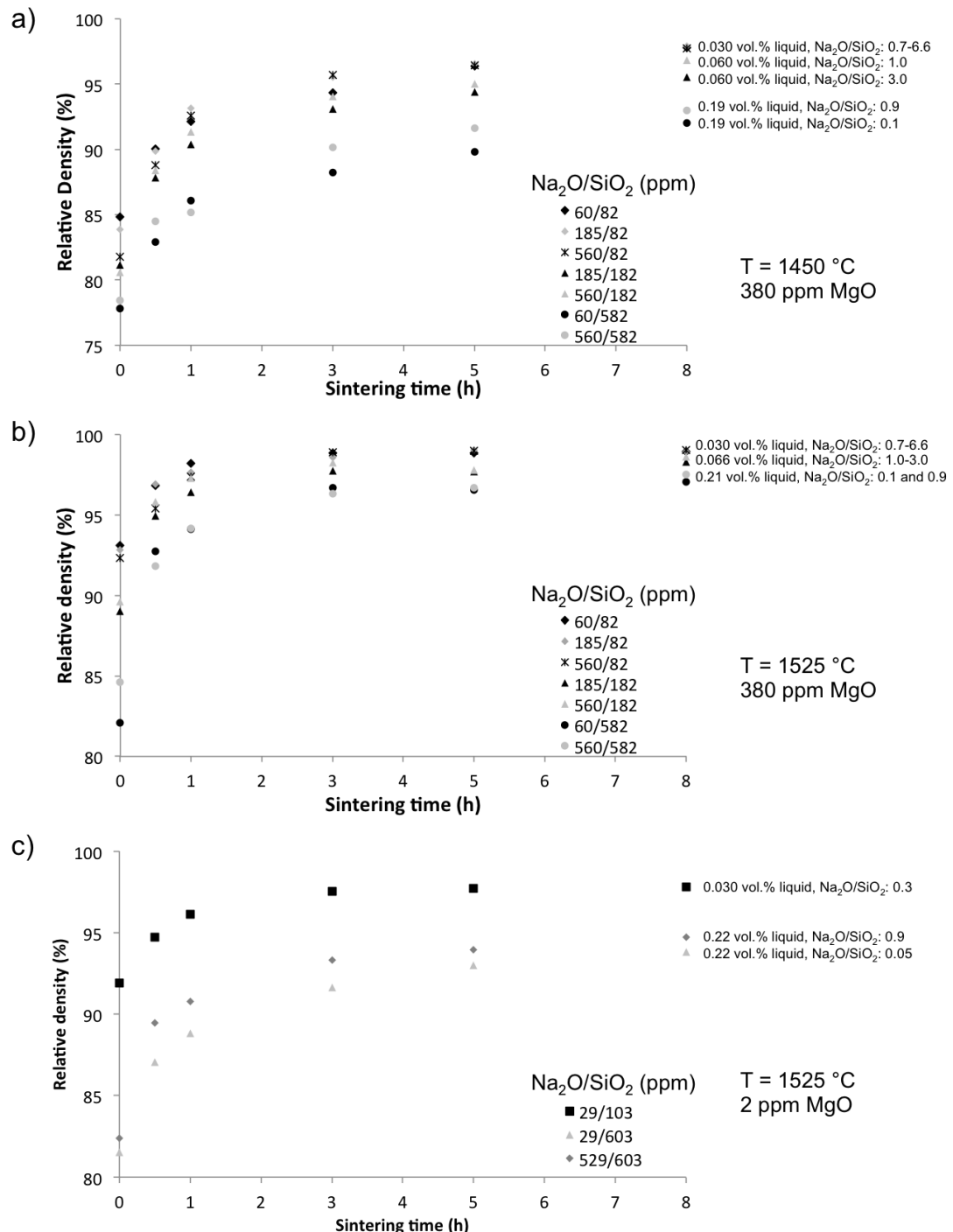


**Figure 3.3.** Densification kinetics of specialty processed alumina containing different amounts  $\text{Na}_2\text{O}$  and  $\text{SiO}_2$  and a) 380 ppm MgO sintered at  $1450^\circ\text{C}$ , b) 380 ppm MgO sintered at  $1525^\circ\text{C}$ , and c) 2 ppm MgO sintered at  $1525^\circ\text{C}$  [2].

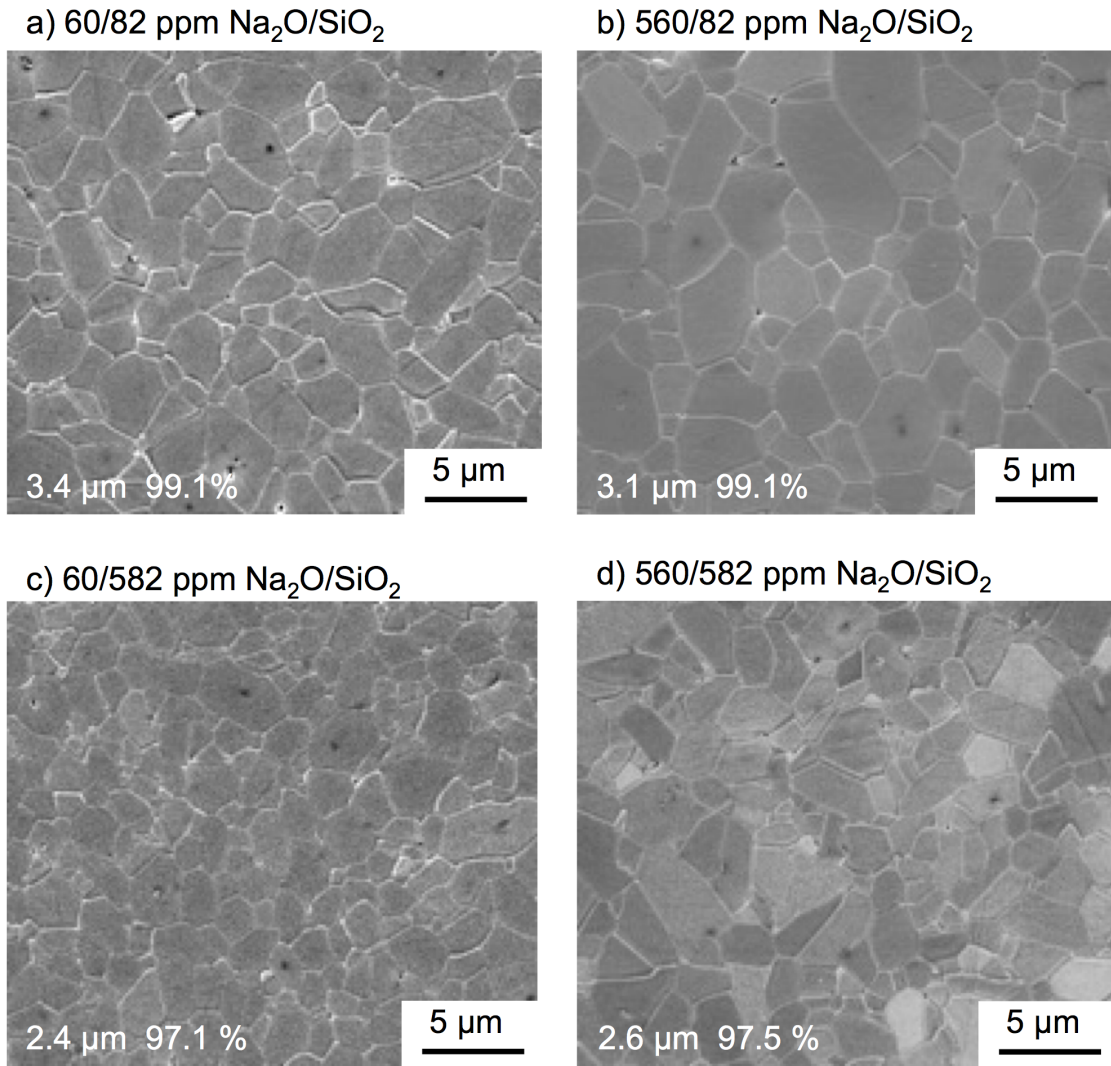


**Figure 3.4.** Microstructures of 380 ppm MgO-doped specialty alumina samples with different  $\text{Na}_2\text{O}$  and  $\text{SiO}_2$  concentrations sintered at 1525°C for 8 h.

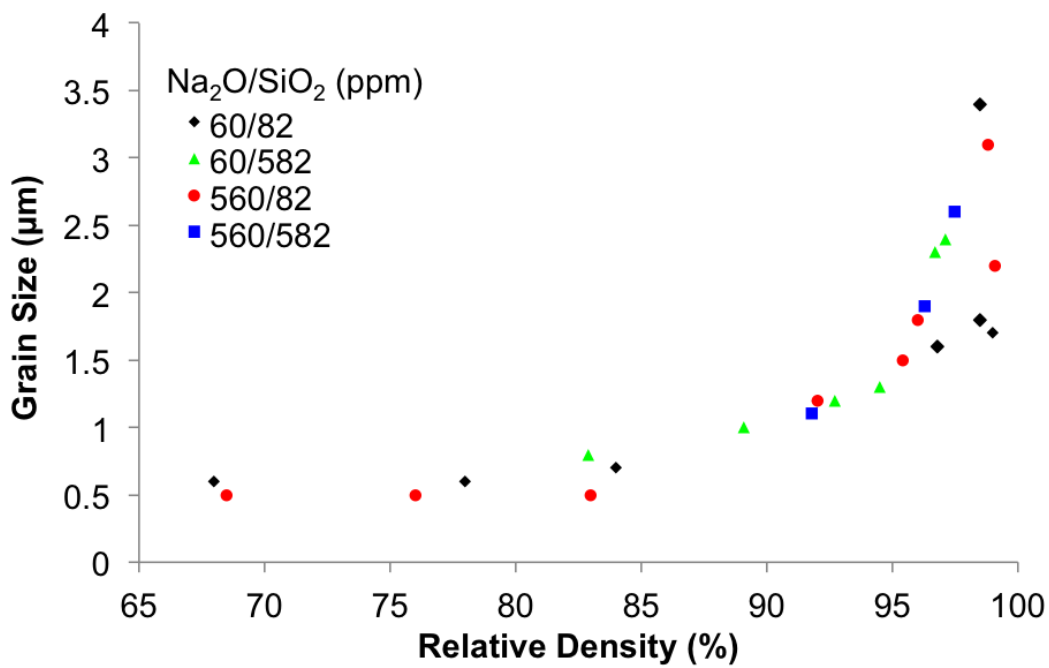


**Figure 3.5.** Sintering trajectories (grain size vs. relative density) for 380 ppm MgO-doped specialty alumina samples with different Na<sub>2</sub>O and SiO<sub>2</sub> concentrations.

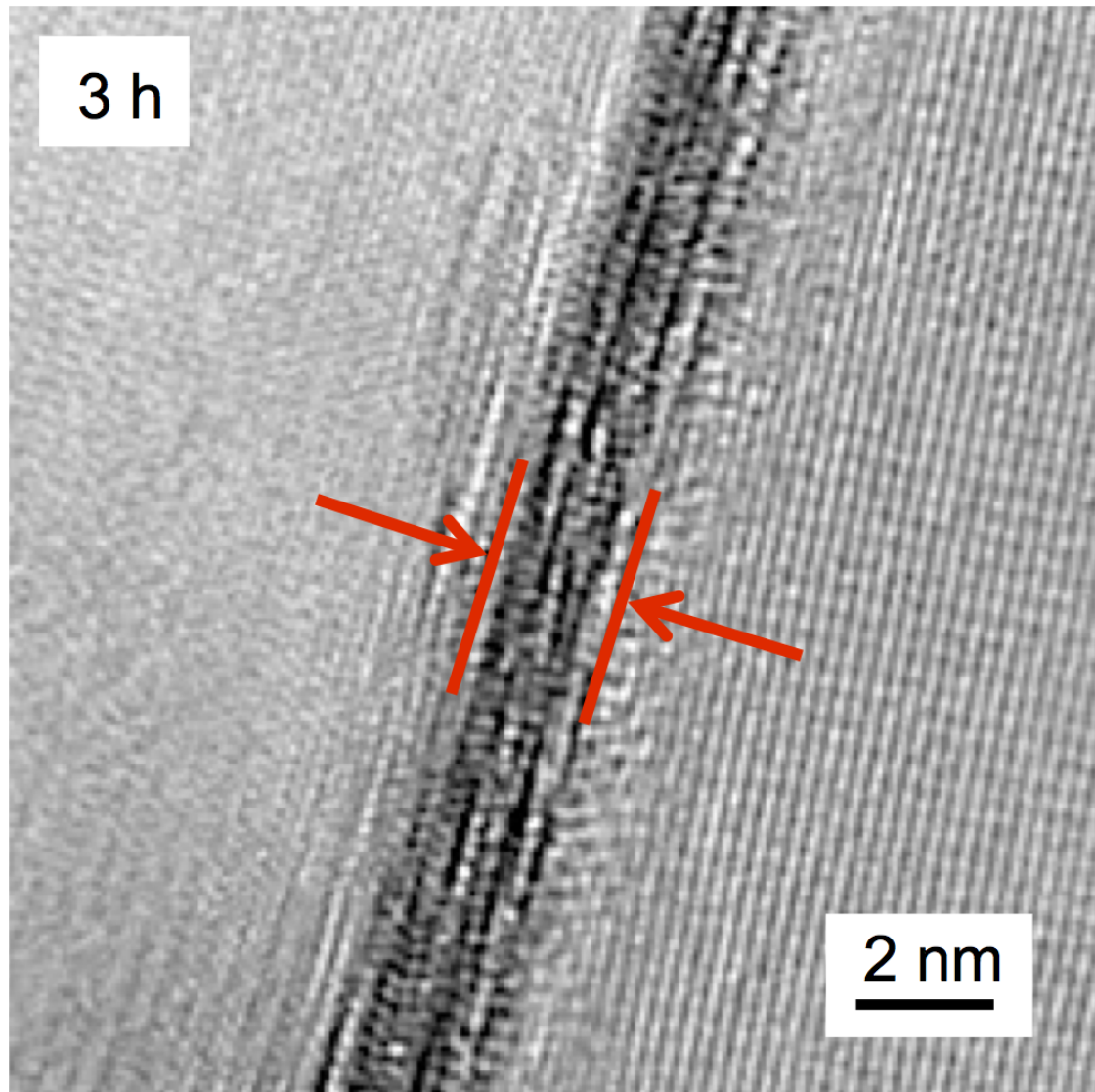


**Figure 3.6.** Grain boundary of a sample containing 529 ppm Na<sub>2</sub>O, 603 ppm SiO<sub>2</sub>, and 2 ppm MgO after 3 h at 1525°C.

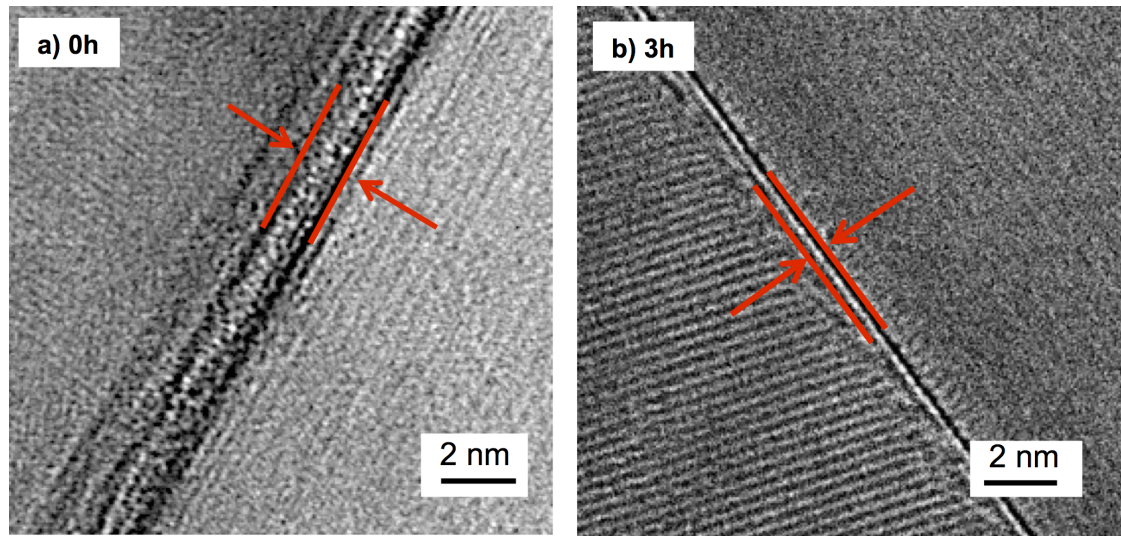


**Figure 3.7.** Grain boundaries of samples containing 560 ppm Na<sub>2</sub>O, 582 ppm SiO<sub>2</sub>, and 380 ppm MgO after a) 0 h and b) 3 h at 1525°C.

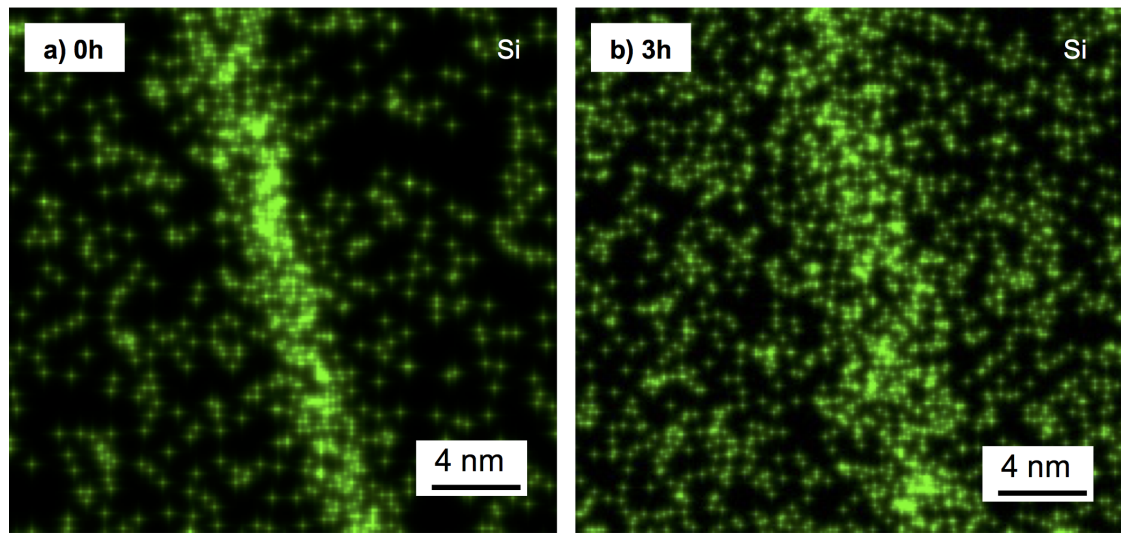


**Figure 3.8.** EDS of grain boundaries of samples containing 560 ppm Na<sub>2</sub>O, 582 ppm SiO<sub>2</sub>, and 380 ppm MgO after a) 0 h and b) 3 h at 1525°C showing the Si distribution. After 0 h Si shows a stronger segregation to the grain boundaries than after 3 h.

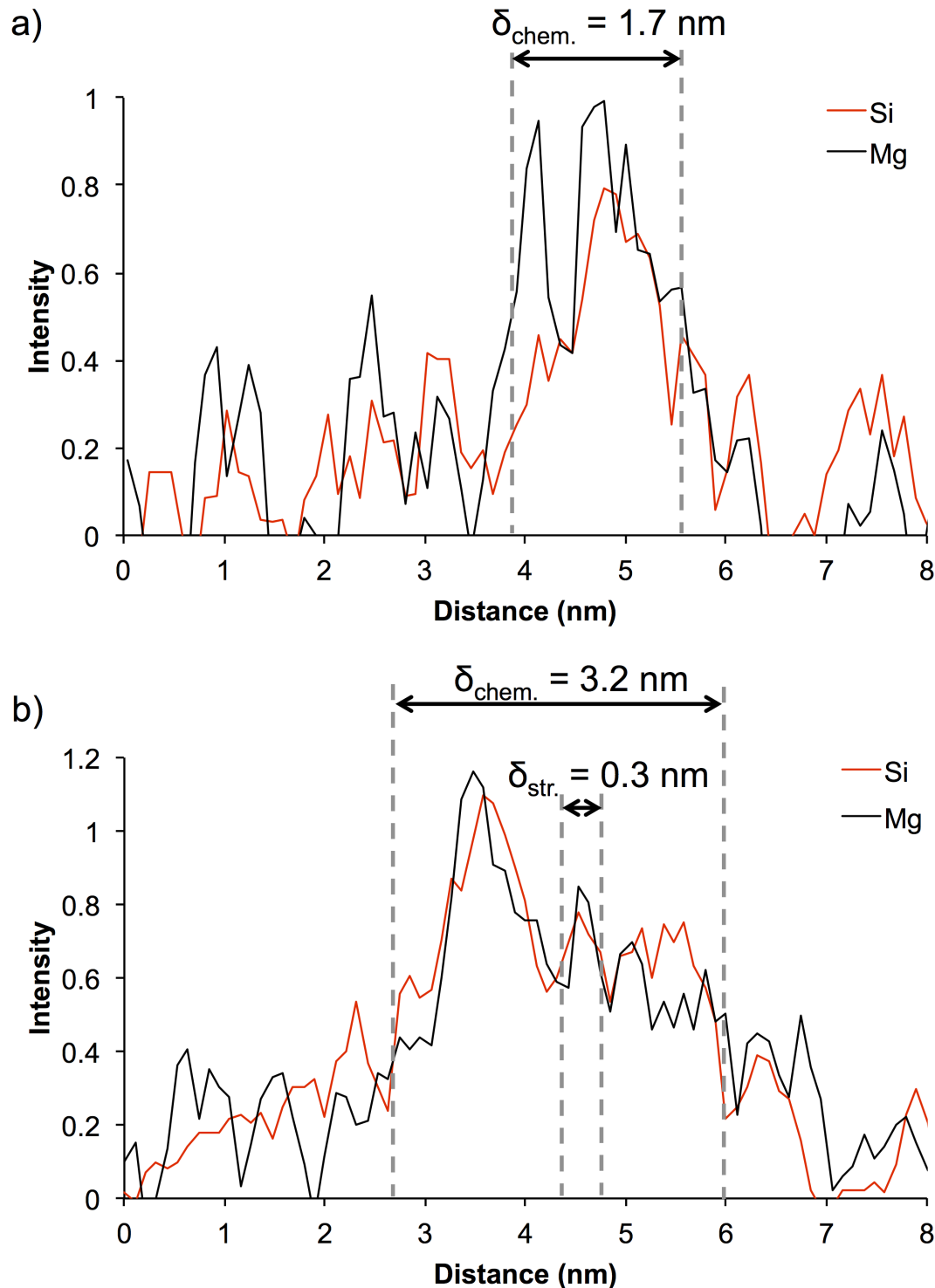


**Figure 3.9.** EDS line scan across a grain boundary of a sample containing 560 ppm Na<sub>2</sub>O, 582 ppm SiO<sub>2</sub>, and 380 ppm MgO after sintering at 1525°C for a) 0 h and b) 3 h.

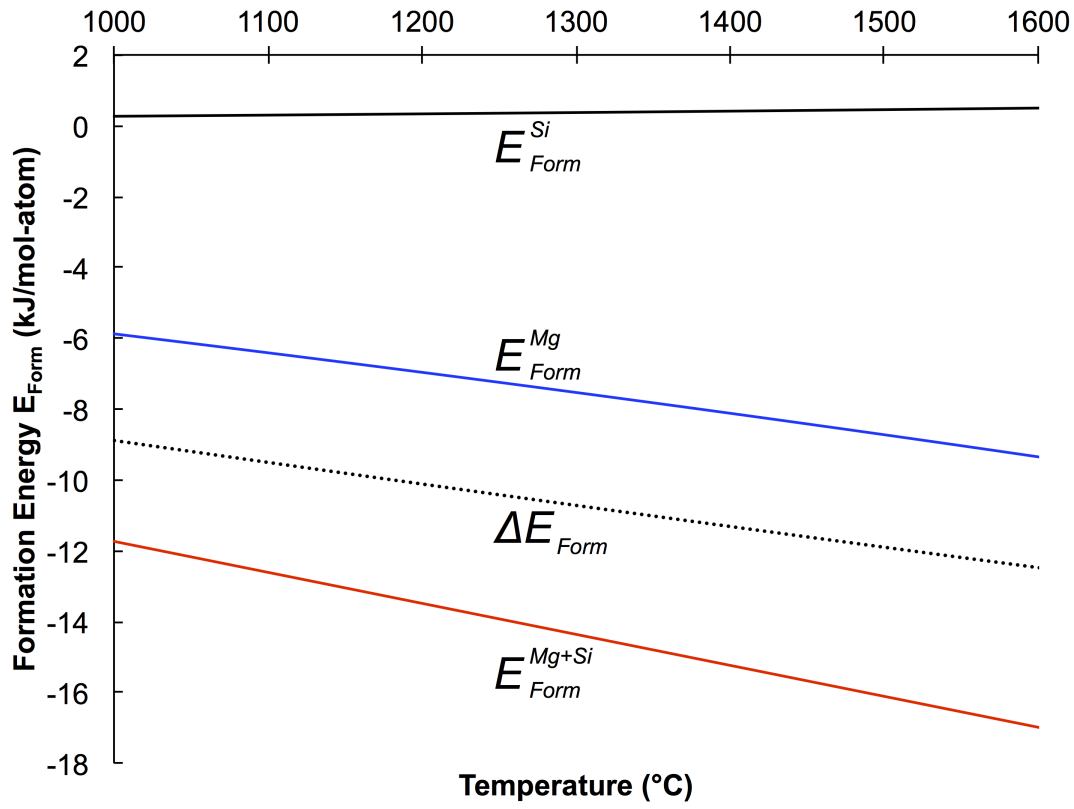


**Figure 3.10.** Comparison of the formation energy of alpha-Al<sub>2</sub>O<sub>3</sub> with an Mg-cluster ( $E_{Form}^{Mg}$ ), Si-cluster ( $E_{Form}^{Si}$ ) and Mg+Si-cluster ( $E_{Form}^{Mg+Si}$ ) as a function of temperature. The formation energy difference ( $\Delta E_{Form}$ ) between the structures was calculated from Eq. REF to compare the formation energy values and show that it is energetically favorable to form Mg+Si-clusters over Si-clusters and Mg-clusters.

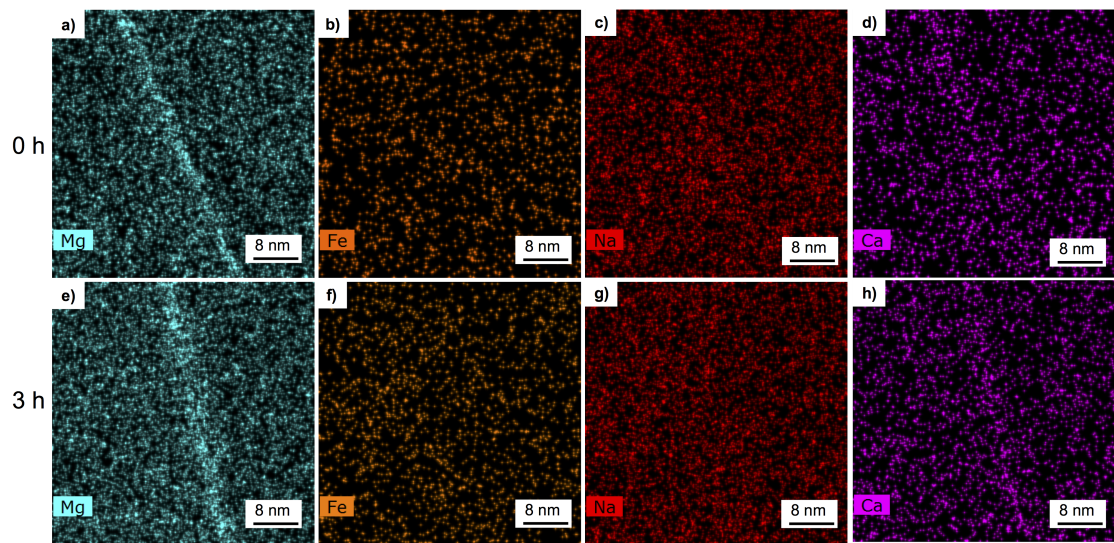


**Figure 3.11.** EDS maps of different oxides in 380 ppm MgO-doped specialty alumina samples after sintering at 1525°C for a-d) 0 h and e-h) 3 h.

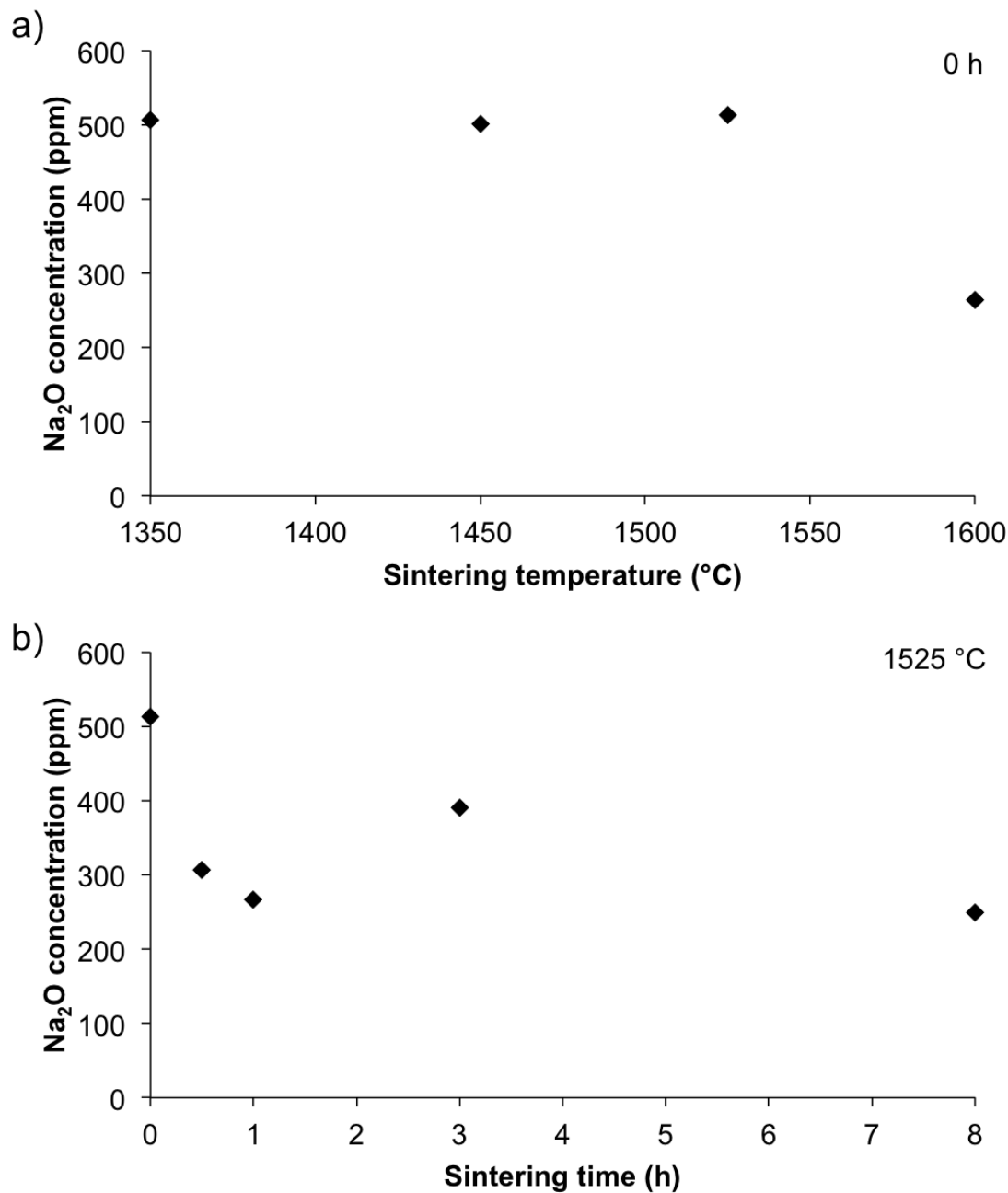


**Figure 3.12.**  $\text{Na}_2\text{O}$  concentration (ICP measurements) of 380 ppm MgO-doped specialty alumina samples with 560 ppm  $\text{Na}_2\text{O}$  as a) function of sintering temperature and b) as a function of sintering time at 1525  $^{\circ}\text{C}$ .

# **Chapter 4**

## **Dynamic development of nanometer scale grain boundaries during liquid phase sintering**

### **4.1 Introduction**

During sintering of ceramics insoluble impurities and dopants can accumulate in the grain boundaries and form an amorphous grain boundary film that significantly influences the sintering behavior and properties of ceramics. Recently, it has been established that grain boundaries in fully dense microstructures can possess different characteristics, depending on chemistry and temperature. Based on their structure and thickness, grain boundaries have been classified into different types of thermodynamically stable complexions [29]. The type of complexion strongly affects transport kinetics and determines the mobility of a grain boundary, and if multiple complexions coexist at a time, multi-modal grain-size distributions and anisotropic microstructures can develop. One class of grain boundaries that is well investigated in dense ceramics are intergranular films (IGF), since they are often observed in a variety of systems such as  $\text{Si}_3\text{N}_4$ ,  $\text{SiC}$ , and  $\text{Al}_2\text{O}_3$  [71, 78]. IGFs are amorphous grain boundary films with an equilibrium thickness of typically 1-2 nm. Clarke et al. showed that the equilibrium film thickness results from a balance of attractive and repulsive interparticle forces, similar to those seen in colloidal systems [78, 79].

In classical sintering theories the differences in grain boundary structures are

considered by distinguishing between solid state and liquid phase sintering with fundamental differences in their respective sintering mechanisms. Solid state sintering occurs by solid state diffusion throughout the entire sintering process. During initial stage sintering surface diffusion leads to the formation of necks between particles. Most of the densification up to  $\sim 92\%$  occurs during intermediate stage, where grain boundaries between particles and pore channels along the grain edges form. At densities  $>92\%$  the pore channels close and isolated pores first form and are then eliminated during final stage sintering. The dominant diffusion mechanisms during intermediate and final stage sintering are volume and grain boundary diffusion, which can be affected by solute segregated to the grain boundaries [29].

In contrast, for liquid phase sintering [80] the particle compact is penetrated by a liquid film and during the initial sintering stage the powder compact begins to densify by particle rearrangement after the liquid phase has formed. Further densification during intermediate and final stage sintering is controlled by a solution-precipitation mechanism, where the particles of the sinter are dispersed in a liquid glass matrix, and material from the grain boundary area dissolves into the liquid grain boundary phase and diffuses to the particle necks, where it precipitates, leading to a particle contact flattening and densification.

Additional models were developed in the literature that account for the liquid phase redistribution during densification. For example, a number of models describe the filling of pores during liquid phase sintering due to capillarity [81, 82]. However, the existing models in the literature that address liquid phase redistribution typically deal with liquid concentrations of at least a few volume percent. In this case it can be assumed that the concentration of liquid phase is high enough to form a continuous liquid film of equilibrium thickness [71, 78, 79] in the grain boundaries and that excess liquid phase accumulates in necks, pores and glass pockets. For example, Svoboda et al. [83] assumed a constant equilibrium intergranular film thickness of 1.5 nm when they developed their liquid phase sintering model, and Kwon and Messing [47] estimated a grain boundary thickness of  $\sim 1$  nm based on a squeeze film analysis.

The redistribution of liquid phase becomes more complicated as the liquid phase concentration in a sinter is reduced, for example to concentrations  $<0.2$  vol.%. In this case the glass phase concentration could be insufficient to form a liquid

film of equilibrium thickness, and if the glass phase concentration is low enough the grain boundaries may be considered rather solid than liquid, which changes the sintering model that can be applied. This case is interesting specifically in commercial powders used in industry, since they typically contain higher impurity levels than the ultra-high purity powders studied in academia. For example, most fundamental research on alumina uses ultra-high purity aluminas of >99.99% Al<sub>2</sub>O<sub>3</sub> and, therefore, sintering is analyzed using solid state sintering models. In contrast commercial alumina powders are typically produced by the Bayer process and are ~99.8% pure with ppm levels of Na<sub>2</sub>O, SiO<sub>2</sub>, CaO, and Fe<sub>2</sub>O<sub>3</sub>, and added MgO as a sintering additive. The concentration and ratios of these impurities and additives can vary substantially by the commercial grade and can form a small amount of liquid phase. Despite considerable interest no research has been done on determining what volume fraction of liquid phase is necessary to consider grain boundaries liquid and when to apply a liquid phase sintering model in such a system.

Concentration, chemistry, and distribution of a liquid phase change during densification as a result of increasing temperature during heating and as a result of changing grain boundary area during densification and grain growth. This implies that grain boundaries undergo a dynamic change in physical and chemical character during densification. This dynamic change in chemistry and structure and possible transitions of grain boundaries from solid to liquid or vice versa can significantly impact densification as densification typically occurs via grain boundary diffusion. While most liquid phase sintering models imply that grain boundaries may change during densification, no work has been done on identifying these changes.

In this work we develop a model to predict the dynamic development of grain boundaries from initial to final stage sintering as a function of chemical and physical parameters of a sintering powder. The predicted grain boundary thicknesses are compared with grain boundaries examined by high-resolution TEM.

## 4.2 Experiment

Two chemically purified Bayer process alumina powders (Almatis, Inc., Leetsdale, PA, USA) were chosen for study. Powder characteristics and experimental details are described in previous chapter [?]. The main difference between the two

powders are the MgO concentrations of 2 ppm (MgO-free powder) and 380 ppm (MgO-doped powder), respectively. The powders were doped with up to 1000 ppm Na<sub>2</sub>O and 1000 ppm SiO<sub>2</sub> using sodium acetate (NaC<sub>2</sub>H<sub>3</sub>O<sub>2</sub>\*3H<sub>2</sub>O, ACS grade, BDH, VWR International LLC, West Chester, PA, USA) and tetraethyl orthosilicate (Si(OC<sub>2</sub>H<sub>5</sub>)<sub>4</sub>, 98%, Aldrich Chemical Company, Inc. Milwaukee, WI, USA), respectively, to obtain chemistries similar to commercial high purity Bayer aluminas at different glass concentrations. Samples with green densities of 59.0 ± 0.5% were fabricated for sintering studies by uniaxial and cold isostatic dry pressing (CIP, Autoclave engineers, Erie, Pa, USA) at 170 MPa and 200 MPa, respectively. The dry pressed cylinders were heated at 10°C/min to 1525°C in a thermomechanical analyzer (TMA, Linseis PT1600, Robbinsville, NJ, USA) to record the shrinkage during heating. Samples were heated at 10°C/min to 1200°C and then at 5°C/min to 1525°C for different hold times. Microstructure and density were measured by the linear intercept (ASTM Standard E112-96) [?] and Archimedes methods (ASTM standard B962-15), [?] respectively. The structure and chemistry of grain boundaries were investigated by transmission electron microscopy (TEM) and energy dispersive x-ray spectroscopy (EDS) using a dual aberration corrected FEI Titan [79] field emission microscope operated at 300 kV and FEI Talos (FEI, Hillsboro, OR, USA) field emission microscope at 200 kV. The EDS on both microscopes is an FEI Super-X system consisting of four SDDs (Silicon Drift Detectors) with a solid angle of 0.9 sr ad. The samples for TEM and EDS were air-quenched from the sintering temperature and prepared using a focused ion beam (Quanta 200 3D Dual Beam FIB, FEI, Hillsboro, OR, USA). Grain boundaries were chosen for analysis that were oriented parallel to the TEM beam in order to accurately measure grain boundary thicknesses in the 2D projection images and EDS profiles.

### 4.3 Grain boundary thickness in MgO-free alumina

The development of the grain boundary thickness during densification is described for MgO-free powder samples with 529/103 ppm Na<sub>2</sub>O/SiO<sub>2</sub>, 529/203 ppm Na<sub>2</sub>O/SiO<sub>2</sub>, and 529/603 ppm Na<sub>2</sub>O/SiO<sub>2</sub>. As shown in the previous chapter, the main difference of the samples is the concentration of glass phase that forms. The liquidus projection of the Al<sub>2</sub>O<sub>3</sub>-Na<sub>2</sub>O-SiO<sub>2</sub> phase diagram [83] was used to predict the equilibrium composition of the glass phase during heating as a function

of temperature [?], and based on the concentration of Na<sub>2</sub>O and SiO<sub>2</sub> the glass phase concentration  $\phi(T)$  was estimated as a function of temperature, as shown in Figure 4.1.

The liquid glass is expected to accumulate in particle contacts due to capillary forces [82], and during densification it is assumed that the liquid phase accumulates in the grain boundaries until an equilibrium film thickness [71] is reached. After this equilibrium thickness is reached it is assumed that the excess liquid phase accumulates in the particle necks. The fraction of a particle/grain surface that is in contact with another particle/grain, i.e. the fraction of grain boundary area, increases with increasing density [84]:

$$\alpha(\rho) = 1 - r(\rho) \left(1 - \frac{\rho}{100}\right)^{\frac{1}{2}} \quad (4.1)$$

where  $r$  is a factor between 1.4 and 1.7, depending on the relative density. With these assumptions the grain boundary thickness based on the amount of impurities in the samples can be estimated by:

$$\delta = 2 \frac{V_g \phi(T)}{S_g (1 - \phi(T)) \alpha(\rho)} \quad (4.2)$$

where  $V_g$  and  $S_g$  are the average volume and average surface area of a particle/grain. The parameters of this equation are specific to the system investigated and change during sintering.

If the calculated grain boundary thickness is smaller than a monolayer, e.g. the size of a SiO<sub>4</sub><sup>4-</sup> tetrahedron ( $\sim 0.3$  nm), the liquid phase concentration in the sample is not high enough to form a liquid grain boundary phase, assuming a homogeneous distribution of the liquid phase in the sample. We assume that a grain boundary thickness  $> 0.6$  nm, i.e. a bilayer of SiO<sub>4</sub><sup>4-</sup> tetrahedra, is necessary to consider the grain boundary liquid or liquid like. For calculated grain boundary thicknesses  $> 0.6$  nm the grain boundary thickness is assumed to be limited by an equilibrium film thickness, if the concentration of the liquid phase is high enough to form an amorphous film of equilibrium thickness. If the concentration of the liquid phase is not high enough to form an amorphous film of equilibrium thickness, the grain boundary thickness is limited by the concentration of glass phase in the sample.

Dilatometry was used to determine the development of relative density as a function of temperature (Figure 4.2), assuming isotropic shrinkage of the samples.

Now the increase in liquid phase concentration can be expressed as a function of relative density, as seen in Figure 4.3.  $V_g$  and  $S_g$  were estimated using the average particle/grain size determined from micrographs, assuming spherical particles of the same size, and using the sintering trajectories shown in Figure 4.4,  $V_g$  and  $S_g$  can be expressed as a function of relative density. The grain boundary thickness can be calculated as a function of relative density since all parameters in Eq. 4.2 can be expressed as a function of the relative density.

## 4.4 The equilibrium film thickness model

In 1987 Clarke proposed a model to calculate the equilibrium grain boundary thickness based on the equilibrium between attractive van der Waals and capillary pressures ( $P_{vdW}$  and  $P_C$ ) and repulsive electric double layer and structural disjoining pressures ( $P_{ELD}$  and  $P_{ST}$ ) [78, 79]:

$$P_{vdW} + P_C = P_{ELD} + P_{ST} \quad (4.3)$$

The van der Waals pressure is given by

$$P_{vdW} = \frac{H}{6\pi h^3} \quad (4.4)$$

where  $h$  is the grain boundary thickness and  $H$  is the Hamaker constant, which can be estimated by:

$$H = \frac{3}{4}kT \left( \frac{\varepsilon_\alpha - \varepsilon_\beta}{\varepsilon_\alpha + \varepsilon_\beta} \right)^2 + \frac{3\pi\hbar v}{8\sqrt{2}} \frac{(n_\alpha^2 - n_\beta^2)^2}{(n_\alpha^2 + n_\beta^2)^{\frac{3}{2}}} \quad (4.5)$$

where  $k$  is the Boltzmann constant,  $T$  is the absolute temperature,  $\varepsilon_\alpha$  and  $\varepsilon_\beta$  are the dielectric constants of the ceramic and the glass phase, respectively, and  $n_\alpha$  and  $n_\beta$  are the refractive indices of the ceramic and the glass phase, respectively.

In Clarke's original work the capillary pressure was assumed to be constant, which is a valid assumption for samples at constant densities. However, during densification the capillary pressure changes and can be estimated by [47]:

$$P_C = \frac{\left(0.59 - 0.79(1-\rho)^{\frac{1}{2}}\right)\rho^{\frac{1}{3}}}{0.39(1-\rho)^{\frac{1}{2}}\left(0.59 - 0.39(1-\rho)^{\frac{1}{2}}\right)} \frac{\gamma_{lv}}{r_s} \quad (4.6)$$

where  $\gamma_{lv}$  is the surface tension of the liquid,  $r_s$  is the particle radius, and  $\rho$  is the relative sintered density.

The structural disjoining force is given by [79]:

$$P_{ST} = -\alpha\tau_0^2 \left(\sinh^2\left(\frac{h}{2\xi}\right)\right)^{-1} \quad (4.7)$$

where  $a$  is a constant that can be approximated by the heat of fusion,  $\tau_0$  is a coefficient for the degree of ordering between 0 and 1, and  $\xi$  is a structural correlation length. The electric double layer force is given by [78]

$$P_{ELD} = \frac{16kT}{z^2\pi b_L h^2} \left(\tanh\frac{ze\psi_s}{4kT}\right)^2 (\kappa h)^2 e^{(-\kappa h)} \quad (4.8)$$

where  $z$  is the ion charge and  $e$  is the proton charge. The Bjerrum length  $b_L$  and the inverse of the Debye length  $\kappa$  are given by [78]

$$b_L = \frac{e^2}{4\pi\varepsilon_\beta\varepsilon_0 kT} \quad (4.9)$$

and [85]

$$\kappa = \sqrt{\frac{2N_A I e^2}{\varepsilon_\beta \varepsilon_0 kT}} \quad (4.10)$$

where  $N_A$  and  $I$  are the Avogadro's number and the ionic strength of the liquid, respectively.

## 4.5 Calculation of the theoretical Equilibrium Film Thicknesses

To calculate the equilibrium film thickness for alumina samples, the contributions  $P_{vdW}$ ,  $P_C$ ,  $P_{ELD}$ , and  $P_{ST}$  were calculated using parameters from the literature. The van der Waals pressure was estimated using Eq. 4.3 and 4.4 for a liquid sodium aluminosilicate glass film ( $\varepsilon_\beta = 10$  [86],  $n_\beta = 1.51$  [49]) located between

two flat alumina surfaces ( $\varepsilon_\alpha = 11.6$ ,  $n_\alpha = 1.752$ ) [79]. The capillary pressure was calculated as a function of the relative density and grain size from the sintering trajectories shown in Figure 4.2, using Eq. 4.6, assuming a surface tension of the sodium aluminosilicate glass of  $\gamma_{glass} = 387 \text{ N/m}$  [87]. The structural disjoining pressure was calculated using the heat of fusion of carnegieite ( $35.8 \text{ J/cm}^3$ ) for the constant  $a$ , and a structural correlation length of  $0.3 \text{ nm}$  (approximate size of a  $\text{SiO}_4^{4-}$  tetrahedron). The heat of fusion of carnegieite was chosen since its chemical composition is close to the chemical composition of the grain boundary phase investigated here. It is reported in the literature that considerable ordering of intergranular films can extend up to  $1.5 \text{ nm}$  into the intergranular film before they can be assumed completely amorphous [88]. Therefore, a high ordering factor of 0.75 was assumed.

The electric double layer pressure was calculated as a function of film thickness  $h$  using Eq. 4.8-4.10, with  $z = 1$  ( $\text{Na}^+$  ion charge) and  $\varepsilon_\beta = 10$ . The electrostatic potential  $\psi_s$  and ionic strength  $I$  are difficult to estimate, since they are not reported in the literature for the present system. Literature reports estimating equilibrium film thicknesses based on Clarke's model assume values for  $\psi_s$  within a reasonable range of up to  $1.5 \text{ V}$  [78, 89]. In this work we attempt to estimate  $\psi_s$  and  $I$  based on the composition and structure of sodium aluminosilicate glass. It is reported in the literature [90] that all  $\text{Al}^{3+}$  ions in sodium aluminosilicate glasses are in tetrahedral coordination if  $\text{Na}/\text{Al} \geq 1$ , and the local charge deficit of an  $\text{AlO}_4^{5-}$  tetrahedron (compared to the  $\text{SiO}_4^{4-}$  tetrahedron) is compensated by an associated  $\text{Na}^+$ . Excess  $\text{Na}^+$  ions that are not required for this charge compensation act as network modifiers in the glass. For  $\text{Na}/\text{Al} < 1$ , there are not enough  $\text{Na}^+$  ions to stabilize all  $\text{Al}^{3+}$  ions in tetrahedral coordination, and excess  $\text{Al}^{3+}$  ions can form triclusters or are in octahedral coordination [90].

In this model we assume for  $\text{Na}/\text{Al} > 1$  in the glass that  $\text{Na}^+$  ions compensating the charge of an  $\text{AlO}_4^{5-}$  tetrahedron are not mobile due to electrostatic attraction between the charged  $\text{AlO}_4^{5+}$  tetrahedron and the  $\text{Na}^+$  ion, whereas excess  $\text{Na}^+$  ions are assumed to be available as charge carriers. For the samples investigated here an  $I$  of  $2.25 \text{ mol/l}$  was calculated. If we assume that a fraction  $f_{cc}$  of the charge carriers segregate to the immediate particle/grain surface, a charge carrier density  $\sigma$  can be calculated by

$$\sigma = \frac{(c_{Na} - c_{Al}) f_{cc} V_{glass} N_A}{V_m \pi d^2} \quad (4.11)$$

where  $c_{Na}$  and  $c_{Al}$  are the concentration of  $\text{Na}^+$  and  $\text{Al}^{3+}$  ions in the glass, respectively,  $V_{glass}$  is the volume of glass around one particle/grain,  $V_m$  is the molar volume of the glass, and  $d$  is the particle/grain diameter. The electrostatic potential can then be calculated by [78]:

$$\psi_s = \sinh^{-1} \left( \frac{\sigma 2\pi z e b_L}{\kappa} \right) \frac{2kT}{ze} \quad (4.12)$$

The composition of the glass phase in the samples estimated from the phase diagram changes during heating, and consequently the Na/Al ratio changes as shown in Figure 4.5.  $\psi_s$  changes during heating because of the changing charge carrier concentration, the increasing grain boundary area, and the increasing grain size during densification. Figure 4.6 shows the change in  $\psi_s$  during heating, assuming a glass density of 2.45 g/cm<sup>3</sup> and 75% of the charge carriers segregate to the particle/grain surface ( $f_{cc} = 0.75$ ). The estimated values for  $\psi_s$  are reasonable when compared to  $\psi_s$  values used in the literature [78].

Figure 4.7 shows the individual contributions to the equilibrium film thickness plotted as a function of film thickness for a sample with 529 ppm  $\text{Na}_2\text{O}$  and 603 ppm  $\text{SiO}_2$  at 1525°C and a relative density of 93%. It can be seen that the net pressure, i.e. the sum of the acting pressures, is 0 MPa for a film thickness of 1.7 nm, which corresponds to the equilibrium film thickness. From the above discussion it is apparent that  $P_{vdW}$ ,  $P_{CP}$ , and  $P_{ELD}$  change during densification. The film thickness at which the net pressure is 0 MPa (i.e., the equilibrium film thickness) was calculated for samples at different relative densities during the sintering process, and the calculated equilibrium film thicknesses are shown in Figure 4.8. It should be noted that  $P_{vdW}$  and  $P_C$  are a function of temperature, since the parameters they are calculated from are functions of temperature, glass composition, refractive indices, dielectric constants, and surface tension. However, investigations showed that the changes in  $P_{vdW}$  and  $P_C$  due to the changing temperature are insignificant, and therefore, these contributions were assumed to be constant. Figure 4.8 shows that the equilibrium film thickness does not depend on the amount of glass phase, but decreases as a function of relative density from 2.2 nm at ~60% relative density to 1.6 nm at 98% relative density, as seen in Figure 4.7.

It is interesting to note that for film thicknesses  $> 1$  nm  $P_C$  and  $P_{ST}$  control the equilibrium thickness, and the contributions from  $P_{vdW}$  and  $P_{ELD}$  are negligible. At film thicknesses  $> 1$  nm  $P_{ST}$  is not expected to change as a function of density, and, therefore, the equilibrium thickness during densification is governed by the change in  $P_C$ . For film thicknesses  $< 1$  nm  $P_{ELD}$ ,  $P_{ST}$ , and  $P_{vdW}$  significantly contribute to the force balance and  $P_C$  is negligible.

Figure 4.9 shows plots of the development of the grain boundary thickness as a function of relative density for different glass concentrations. The trajectory of the equilibrium film thickness (see also Figure 4.8) represents the grain boundary thickness if enough glass phase is present to form a film with equilibrium thickness. The three trajectories labeled with 529/103 ppm Na<sub>2</sub>O/SiO<sub>2</sub>, 529/203 ppm Na<sub>2</sub>O/SiO<sub>2</sub>, and 529/603 ppm Na<sub>2</sub>O/SiO<sub>2</sub> are the estimated grain boundary thicknesses based on the amount of glass phase that is present in the samples. For all glass concentrations, the grain boundary thickness first decreases during initial and intermediate stage sintering. This decrease in grain boundary thickness is due to the increase in grain boundary area with increasing relative density, since the liquid glass phase is distributed over a larger grain boundary area. At the end of the intermediate sintering stage and during final stage sintering grain growth begins, which results in a reduction of the grain boundary area and, therefore, an increase in grain boundary thickness.

For samples with 529/103 ppm Na<sub>2</sub>O/SiO<sub>2</sub> and 529/203 ppm Na<sub>2</sub>O/SiO<sub>2</sub> the grain boundary thicknesses determined from the amount of glass phase are less than the equilibrium film thickness, and therefore, the grain boundary thickness is limited by the amount of glass phase in the sample. For samples with 529/603 ppm Na<sub>2</sub>O/SiO<sub>2</sub> the glass phase concentration in the sample is close to the glass phase concentration necessary to form a film of equilibrium thickness, and the grain boundary thickness is limited by the amount of glass phase or the equilibrium film thickness, depending on the relative density. For samples with higher glass concentrations, the grain boundary thickness is determined by the equilibrium film thickness.

## 4.6 High-resolution TEM

The predicted grain boundary thicknesses were compared to grain boundary thicknesses measured from high-resolution TEM images of samples with different glass concentrations. Figure 4.10 shows high resolution TEM images of the grain boundaries of samples with 0.066 vol.% (529/203 ppm Na<sub>2</sub>O/SiO<sub>2</sub>), 0.21 vol.% (529/603 ppm Na<sub>2</sub>O/SiO<sub>2</sub>), and 0.36 vol.% glass phase (1000/1000 ppm Na<sub>2</sub>O/SiO<sub>2</sub>) after 3 h at 1525°C. The thicknesses of the amorphous grain boundary as measured from the TEM images are 1.0 nm, 1.7 nm and 1.9 nm, respectively.

As seen in Figure 4.9 the measured grain boundary thicknesses agree well with the predicted grain boundary thicknesses. For a sample of 96% relative density and 0.073 vol.% glass phase the predicted grain boundary thickness is 0.9 nm, and the measured grain boundary thickness is 1.0 nm (Figure 4.10a). The equilibrium grain boundary thickness for this sample is 1.6 nm, however, the glass phase concentration is only high enough to form a 1.0 nm thick film. For the sample with 0.21 vol.% (529/603 ppm Na<sub>2</sub>O/SiO<sub>2</sub>) and a relative density of 93% the measured grain boundary thickness of 1.7 nm agrees well with the estimated equilibrium film thickness of 1.7 nm. The glass phase concentration in this sample is high enough to form a film with a thickness of ~2.2 nm, however, the grain boundary thickness is limited by the equilibrium film thickness. For samples with even higher glass concentrations of 0.36 vol.% the glass phase concentration is high enough to form a grain boundary thickness > 3.5 nm, however, the grain boundary thickness determined by TEM is 1.9 nm, which is close to the value of the equilibrium film thickness of 1.7 nm.

Figure 4.9d shows a sample with 0.03 vol.% glass phase (29/103 ppm Na<sub>2</sub>O/SiO<sub>2</sub>). There is no amorphous film in the grain boundaries because for samples with low SiO<sub>2</sub> concentrations such as 103 ppm the theoretically predicted grain boundary is less than a monolayer, and the amount of SiO<sub>2</sub> is insufficient to form a continuous amorphous film in the grain boundaries. However, EDS analysis shows that there is still SiO<sub>2</sub> segregated to the grain boundaries. Note that the maximum sintering temperature of the samples in this work is 1525°C. At higher sintering temperatures a higher glass phase concentration is expected, and, therefore, thicker grain boundaries would be observed.

## 4.7 The effect of changes in powder chemistry

### 4.7.1 Na<sub>2</sub>O/SiO<sub>2</sub> ratio

For the results above a Na<sub>2</sub>O/SiO<sub>2</sub> ratio  $\geq 0.5$  in the sample was assumed, which results in a Na<sub>2</sub>O/SiO<sub>2</sub> ratio of 0.5 in the glass phase. For Na<sub>2</sub>O/SiO<sub>2</sub> ratios  $< 0.5$  the composition of the glass phase is expected to change, and consequently the grain boundary thickness is expected to change as a function of chemistry.

Figure 4.11 shows a high resolution TEM image of a grain boundary of a sample containing 0.17 vol.% glass phase (29/603 ppm Na<sub>2</sub>O/SiO<sub>2</sub>) and a molar Na<sub>2</sub>O/SiO<sub>2</sub> ratio of 0.1 after 3 h at 1525°C, and the measured grain boundary is  $\sim 1.0$  nm thick. Based on the amount of impurities a grain boundary thickness of 2.2 nm is expected in those samples, which indicates that for this chemical composition an equilibrium grain boundary thickness [71] is reached at  $\sim 1.0$  nm. Investigations on how the capillary pressure and van der Waals pressure change as a result of the changed glass chemistry show that the differences in the resulting pressures are negligible. Therefore, the reduction can be attributed to a reduction in the repulsive  $P_{ST}$  and  $P_{ELD}$ .

The Na/Al ratio in the glass phase of the sample with 29/603 ppm Na<sub>2</sub>O/SiO<sub>2</sub> is  $< 1$ , and all Na<sup>+</sup> ions are assumed to stabilize Al<sup>3+</sup> ions in tetrahedral coordination. Therefore, no Na<sup>+</sup> ions are available as charge carriers, and  $P_{ELD}$  is assumed to be zero. If  $P_{ELD}$  is assumed to be zero and  $P_{ST}$  is the same as for higher Na<sub>2</sub>O/SiO<sub>2</sub> ratios, the change in equilibrium film thickness is  $< 0.1$  nm. This confirms the earlier conclusion that  $P_{ST}$  is the dominant repulsive pressure at film thicknesses  $\geq 1$  nm, and that  $P_{ELD}$  is insignificant for the equilibrium grain boundary thicknesses investigated here. This means  $P_{ST}$  has to decrease as the Na<sub>2</sub>O/SiO<sub>2</sub> ratio in the sample decreases. Computer simulations showed that the ordering of sodium silicate glass between two alumina surfaces increases with increasing Na<sub>2</sub>O/SiO<sub>2</sub> ratio [91]. Therefore, it is reasonable to assume a lower ordering parameter  $\tau_0$  for the sample with a molar Na<sub>2</sub>O/SiO<sub>2</sub> ratio of 0.1. For example, if an ordering parameter of 0.25 is assumed the calculated equilibrium film thickness is  $\sim 1.0$  nm for samples with a relative density of 93%, which is close to the observed grain boundary thickness seen in Figure 4.11.

### 4.7.2 MgO-doped Bayer alumina

The influence of MgO on the sintering of Bayer alumina was reported in previous work, and it was shown that MgO increases the solubility of SiO<sub>2</sub> in the alumina lattice. Therefore, the reduction of SiO<sub>2</sub> on the grain boundaries by this process has to be taken into account when the grain boundary thickness is calculated. Figure 4.12 shows high resolution TEM images of grain boundaries of the MgO-doped powder with a) 60/82 ppm Na<sub>2</sub>O/SiO<sub>2</sub>, b) 60/582 ppm Na<sub>2</sub>O/SiO<sub>2</sub>, and c) 560/582 ppm Na<sub>2</sub>O/SiO<sub>2</sub> after 3 h at 1525°C and the amorphous film thicknesses are 0 nm, 0.6 nm, and 0.8 nm, respectively. For the sample containing 60 ppm Na<sub>2</sub>O and 82 ppm SiO<sub>2</sub> no amorphous film is expected because the amount of liquid phase in this sample is not sufficient to form a monolayer, similar to the MgO-free powder samples with 103 ppm SiO<sub>2</sub> seen in Figure 4.9d.

For the samples with 60/582 ppm Na<sub>2</sub>O/SiO<sub>2</sub> and 560/582 ppm Na<sub>2</sub>O/SiO<sub>2</sub> the grain boundaries are substantially thinner than the theoretical calculation of ~2.2 nm. As reported in previous work, we believe that this is due to a co-dissolution process of Mg<sup>2+</sup> and Si<sup>4+</sup> into the alumina lattice, which reduces the amount of liquid phase in the grain boundaries. Assuming that equivalent amounts of SiO<sub>2</sub> and MgO go into solid solution a maximum of 380 ppm MgO and 380 ppm SiO<sub>2</sub> could dissolve into the alumina lattice, which leaves 202 ppm SiO<sub>2</sub> in the grain boundaries that can form a liquid phase. With 202 ppm SiO<sub>2</sub> in the grain boundaries an amorphous film with a thickness of ~0.8 nm is calculated, which agrees well with the observed grain boundary thicknesses of 0.6 and 0.8 nm for the samples containing 560/582 ppm Na<sub>2</sub>O/SiO<sub>2</sub> and 60/582 ppm Na<sub>2</sub>O/SiO<sub>2</sub>, respectively.

## 4.8 Conclusion

A model that describes the dynamic change in grain boundary chemistry and thickness during densification of Bayer alumina was developed. SiO<sub>2</sub> and Na<sub>2</sub>O impurities form a glass phase during heating, which accumulates in particle contacts due to capillarity. The chemistry and concentration of this glass phase changes as a function of temperature. During sintering the grain boundary area changes as a result of densification and grain growth, which affects the glass phase distribution

and, therefore, leads to the observed dynamic change in grain boundary thickness as a function of relative density.

An intergranular film of equilibrium thickness can form between particles/grains if the glass phase concentration is sufficient, and an interparticle force balance governs the grain boundary thickness. We demonstrated that for grain boundary thicknesses  $\geq 1.0$  nm the contributions that control the equilibrium intergranular film thickness are the attractive capillary pressure and the repulsive structural disjoining pressure. If the glass phase concentration in the sample is insufficient to form an intergranular film of equilibrium thickness the grain boundary thickness is determined by the glass phase concentration in the sample. Changes in powder chemistry such as changing the  $\text{Na}_2\text{O}/\text{SiO}_2$  ratio or the  $\text{MgO}$  concentration affect the concentration of glass phase in the sample and the interparticle force balance, which leads to a change in grain boundary thickness. Grain boundary thicknesses measured from high-resolution TEM images agree well with predicted values.

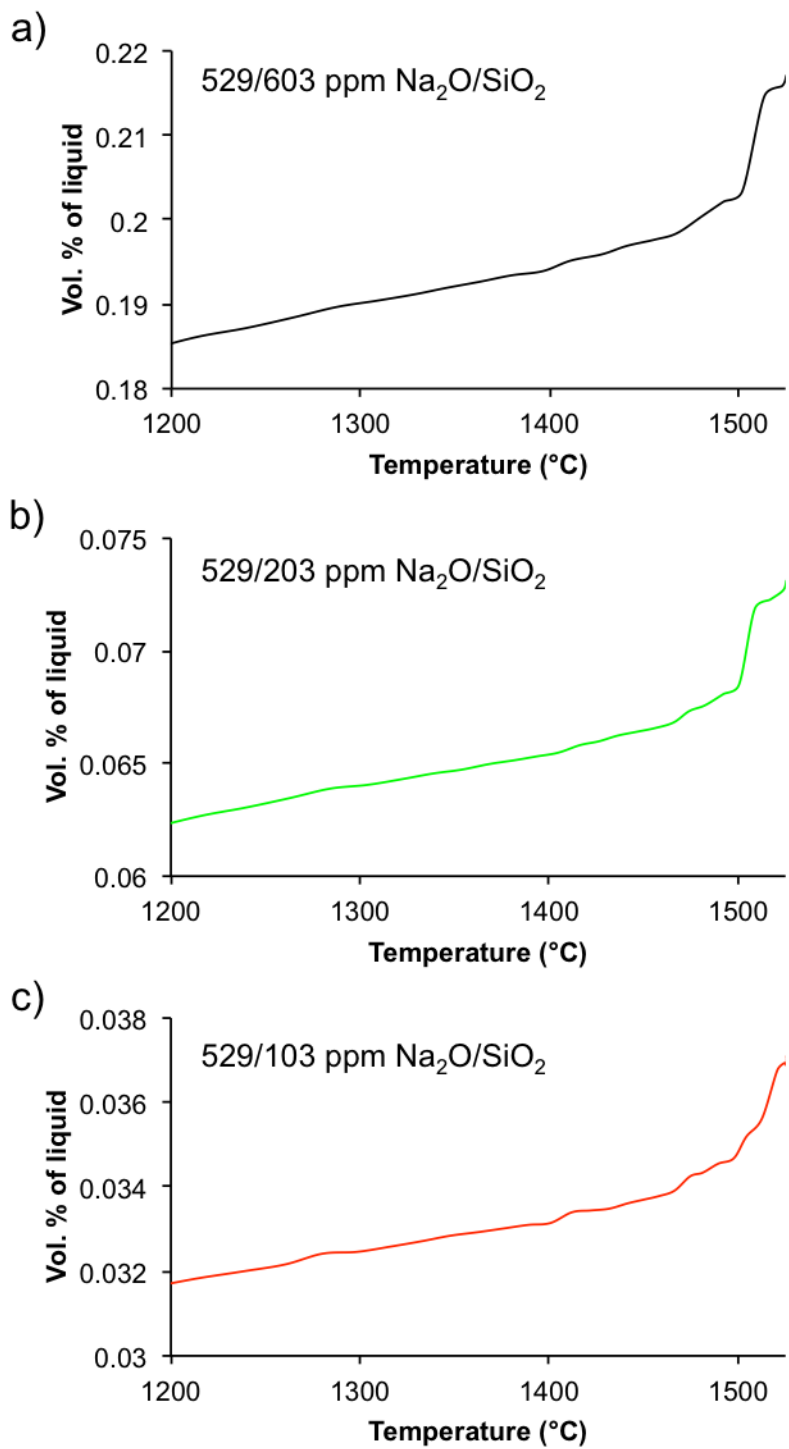


**Figure 4.1.** Increase in concentration of liquid phase as a function of temperature for MgO-free powder samples with 529 ppm  $\text{Na}_2\text{O}$  and different  $\text{SiO}_2$  concentrations.

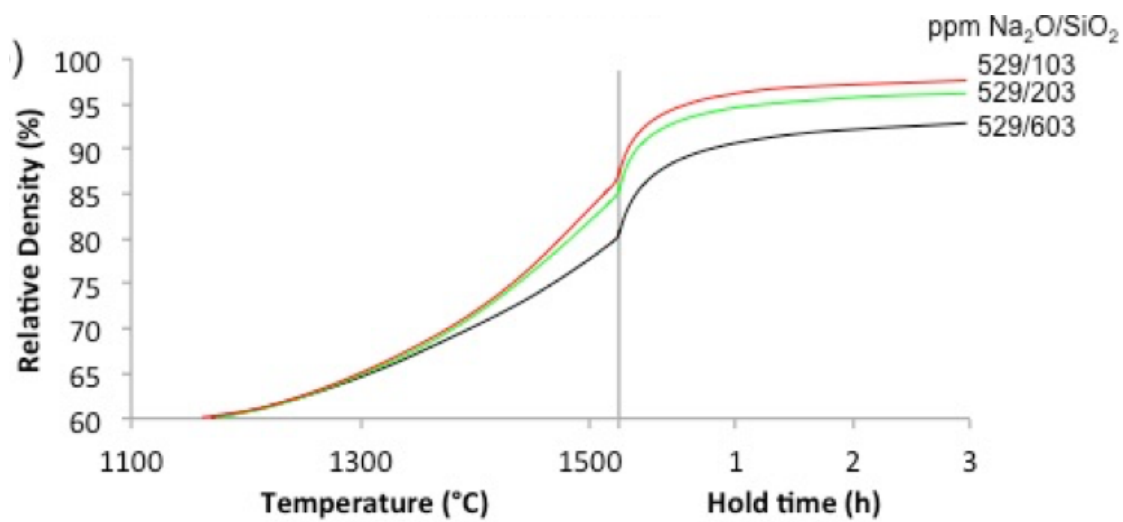


**Figure 4.2.** Relative density as a function of temperature and hold time determined from dilatometry for MgO-free powder samples with 529 ppm Na<sub>2</sub>O and different SiO<sub>2</sub> concentrations.

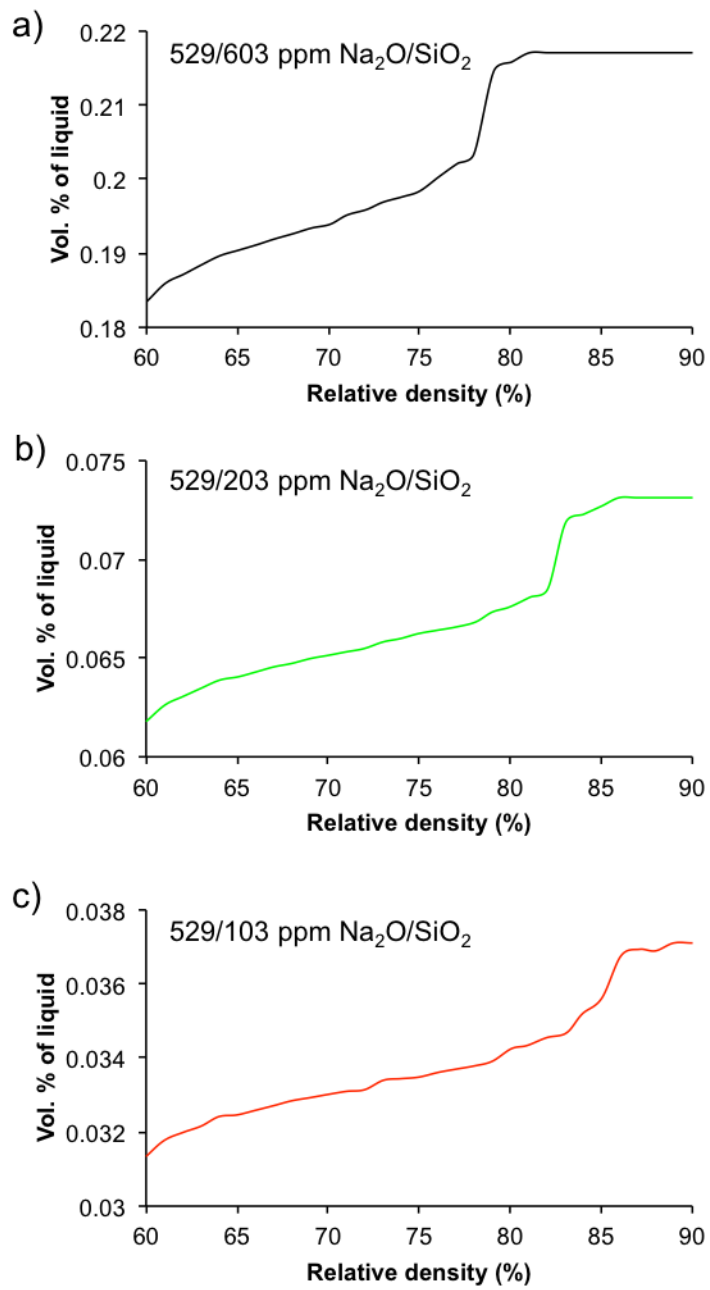


**Figure 4.3.** Liquid phase concentration as a function of relative density for MgO-free powder samples with 529 ppm Na<sub>2</sub>O and different SiO<sub>2</sub> concentrations.

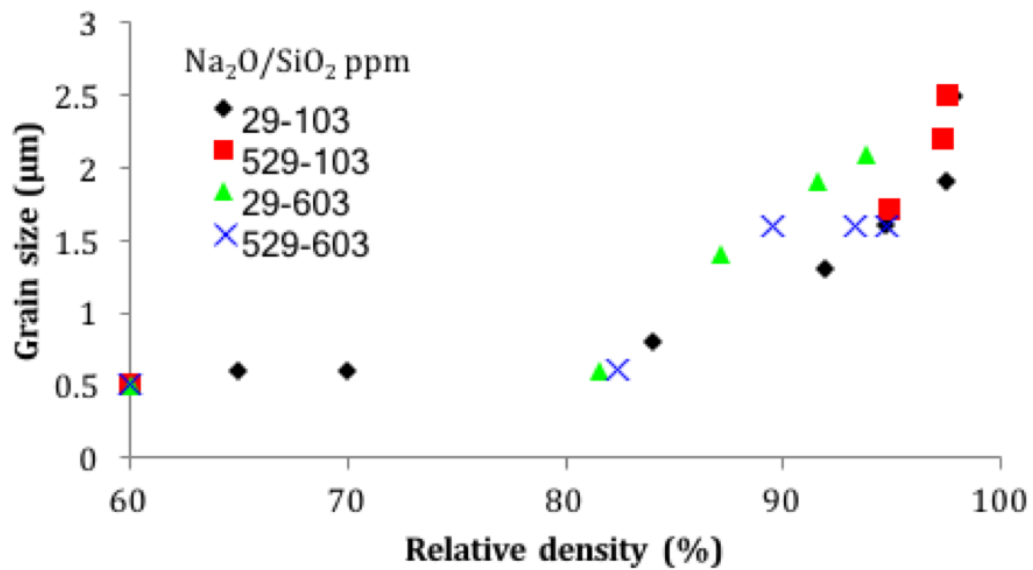


**Figure 4.4.** Grain size - density trajectories as a function of  $\text{Na}_2\text{O}$  and  $\text{SiO}_2$  concentration for MgO-free alumina.

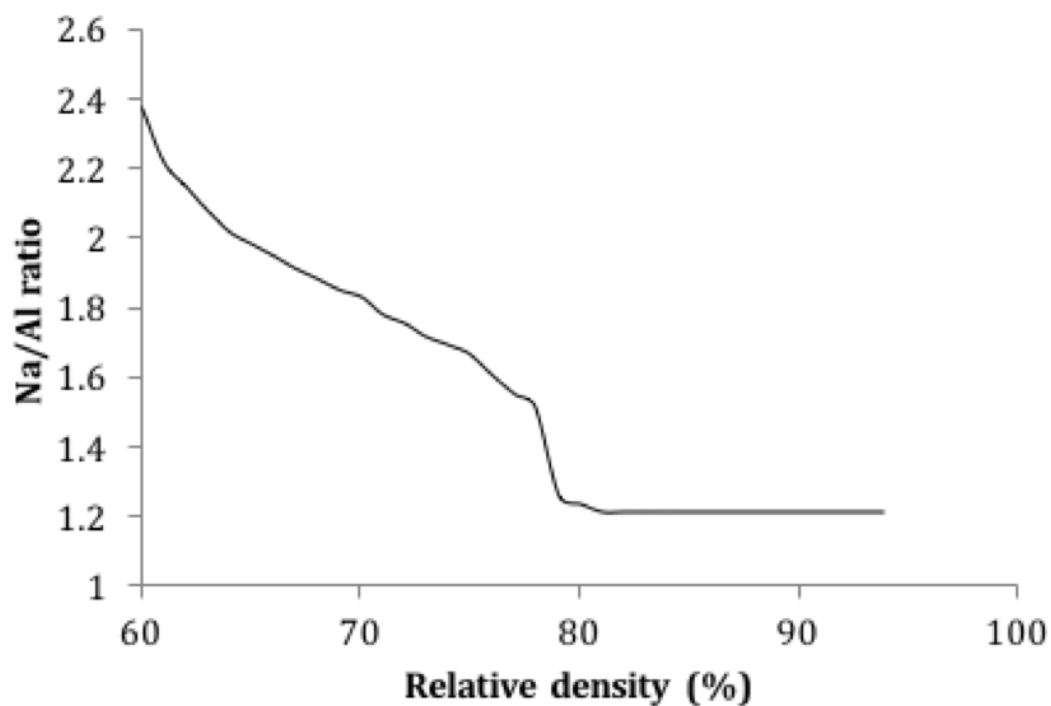


**Figure 4.5.** Change in Na/Al ion ratio in the liquid phase during sintering of samples with  $\text{Na}_2\text{O}/\text{SiO}_2$  ratios  $> 0.5$ .

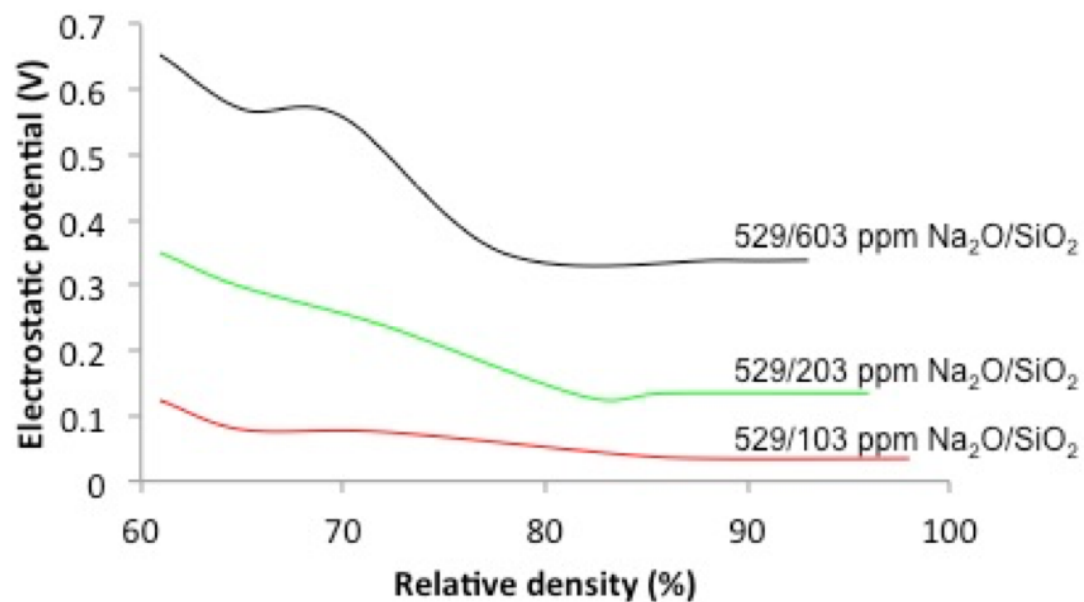


**Figure 4.6.** Development of the electrostatic potential as a function of relative density. For MgO-free powder samples with 529 ppm  $\text{Na}_2\text{O}$  and different  $\text{SiO}_2$  concentrations.

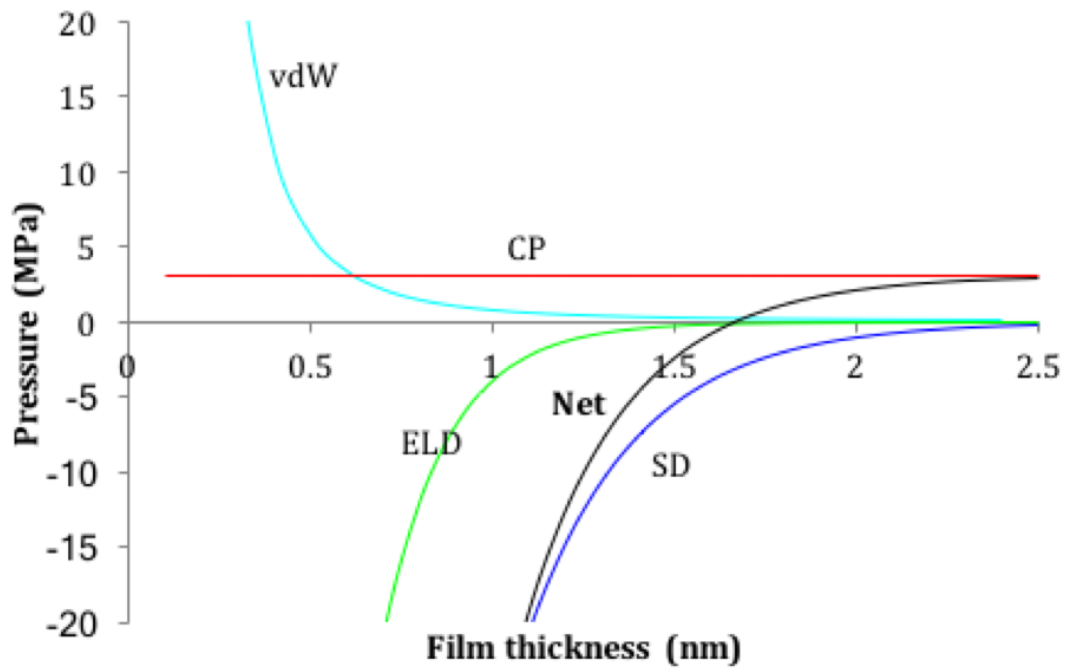


**Figure 4.7.** Contributions to the equilibrium film thickness as a function of film thickness for MgO-free powder samples with 529/603 ppm Na<sub>2</sub>O/SiO<sub>2</sub> at a relative density of 93%.

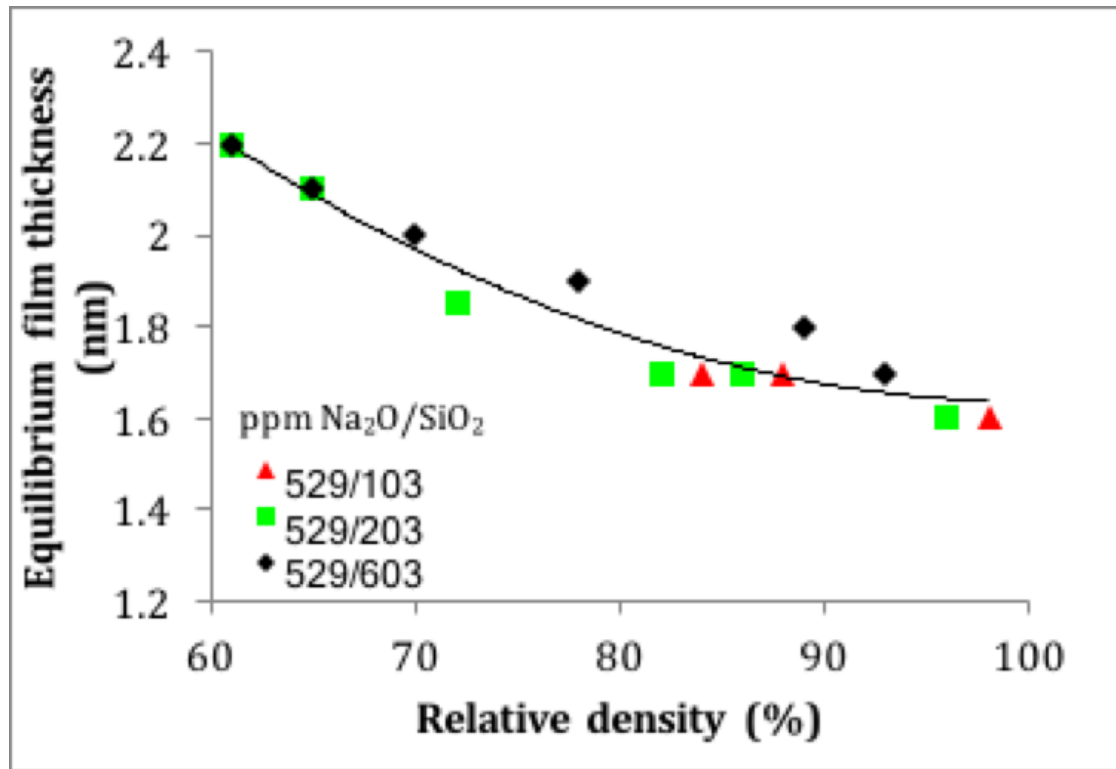


**Figure 4.8.** Calculated equilibrium film thickness for MgO-free powder samples at different chemistries as a function of relative density.

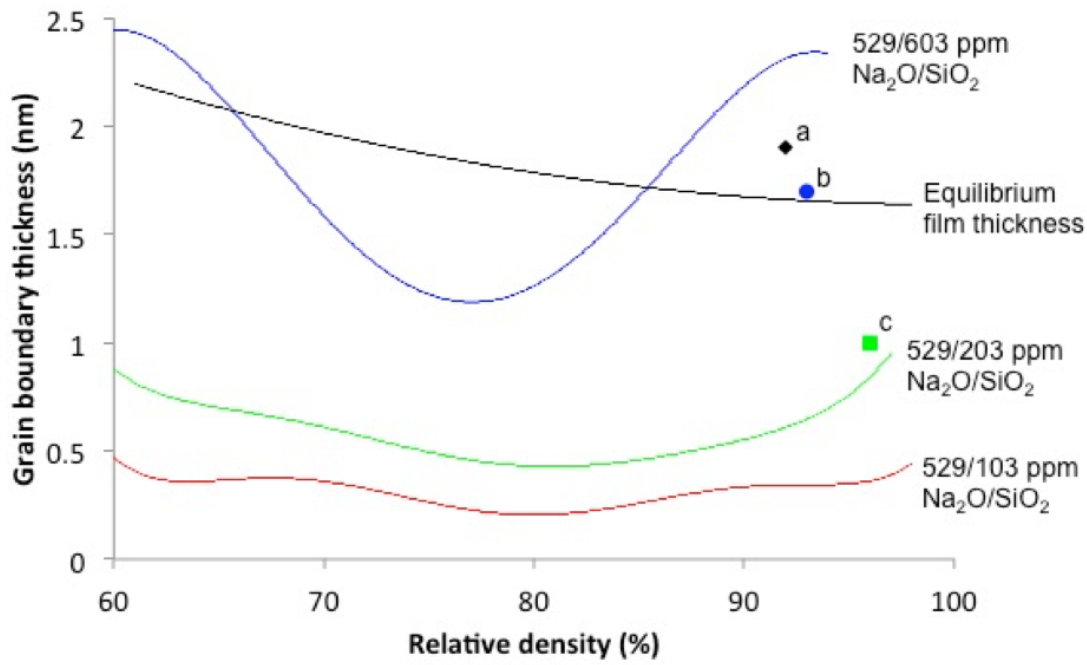


**Figure 4.9.** Calculated grain boundary thicknesses as a function of relative density for MgO-free powder samples. The trajectories labeled with 529/603 ppm  $\text{Na}_2\text{O}/\text{SiO}_2$ , 529/203 ppm  $\text{Na}_2\text{O}/\text{SiO}_2$ , and 529 ppm  $\text{Na}_2\text{O}/\text{SiO}_2$  were calculated based on the liquid phase concentration and sintering stage. The equilibrium film thickness was calculated based on Clarke's model. The calculated grain boundary thicknesses are compared to measured grain boundary thicknesses (data points a: 1000/1000 ppm  $\text{Na}_2\text{O}/\text{SiO}_2$ , b) 529/603 ppm  $\text{Na}_2\text{O}/\text{SiO}_2$ , c) 529/203 ppm  $\text{Na}_2\text{O}/\text{SiO}_2$  after heating at 1525°C for 3 h).

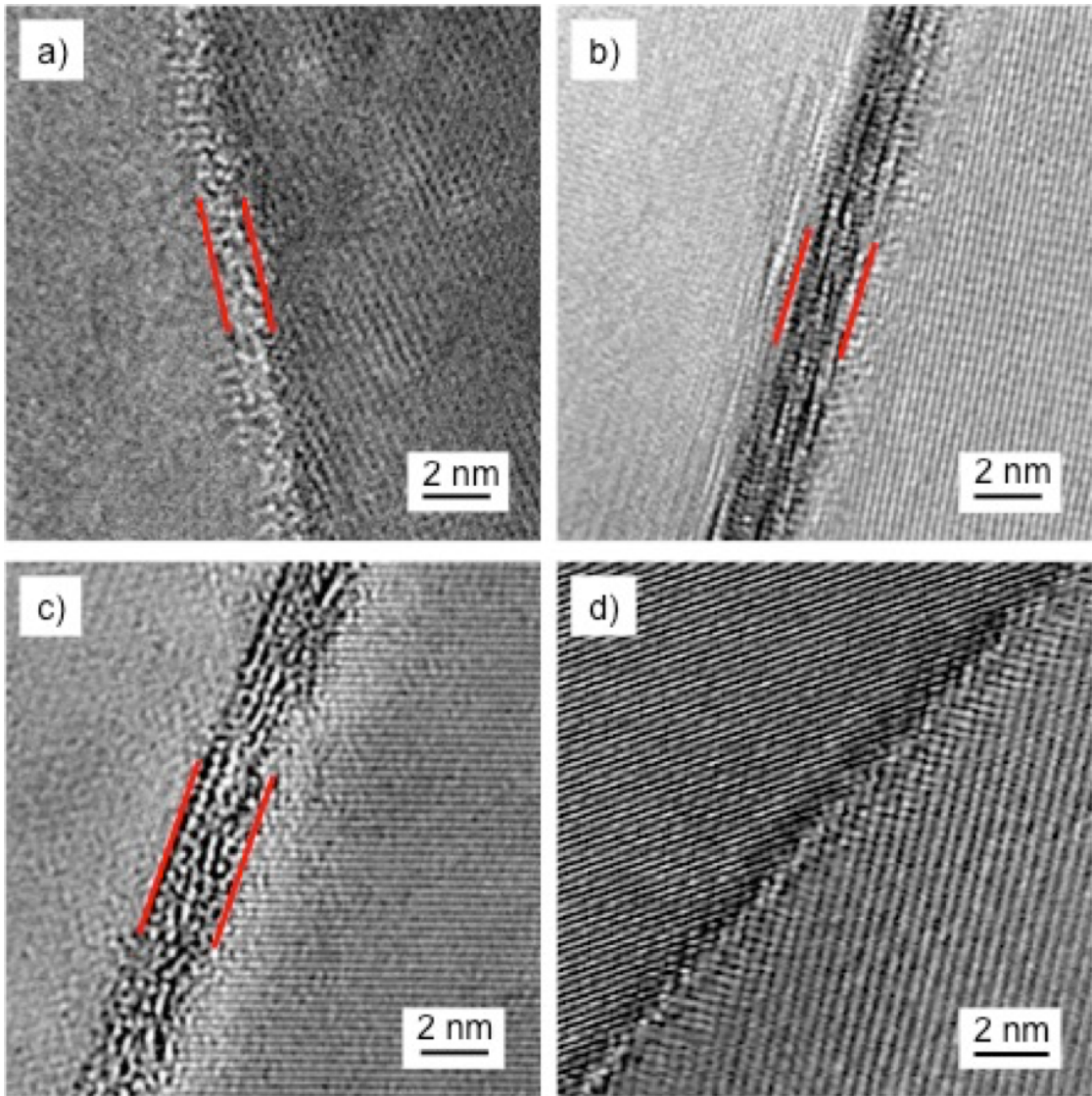


**Figure 4.10.** TEM images of MgO-free powder samples with a) 529/203 ppm Na<sub>2</sub>/SiO<sub>2</sub>, b) 529/603 ppm Na<sub>2</sub>/SiO<sub>2</sub>, c) 1000/1000 ppm Na<sub>2</sub>/SiO<sub>2</sub>, and d) 29/103 ppm Na<sub>2</sub>/SiO<sub>2</sub> after sintering at 1525°C for 3 h.

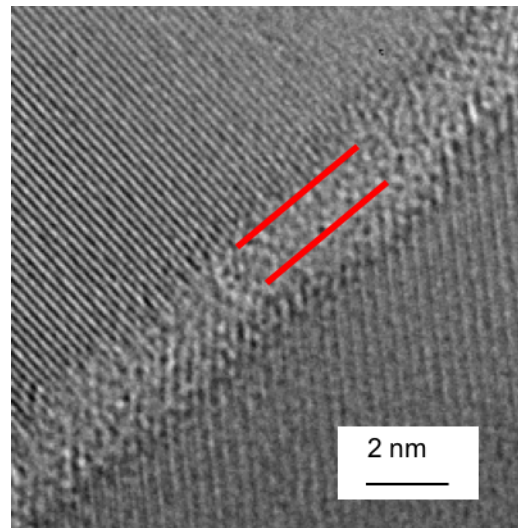


**Figure 4.11.** TEM image of a MgO-free powder sample with 29/603 ppm Na<sub>2</sub>O/SiO<sub>2</sub>.

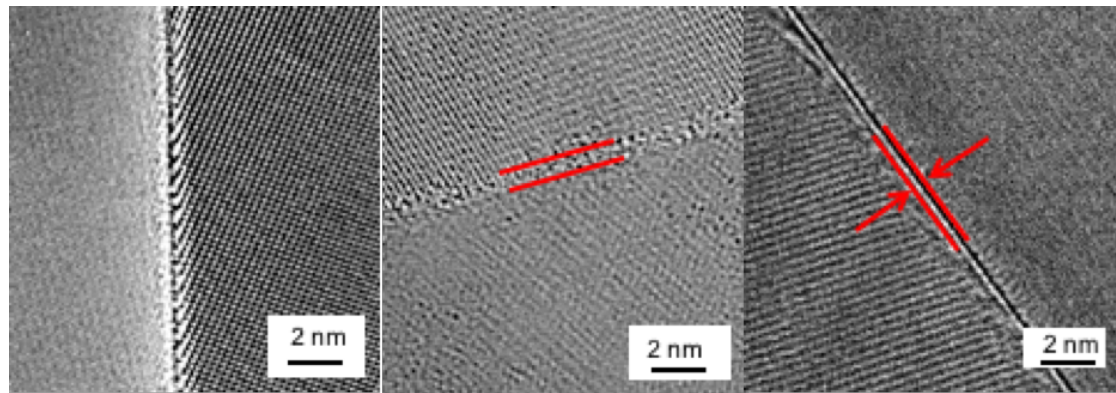


**Figure 4.12.** TEM images of MgO-doped (380 ppm) powder samples with a) 60/82 ppm Na<sub>2</sub>O/SiO<sub>2</sub>, b) 60/582 ppm Na<sub>2</sub>O/SiO<sub>2</sub>, and c) 560/582 ppm Na<sub>2</sub>O/SiO<sub>2</sub>. After heating at 1525°C for 3 h.

# Chapter 5 |

# Second phase formation in Bayer alumina

## 5.1 Introduction

It is reported in the literature that dopants and impurities such as MgO, CaO, and Na<sub>2</sub>O can form second phases such as spinel, calcium hexaluminate, and  $\beta$ -Al<sub>2</sub>O<sub>3</sub>, respectively, if their concentration is high enough. For Bayer aluminas  $\beta$ -Al<sub>2</sub>O<sub>3</sub> is of particular interest because Na<sub>2</sub>O impurities are characteristic to Bayer alumina and small amounts of a few hundred ppm can be sufficient to form  $\beta$ -Al<sub>2</sub>O<sub>3</sub>. Rankin and Merwin [38] were the first to observe the formation of a new alumina phase in the high Al<sub>2</sub>O<sub>3</sub> region in the system CaO-Al<sub>2</sub>O<sub>3</sub>-MgO. They believed it was an allotropic modification of Al<sub>2</sub>O<sub>3</sub>, and named it  $\beta$ -Al<sub>2</sub>O<sub>3</sub>. However, later work clarified that there is a relation between the alkali content in the Al<sub>2</sub>O<sub>3</sub> and the formation of  $\beta$ -Al<sub>2</sub>O<sub>3</sub> [92], and that  $\beta$ -Al<sub>2</sub>O<sub>3</sub> is an alkali aluminate, rather than an allotropic form of Al<sub>2</sub>O<sub>3</sub> [44]. Ridgway et al. [39] reported that the Na<sub>2</sub>O content in Bayer process alumina can be high enough for the formation of  $\beta$ -Al<sub>2</sub>O<sub>3</sub>, and that  $\beta$ -Al<sub>2</sub>O<sub>3</sub> forms in "dry ore process" Al<sub>2</sub>O<sub>3</sub> (with unspecified low concentrations of Na<sub>2</sub>O) only when Na<sub>2</sub>O or K<sub>2</sub>O is added. Four types of  $\beta$ -Al<sub>2</sub>O<sub>3</sub> exist; two of them,  $\beta$ -Al<sub>2</sub>O<sub>3</sub> (Na<sub>2</sub>O\*11Al<sub>2</sub>O<sub>3</sub>) and  $\beta''$ -Al<sub>2</sub>O<sub>3</sub> (Na<sub>2</sub>O\*5Al<sub>2</sub>O<sub>3</sub>), form in the binary system Na<sub>2</sub>O-Al<sub>2</sub>O<sub>3</sub>, and can incorporate MgO. The other two beta aluminas,  $\beta'''$ -Al<sub>2</sub>O<sub>3</sub> and  $\beta''''$ -Al<sub>2</sub>O<sub>3</sub> are found in the ternary system Na<sub>2</sub>O-Al<sub>2</sub>O<sub>3</sub>-MgO [42]. For completeness it should be mentioned that the existence of a  $\beta'$ -Al<sub>2</sub>O<sub>3</sub> (Na<sub>2</sub>O\*7Al<sub>2</sub>O<sub>3</sub>) has been reported as well, but subsequent literature is in agreement

that  $\beta'$ -Al<sub>2</sub>O<sub>3</sub> is actually  $\beta$ -Al<sub>2</sub>O<sub>3</sub> with excess Na<sub>2</sub>O [42].

The formation and stability of  $\beta$ -Al<sub>2</sub>O<sub>3</sub> has been extensively studied in the literature because its excellent ion conductivity makes it suitable for applications as a solid electrolyte; especially for use in batteries. Most reported preparation routes involve sodium carbonate and alumina [44, 93, 94]. Heating mixtures of alumina and sodium carbonate to 1100°C leads to the formation of  $\beta''$ -Al<sub>2</sub>O<sub>3</sub>, which decomposes to  $\beta$ -Al<sub>2</sub>O<sub>3</sub> and NaAlO<sub>2</sub> at temperatures >1500°C. The equilibrium vapor pressure of Na<sub>2</sub>O over  $\beta$ -Al<sub>2</sub>O<sub>3</sub> has been reported to be "appreciable" at temperatures >1400°C [93], where  $\beta$ -Al<sub>2</sub>O<sub>3</sub> can decompose to  $\alpha$ -Al<sub>2</sub>O<sub>3</sub> by volatilization of Na<sub>2</sub>O. However, soda loss has been reported to occur at lower temperatures as well, e.g. 6.4 wt% of soda loss was reported by de Vries and Roth [44] when they prepared  $\beta''$ -alumina samples and heated it for 4 h at 1100 °C. On the other hand, Gallup [52] investigated the stability of  $\beta$ -Al<sub>2</sub>O<sub>3</sub> at high temperatures and under different atmospheres and he reported that  $\beta$ -Al<sub>2</sub>O<sub>3</sub> can convert to  $\alpha$ -Al<sub>2</sub>O<sub>3</sub> at temperatures as low as 1300°C in hydrogen or vacuum atmosphere, but in air no conversion was observed for heating as long as 1 h at 1500°C. Full conversion was observed when the material was heated for 10 min at 1600°C.

Even though the conditions for the formation of  $\beta$ -Al<sub>2</sub>O<sub>3</sub> in  $\alpha$ -Al<sub>2</sub>O<sub>3</sub> ceramics are of great importance, especially because the Na<sub>2</sub>O content in Bayer process Al<sub>2</sub>O<sub>3</sub> is sufficient for the formation of  $\beta$ -Al<sub>2</sub>O<sub>3</sub>, it is barely studied in literature. Duncan and Creyke [40] investigated the formation and stability of  $\beta$ -Al<sub>2</sub>O<sub>3</sub> in  $\alpha$ -Al<sub>2</sub>O<sub>3</sub> ceramics and used two commercial alumina powders with impurities of 0.038 wt% SiO<sub>2</sub>, 0.006 wt% MgO and 0.061 ppm Na<sub>2</sub>O, and 0.04 wt% SiO<sub>2</sub>, 0.2 wt% MgO and 0.04 wt% Na<sub>2</sub>O, respectively. They reported that  $\beta$ -Al<sub>2</sub>O<sub>3</sub> can form at Na<sub>2</sub>O concentrations as low as 300 ppm if a small amount of MgO is present. They estimated the amount of  $\beta$ -Al<sub>2</sub>O<sub>3</sub> by measuring the dielectric loss of the sample, since  $\beta$ -Al<sub>2</sub>O<sub>3</sub> was observed to increase the dielectric loss of  $\alpha$ -Al<sub>2</sub>O<sub>3</sub> samples. An increase in amount of  $\beta$ -Al<sub>2</sub>O<sub>3</sub> was observed with increasing Na<sub>2</sub>O, but also with increasing MgO additions, and it was shown by electron-probe microanalysis that there is a higher concentration of Na<sub>2</sub>O and MgO in the  $\beta$ -Al<sub>2</sub>O<sub>3</sub> grains. They state that samples, in which  $\beta$ -Al<sub>2</sub>O<sub>3</sub> forms, show no formation of spinel [40] and furthermore they determined that  $\beta$ -Al<sub>2</sub>O<sub>3</sub> in  $\alpha$ -Al<sub>2</sub>O<sub>3</sub> is stable to up to 1650 °C in stagnant air. In a flowing air stream, however, decomposition to  $\alpha$ -Al<sub>2</sub>O<sub>3</sub> takes place, even in the center of the sample and the decomposition is facilitated by

open porosity and higher temperatures, whereas a high degree of compaction of the powder, e.g. a high green density, impedes the decomposition. Small amounts of other oxides (e.g. SiO<sub>2</sub>, MgO, ZrO<sub>2</sub>) are reported to facilitate the decomposition process due to an easier diffusion path through the grain boundaries. The work by Duncan and Creyke focuses on the decomposition and while some literature reports indicate under what conditions  $\beta$ -Al<sub>2</sub>O<sub>3</sub> may form [40], there is no systematic study on the formation of  $\beta$ -Al<sub>2</sub>O<sub>3</sub> as function of powder chemistry, at what sintering stage  $\beta$ -Al<sub>2</sub>O<sub>3</sub> forms and what possible formation mechanisms are. Goal of this work is to identify the stages and mechanisms of  $\beta$ -Al<sub>2</sub>O<sub>3</sub> formation in  $\alpha$ -Al<sub>2</sub>O<sub>3</sub>.

## 5.2 Experimental

The samples fabricated for the investigations in Chapters 2 and 3 were used to investigate the formation of  $\beta$ -Al<sub>2</sub>O<sub>3</sub> in  $\alpha$ -Al<sub>2</sub>O<sub>3</sub>. To investigate the influence of MgO concentration on the formation of  $\beta$ -Al<sub>2</sub>O<sub>3</sub> the MgO-free powder used in Chapter 2 was also doped with up to 1000 ppm MgO using magnesium nitrate hexahydrate (Mg(NO<sub>3</sub>)<sub>2</sub>\*6H<sub>2</sub>O, 99.97%, Alfa Aesar, Ward Hill, MA, USA). The alumina powder was dispersed in aqueous magnesium nitrate solution and stirred on a magnetic stir plate for 5 h at room temperature, and then held at 80 °C for 24 h until the mixture was too viscous to stir. The mixture was then placed in a drying oven at 100 °C for 24 h to thoroughly dry the powder. Additionally, an ultra-high purity powder (AKP-50, Sumitomo Chemical Co. Ltd., Tokyo, Japan) was doped with up to 2000 ppm Na<sub>2</sub>O, 500 ppm SiO<sub>2</sub>, and 500 ppm MgO and used to dry press samples. The intrinsic impurities in the ultra high purity powder are 11 ppm SiO<sub>2</sub>, 4 ppm Fe<sub>2</sub>O<sub>3</sub>, 2 ppm Na<sub>2</sub>O, 2 ppm MgO, and 1 ppm Cu. The doping and sample preparation procedure is described in detail in chapters 2 and 3.

## 5.3 Results

Initially the detection of  $\beta$ -Al<sub>2</sub>O<sub>3</sub> in an  $\alpha$ -Al<sub>2</sub>O<sub>3</sub> matrix was investigated. Figure 5.1a-c shows SEM micrographs of  $\beta$ -Al<sub>2</sub>O<sub>3</sub> grains in a sample with 529 ppm Na<sub>2</sub>O, 103 ppm SiO<sub>2</sub>, and 380 ppm MgO sintered at 1525°C for 3 h. It can be seen that in unetched samples  $\beta$ -Al<sub>2</sub>O<sub>3</sub> grains can hardly be observed in images obtained from secondary electrons (Figure 5.1a). Figure 5.1b shows an SEM image of the

same area of the sample as Figure 5.1a obtained from the backscattered electrons and a stronger contrast between the  $\beta$ -Al<sub>2</sub>O<sub>3</sub> grains and the surrounding  $\alpha$ -Al<sub>2</sub>O<sub>3</sub> matrix can be seen, which is due to the higher sensitivity of backscattered electrons to density.  $\beta$ -Al<sub>2</sub>O<sub>3</sub> grains appear darker due to the lower density (3.31 g/cm<sup>3</sup>) compared to  $\alpha$ -Al<sub>2</sub>O<sub>3</sub> (3.986 g/cm<sup>3</sup>). Figure 5.1c shows a  $\beta$ -Al<sub>2</sub>O<sub>3</sub> grain after thermal etching at 1425°C for 40 min and it can be seen that the  $\beta$ -Al<sub>2</sub>O<sub>3</sub> grain has evaporated during thermal etching, leaving a platelet shaped hole in the etched microstructure. It is interesting to note that samples with low Na<sub>2</sub>O concentrations such as 29 ppm form  $\beta$ -Al<sub>2</sub>O<sub>3</sub> grains that do not evaporate during thermal etching, as seen in Figure 5.1d. SEM micrographs obtained from backscattered electrons were used to detect  $\beta$ -Al<sub>2</sub>O<sub>3</sub> grains for the following investigations.

### 5.3.1 Influence of MgO on the formation of $\beta$ -Al<sub>2</sub>O<sub>3</sub>

Figure 5.2a shows the influence of MgO concentration on the number of  $\beta$ -Al<sub>2</sub>O<sub>3</sub> grains after sintering at 1525°C for 3 h. It can be seen that for a MgO concentration of 2 ppm no  $\beta$ -Al<sub>2</sub>O<sub>3</sub> was observed, and with increasing the MgO concentration the number of  $\beta$ -Al<sub>2</sub>O<sub>3</sub> grains that form increases up to 502 ppm MgO, but does not increase further when the MgO concentration is increased to 1002 ppm. This shows that MgO assists the formation of  $\beta$ -Al<sub>2</sub>O<sub>3</sub>. The influence of Na<sub>2</sub>O concentration on the number of  $\beta$ -Al<sub>2</sub>O<sub>3</sub> grains in MgO-free Bayer alumina after sintering at 1525°C for 3 h is shown in Figure 5.2b. It can be seen that only a small number of  $\beta$ -Al<sub>2</sub>O<sub>3</sub> grains form for concentrations  $\leq$  529 ppm Na<sub>2</sub>O, but for higher concentrations, such as 1029 ppm, the number of  $\beta$ -Al<sub>2</sub>O<sub>3</sub> grains increases significantly. Since commercial Bayer aluminas are typically doped with MgO, the following investigations are focused on Bayer alumina powder that was doped with 380 ppm MgO.

### 5.3.2 MgO-doped Bayer alumina

#### 5.3.2.1 Number frequency of $\beta$ -Al<sub>2</sub>O<sub>3</sub> grains

Figure 5.3 shows the influence of the Na<sub>2</sub>O and SiO<sub>2</sub> concentration on the number density of  $\beta$ -Al<sub>2</sub>O<sub>3</sub> grains in Bayer alumina powder doped with 380 ppm MgO. It can be seen that the number density of  $\beta$ -Al<sub>2</sub>O<sub>3</sub> grains increases with increasing Na<sub>2</sub>O concentration (Figure 5.3a), but decreases as a function of SiO<sub>2</sub> concentration

in samples with different  $\text{Na}_2\text{O}$  concentrations (Figure 5.3b). This indicates that the  $\text{Na}_2\text{O}/\text{SiO}_2$  ratio determines the number density of  $\beta\text{-Al}_2\text{O}_3$  grains. Figure 5.3c shows the number density of  $\beta\text{-Al}_2\text{O}_3$  grains as a function of the  $\text{Na}_2\text{O}/\text{SiO}_2$  ratio, and it can be seen that the number density of  $\beta\text{-Al}_2\text{O}_3$  grains increases linearly with increasing  $\text{Na}_2\text{O}/\text{SiO}_2$  ratio.

The kinetics of  $\beta\text{-Al}_2\text{O}_3$  formation at 1525°C for different powder chemistries (MgO-doped Bayer alumina) is shown in Figure 5.4. Most  $\beta\text{-Al}_2\text{O}_3$  grains forms within the first hour at 1525°C, and after that the number density of  $\beta\text{-Al}_2\text{O}_3$  grains does not change for all chemistries. In contrast, for samples prepared from ultra high purity powder (AKP-50) the amount of  $\beta\text{-Al}_2\text{O}_3$  that forms during sintering in the temperature range from 1450°C to 1600°C for up to 8 h does not change, regardless of the  $\text{Na}_2\text{O}$ , MgO, or  $\text{SiO}_2$  concentrations. However, in the ultra-high purity powder it was observed that increasing the  $\text{Na}_2\text{O}$  and MgO concentrations increases the number of  $\beta\text{-Al}_2\text{O}_3$  grains in the microstructures, and increasing the  $\text{SiO}_2$  concentration decreases the number of  $\beta\text{-Al}_2\text{O}_3$  grains in the microstructures, similar to the Bayer alumina powder.

### 5.3.2.2 Size of $\beta\text{-Al}_2\text{O}_3$ grains

Figure 5.5 shows micrographs of samples with different powder chemistries with up to 1000 ppm MgO,  $\text{Na}_2\text{O}$ , and  $\text{SiO}_2$  after sintering at 1525°C for 3 h. It can be seen that the size of the  $\beta\text{-Al}_2\text{O}_3$  grains changes as a function of powder chemistry. Samples with 1000 ppm MgO, 1000 ppm  $\text{SiO}_2$ , and 29 ppm  $\text{Na}_2\text{O}$  form 30-40  $\mu\text{m}$  long  $\beta\text{-Al}_2\text{O}_3$  grains (Figure 5.5a). The  $\beta\text{-Al}_2\text{O}_3$  grains that form in samples with 2 ppm MgO, 1000 ppm  $\text{SiO}_2$ , and 1000 ppm  $\text{Na}_2\text{O}$  are 10-20  $\mu\text{m}$  long (Figure 5.5b), and the  $\beta\text{-Al}_2\text{O}_3$  grains in samples with 1000 ppm MgO, 1000 ppm  $\text{SiO}_2$ , and 1000 ppm  $\text{Na}_2\text{O}$  are 4-10  $\mu\text{m}$  long (Figure 5.5c). Note that no  $\beta\text{-Al}_2\text{O}_3$  was observed in samples with 29 ppm  $\text{Na}_2\text{O}$  and 2 ppm MgO, regardless of the  $\text{SiO}_2$  concentration.

Micrographs of MgO-doped (380 ppm) Bayer alumina with  $\text{Na}_2\text{O}$  concentrations of up to 1060 ppm  $\text{Na}_2\text{O}$  sintered at 1525°C for 3 h are shown in Figure 5.6. The  $\beta\text{-Al}_2\text{O}_3$  grains are 3-13  $\mu\text{m}$  long for samples with 185 ppm  $\text{Na}_2\text{O}$  and 4-10  $\mu\text{m}$  for samples with 560 ppm  $\text{Na}_2\text{O}$ , and if the  $\text{Na}_2\text{O}$  concentration is increased to 1060 ppm the  $\beta\text{-Al}_2\text{O}_3$  grains are significantly smaller (2-7  $\mu\text{m}$ ).

Micrographs of samples with 185/182 ppm  $\text{Na}_2\text{O}/\text{SiO}_2$  and 560/182 ppm  $\text{Na}_2\text{O}/\text{SiO}_2$  after sintering at 1525°C for 3 h are shown in Figure 5.7. The  $\text{Na}_2\text{O}$

concentrations in those samples are the same as in the samples in Figure 5.6a and b, respectively. However, the samples in Figure 5.7 contain 100 ppm more SiO<sub>2</sub>. It can be seen that higher SiO<sub>2</sub> concentrations lead to larger  $\beta$ -Al<sub>2</sub>O<sub>3</sub> grains compared to samples with lower SiO<sub>2</sub> concentrations.

Figure 5.8 shows micrographs of MgO-doped (380 ppm) Bayer alumina samples with 560 ppm Na<sub>2</sub>O and 82 ppm SiO<sub>2</sub> after heating for 0 h, 1 h, and 8 h. It can be seen that the size of the  $\beta$ -Al<sub>2</sub>O<sub>3</sub> grains does not change as a function of sintering time. However, as shown in Figure 5.4, the number of the  $\beta$ -Al<sub>2</sub>O<sub>3</sub> grains increases with increasing sintering time.

Figure 5.9 show the XRD pattern of a polished sample with 1060 ppm Na<sub>2</sub>O, 582 ppm SiO<sub>2</sub> and 380 ppm MgO after sintering at 1525°C for 5 h. The pattern shows that there is a small amount of  $\beta$ -Al<sub>2</sub>O<sub>3</sub> present with P6<sub>3</sub>/mmc crystal structure, which can be assigned to  $\beta$ -Al<sub>2</sub>O<sub>3</sub>. The estimated amount of  $\beta$ -Al<sub>2</sub>O<sub>3</sub> from the XRD pattern is 0.6 wt.%. EDS reveals that the  $\beta$ -Al<sub>2</sub>O<sub>3</sub> grains contain higher concentrations of MgO and Na<sub>2</sub>O compared to the surrounding matrix.

Since the type of  $\beta$ -Al<sub>2</sub>O<sub>3</sub> that forms is known a theoretical volume fraction of  $\beta$ -Al<sub>2</sub>O<sub>3</sub> can be estimated based on the chemical formula of  $\beta$ -Al<sub>2</sub>O<sub>3</sub> (Na<sub>2</sub>O\*11Al<sub>2</sub>O<sub>3</sub>) and the amount of Na<sub>2</sub>O in the samples, as seen in Table 5.1. The size of the  $\beta$ -Al<sub>2</sub>O<sub>3</sub> grains was measured from the SEM images (length and thickness) and an area fraction was estimated. The estimated area fraction is assumed to be equal to the volume fraction of  $\beta$ -Al<sub>2</sub>O<sub>3</sub> in the sample. It can be seen that the theoretically estimated amount of  $\beta$ -Al<sub>2</sub>O<sub>3</sub> that can form based on the amount of Na<sub>2</sub>O in the samples is higher than the observed amount of  $\beta$ -Al<sub>2</sub>O<sub>3</sub> in the samples. A possible explanation is that some amount of Na<sub>2</sub>O might volatize during sintering, as shown in Chapter 3. Taking into account that 35% of the Na<sub>2</sub>O might volatize during heating (Figure 3.12 Chapter 3), the expected amount of  $\beta$ -Al<sub>2</sub>O<sub>3</sub> in the samples is close to the observed amount of  $\beta$ -Al<sub>2</sub>O<sub>3</sub>, as seen in Table 5.1.

### 5.3.3 Interpretation and mechanisms of formation

TEM and EDS analysis showed that insoluble impurities and dopants such as Na<sub>2</sub>O, MgO, CaO and SiO<sub>2</sub> segregate to the grain boundaries. In general it can be assumed that second phases can form when the solubility of impurities and dopants in the bulk and in the grain boundaries is exceeded. In the MgO-free powder it can

be seen that no second phase forms for  $\text{Na}_2\text{O}$  concentrations of 29 ppm, and only a very small amount of  $\beta$ - $\text{Al}_2\text{O}_3$  forms in samples with 529 ppm  $\text{Na}_2\text{O}$ . When the  $\text{Na}_2\text{O}$  concentration is increased to 1029 ppm the amount of  $\beta$ - $\text{Al}_2\text{O}_3$  that forms increases drastically (Figure 5.2b). This indicates that the solubility of  $\text{Na}_2\text{O}$  in the grains and grain boundaries in the  $\text{MgO}$ -free alumina is  $\sim$ 500 ppm  $\text{Na}_2\text{O}$  (note the presence of 103 ppm  $\text{SiO}_2$  in the  $\text{MgO}$ -free powder). For higher  $\text{Na}_2\text{O}$  concentrations the grain boundaries supersaturate during sintering and  $\beta$ - $\text{Al}_2\text{O}_3$  forms. If the  $\text{SiO}_2$  concentration in  $\text{MgO}$ -free powder samples is increased no  $\beta$ - $\text{Al}_2\text{O}_3$  forms and we believe that  $\text{SiO}_2$  significantly increases the  $\text{Na}_2\text{O}$  solubility in the grain boundaries by forming a liquid grain boundary phase. The argument that  $\text{SiO}_2$  increases the solubility of  $\text{Na}_2\text{O}$  in the grain boundaries is further supported by the observation that a considerable number of  $\beta$ - $\text{Al}_2\text{O}_3$  grains form in the ultra high purity powder with 502 ppm  $\text{Na}_2\text{O}$ , 2 ppm  $\text{MgO}$  and 11 ppm  $\text{SiO}_2$ , as seen in Figure 5.10, whereas almost no  $\beta$ - $\text{Al}_2\text{O}_3$  grains were observed in  $\text{MgO}$ -free Bayer alumina samples with 529 ppm  $\text{Na}_2\text{O}$ , 2 ppm  $\text{MgO}$ , and 103 ppm  $\text{SiO}_2$ .

When the  $\text{MgO}$  concentration in Bayer alumina is increased  $\beta$ - $\text{Al}_2\text{O}_3$  forms at significantly lower  $\text{Na}_2\text{O}$  concentrations, e.g. at  $\text{Na}_2\text{O}$  concentrations as low as 29 ppm. The amount of  $\beta$ - $\text{Al}_2\text{O}_3$  that forms increases with increasing  $\text{MgO}$  concentration up to 502 ppm. We believe that this is because  $\text{MgO}$  removes  $\text{SiO}_2$  from the grain boundaries during sintering, as explained earlier, and this mechanism significantly decreases the solubility of  $\text{Na}_2\text{O}$  in the grain boundaries, leading to the nucleation of  $\beta$ - $\text{Al}_2\text{O}_3$ .

If it is assumed that  $\text{MgO}$  and  $\text{SiO}_2$  form the defect complex proposed earlier, and if it is assumed that  $\text{MgO}$  and  $\text{SiO}_2$  go into solid solution at equal amounts and that all  $\text{MgO}$  is consumed by this process,  $\text{MgO}$ -doped powder samples (380 ppm  $\text{MgO}$ ) with 82 and 182 ppm  $\text{SiO}_2$  do not have any  $\text{SiO}_2$  left in the grain boundaries. This reduction in the amount of  $\text{SiO}_2$  in the grain boundaries reduces the solubility of  $\text{Na}_2\text{O}$  in the grain boundaries significantly, leading to the precipitation of  $\beta$ - $\text{Al}_2\text{O}_3$ . Samples with 582 ppm  $\text{SiO}_2$  have 202 ppm  $\text{SiO}_2$  left in the grain boundaries after 380 ppm  $\text{MgO}$  and  $\text{SiO}_2$  co-dissolve into the alumina lattice, and the solubility of  $\text{Na}_2\text{O}$  in the grain boundaries is still high enough so that only few  $\beta$ - $\text{Al}_2\text{O}_3$  grains in this sample, due to the presence of 202 ppm  $\text{SiO}_2$ .

The process of  $\text{SiO}_2$  and  $\text{MgO}$  co-dissolving into the alumina lattice and the formation of  $\beta$ - $\text{Al}_2\text{O}_3$  happens at the same time, between 0 and 3 h at 1525°C,

which supports the hypothesis that  $\beta$ -Al<sub>2</sub>O<sub>3</sub> nucleates and grows as a result of supersaturation of the grain boundaries when MgO removes SiO<sub>2</sub> from the grain boundaries. However, samples with 560 ppm Na<sub>2</sub>O and 82 ppm SiO<sub>2</sub> form more  $\beta$ -Al<sub>2</sub>O<sub>3</sub> than samples with 560 ppm Na<sub>2</sub>O and 182 ppm SiO<sub>2</sub>, even though no SiO<sub>2</sub> should be in the grain boundaries for both samples. One reason could be that not all 380 ppm MgO and SiO<sub>2</sub> are consumed by this co-dissolution process, and a small amount SiO<sub>2</sub> might remain on the grain boundaries, which would increase the Na<sub>2</sub>O solubility.

Another possible explanation is that MgO has an additional effect on the formation of  $\beta$ -Al<sub>2</sub>O<sub>3</sub> in  $\alpha$ -Al<sub>2</sub>O<sub>3</sub>. It has been reported that MgO supports the formation of  $\beta$ -Al<sub>2</sub>O<sub>3</sub> in alumina, and samples with 560 ppm Na<sub>2</sub>O and 82 ppm SiO<sub>2</sub> have 100 ppm more MgO left in the grain boundaries than samples with 560 ppm Na<sub>2</sub>O and 182 ppm SiO<sub>2</sub>. Since EDS shows that MgO is in the  $\beta$ -Al<sub>2</sub>O<sub>3</sub> grains MgO might facilitate the formation of  $\beta$ -Al<sub>2</sub>O<sub>3</sub>.

## 5.4 Summary

**Table 5.1.** Estimated amount of  $\beta$ -Al<sub>2</sub>O<sub>3</sub> in MgO-doped (380 ppm) Bayer alumina samples after 3 h at 1525°C.

Concentration of Na <sub>2</sub> O in the sample (ppm)	Theoretical vol.% of $\beta$ -Al <sub>2</sub> O <sub>3</sub>		Measured amount of $\beta$ -Al <sub>2</sub> O <sub>3</sub> 3h 1525°
	No Na <sub>2</sub> O volatizes	Assuming 35 % of Na <sub>2</sub> O volatizes	
60	0.14	0.09	0.18
185	0.42	0.28	0.25
310	0.71	0.46	0.38
560	1.28	0.84	0.65
1060	2.42	1.58	0.49

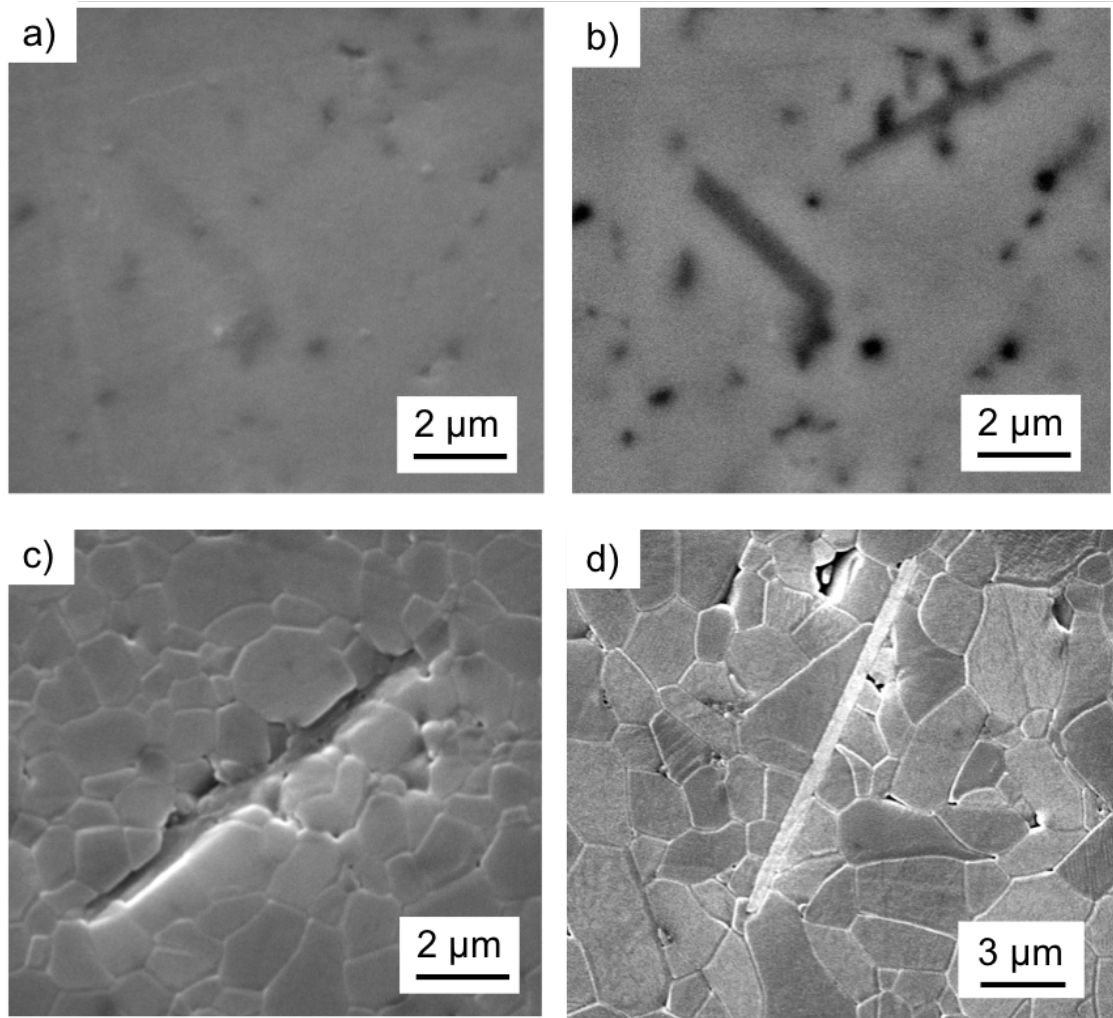


**Figure 5.1.** SEM micrographs of  $\beta$ - $\text{Al}_2\text{O}_3$  grains in a-c) Bayer alumina with 560 ppm  $\text{Na}_2\text{O}$ , 82 ppm  $\text{SiO}_2$ , and 380 ppm  $\text{MgO}$  after 3 h at 1525°C and d) Bayer alumina with 29 ppm  $\text{Na}_2\text{O}$ , 103 ppm  $\text{SiO}_2$ , and 502 ppm  $\text{MgO}$  after 3 h at 1525°C. The samples in a) and b) were not etched and the samples in c) and d) were etched. a), c), and d) were obtained using a secondary electron detector, and b) was obtained using a backscattered electron detector.

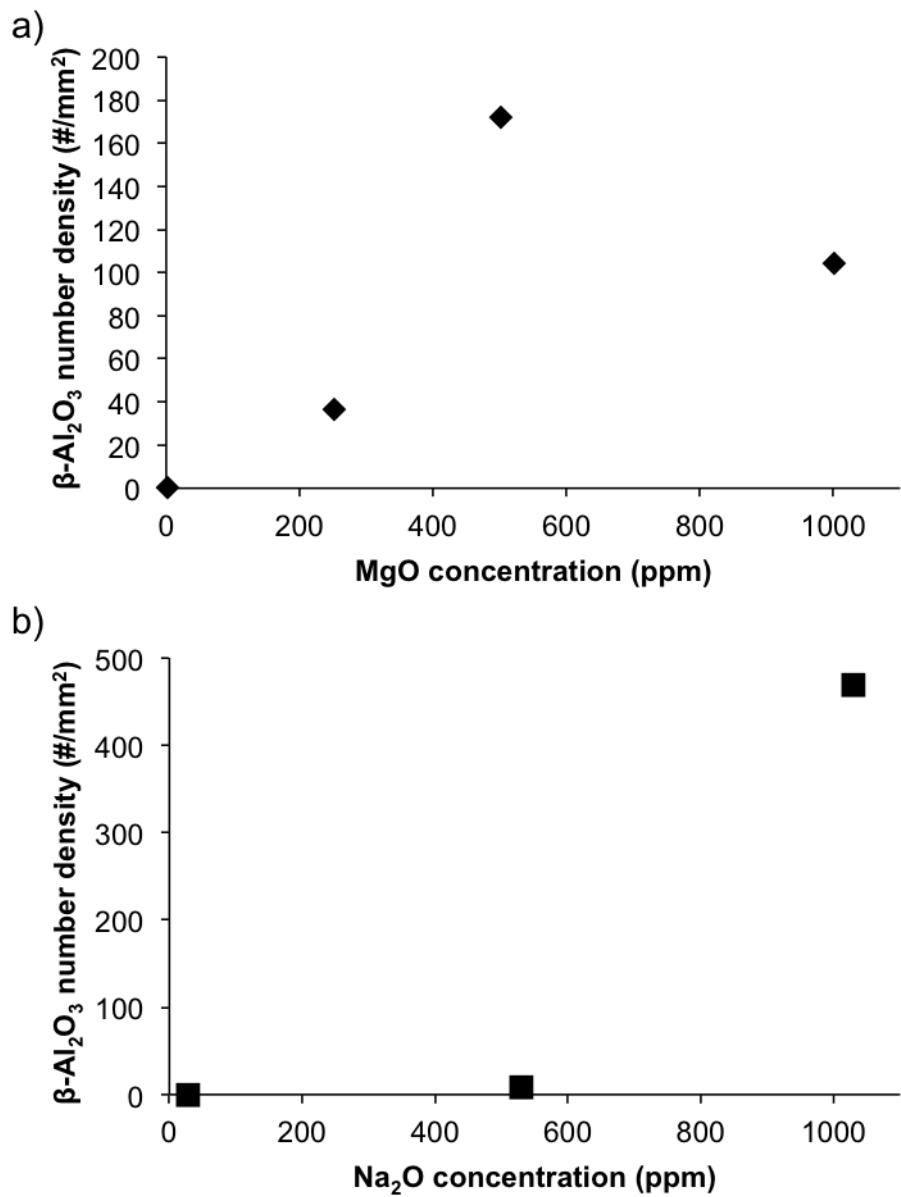


**Figure 5.2.** Formation of  $\beta$ -Al<sub>2</sub>O<sub>3</sub> in MgO-free powder samples as a function of a) MgO concentration and b) Na<sub>2</sub>O concentration in samples after 3 h at 1525°C.

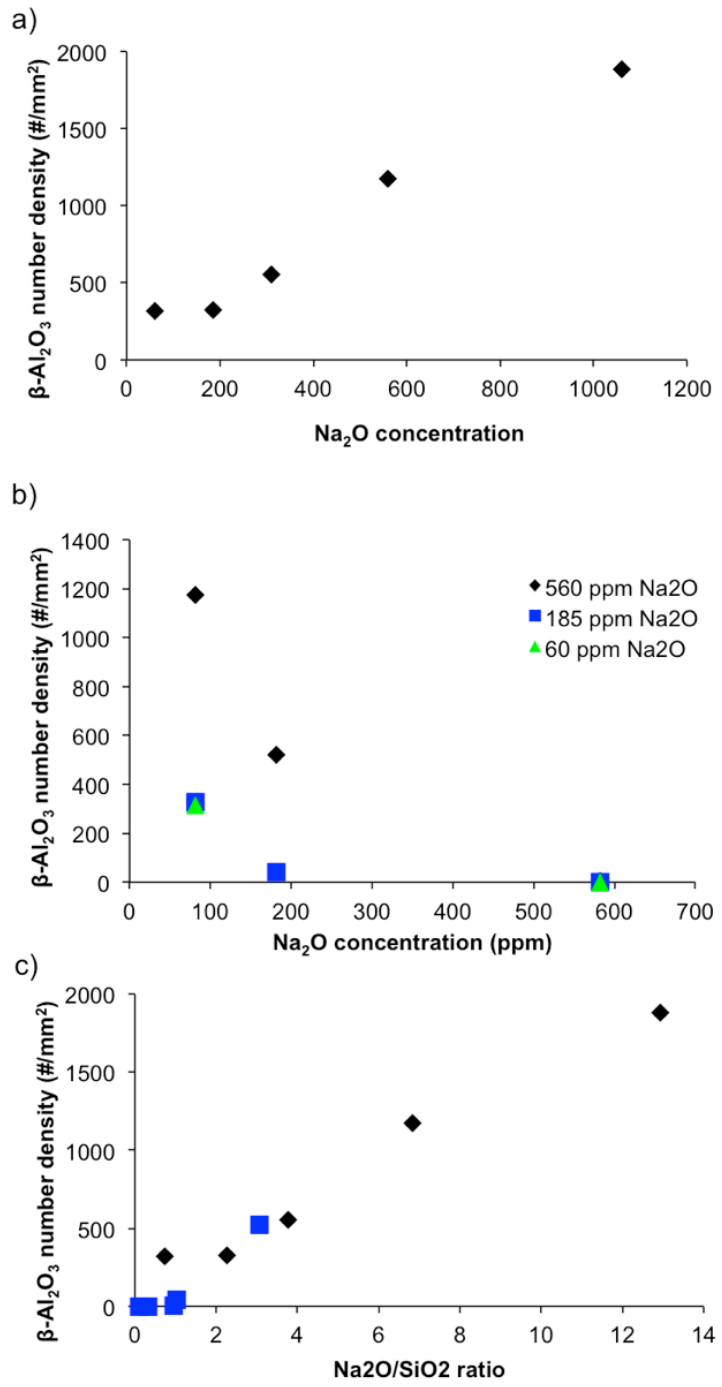


**Figure 5.3.** Formation of  $\beta$ - $\text{Al}_2\text{O}_3$  a function of a)  $\text{Na}_2\text{O}$  concentration, b)  $\text{SiO}_2$  concentration for different  $\text{Na}_2\text{O}$  concentrations, and c) of the  $\text{Na}_2\text{O}/\text{SiO}_2$  ratio in  $\text{MgO}$ -doped (380 ppm) powder samples. In c) the black diamonds are samples with 82 ppm  $\text{SiO}_2$  and the blue squares are samples with 182 and 582 ppm  $\text{SiO}_2$ .

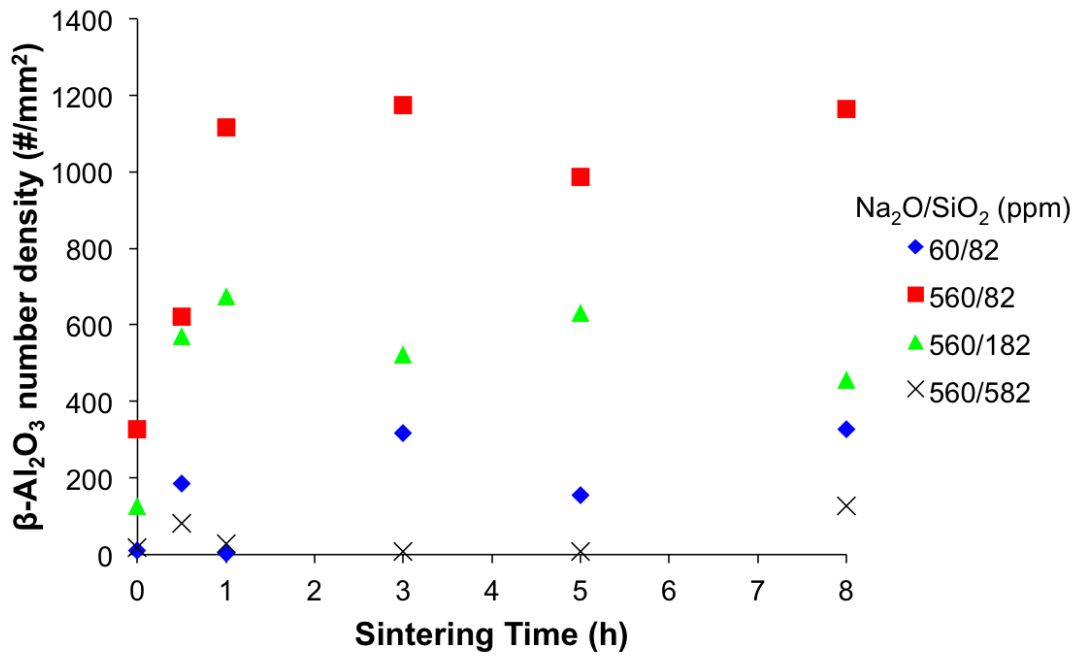


**Figure 5.4.** Kinetics of  $\beta$ -Al<sub>2</sub>O<sub>3</sub> formation for different powder chemistries of MgO-doped powder samples (380 ppm MgO).

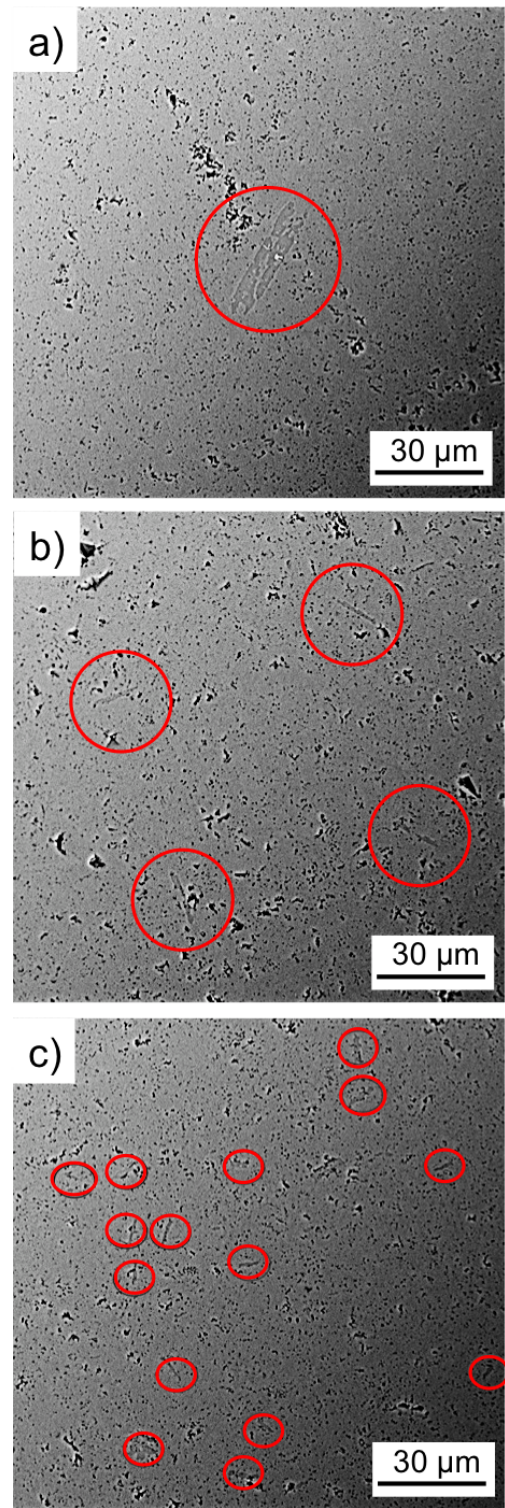


**Figure 5.5.** Micrographs showing  $\beta$ - $\text{Al}_2\text{O}_3$  grains (red circles) in Bayer alumina samples with a) 1000 ppm MgO, 1000 ppm SiO<sub>2</sub>, 29 ppm Na<sub>2</sub>O, b) 2 ppm MgO, 1000 ppm SiO<sub>2</sub>, 1000 ppm Na<sub>2</sub>O, c) 1000 ppm MgO, 1000 ppm SiO<sub>2</sub>, 1000 ppm Na<sub>2</sub>O after 3 h at 1525°C.

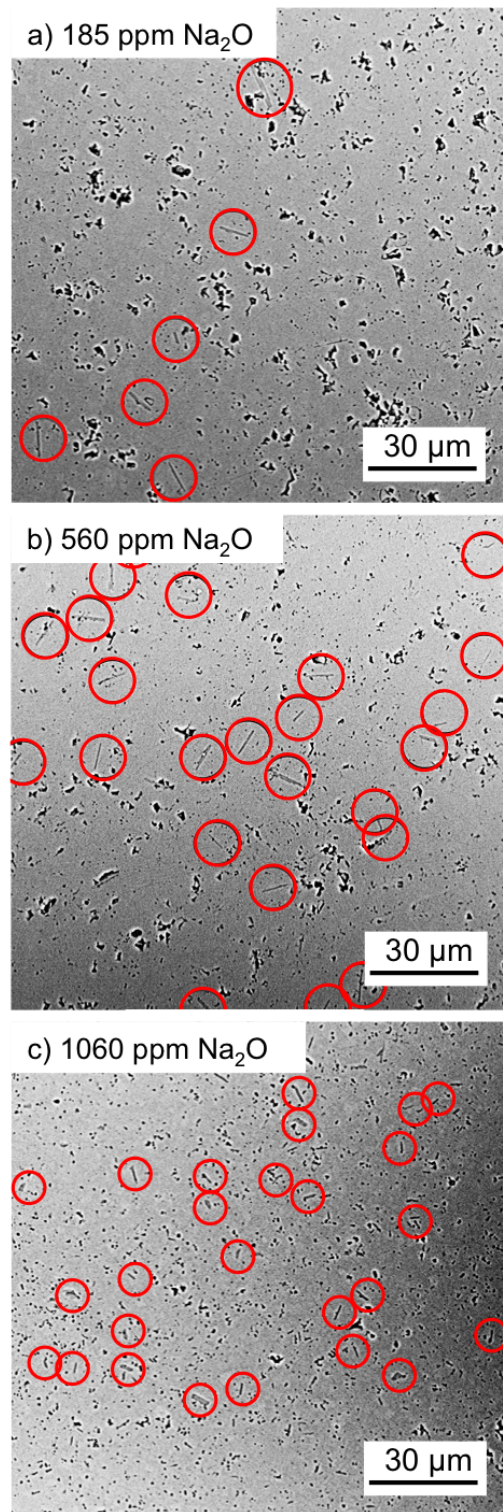


**Figure 5.6.** Micrographs showing  $\beta$ -Al<sub>2</sub>O<sub>3</sub> grains (red circles) in MgO-doped (380 ppm) Bayer alumina samples with 82 ppm SiO<sub>2</sub> and a) 185 ppm Na<sub>2</sub>O, b) 560 ppm Na<sub>2</sub>O, and c) 1060 ppm Na<sub>2</sub>O after sintering at 1525°C for 3 h.

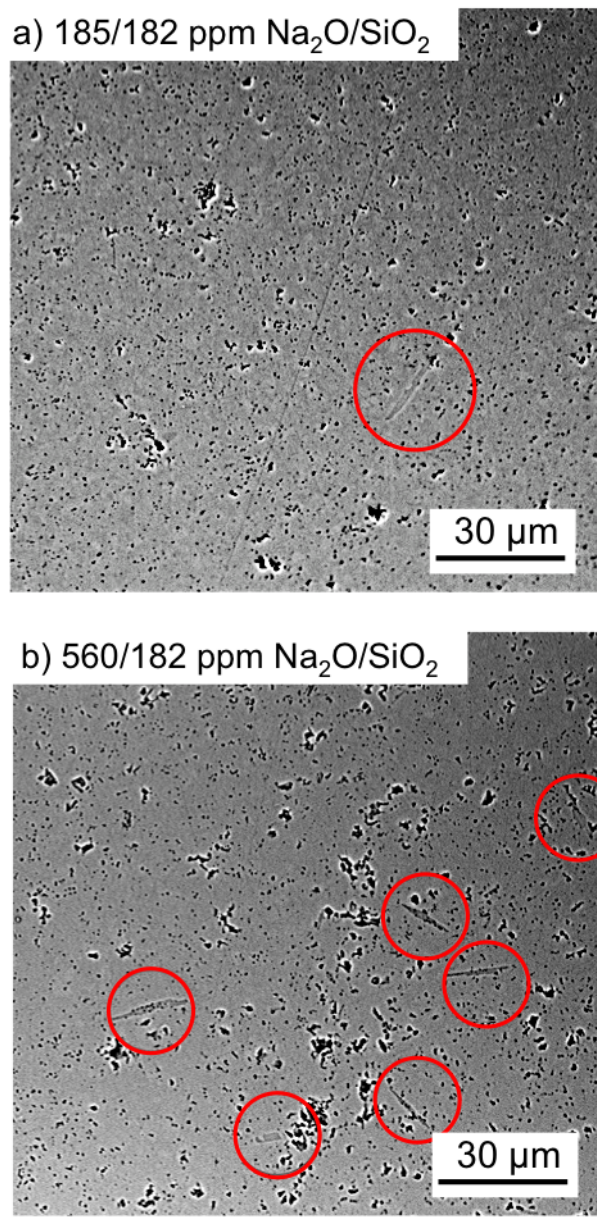


**Figure 5.7.** Micrographs showing  $\beta$ -Al<sub>2</sub>O<sub>3</sub> grains (red circles) in MgO-doped (380 ppm) Bayer alumina samples with a) 185/182 ppm Na<sub>2</sub>O/SiO<sub>2</sub> and b) 560/182 ppm Na<sub>2</sub>O/SiO<sub>2</sub> after sintering at 1525°C for 3 h.

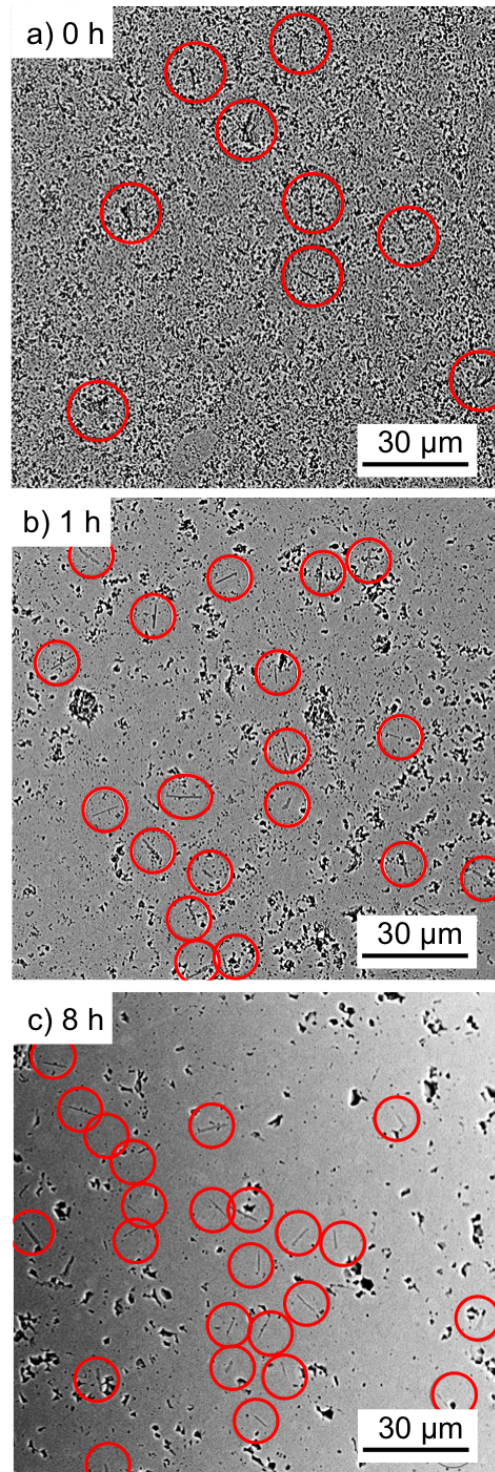


**Figure 5.8.** Micrographs showing  $\beta$ -Al<sub>2</sub>O<sub>3</sub> grains (red circles) in MgO-doped (380 ppm) Bayer alumina samples with 82 ppm SiO<sub>2</sub> and 560 ppm Na<sub>2</sub>O after sintering at 1525°C for a) 0 h, b) 1 h, and c) 8 h.

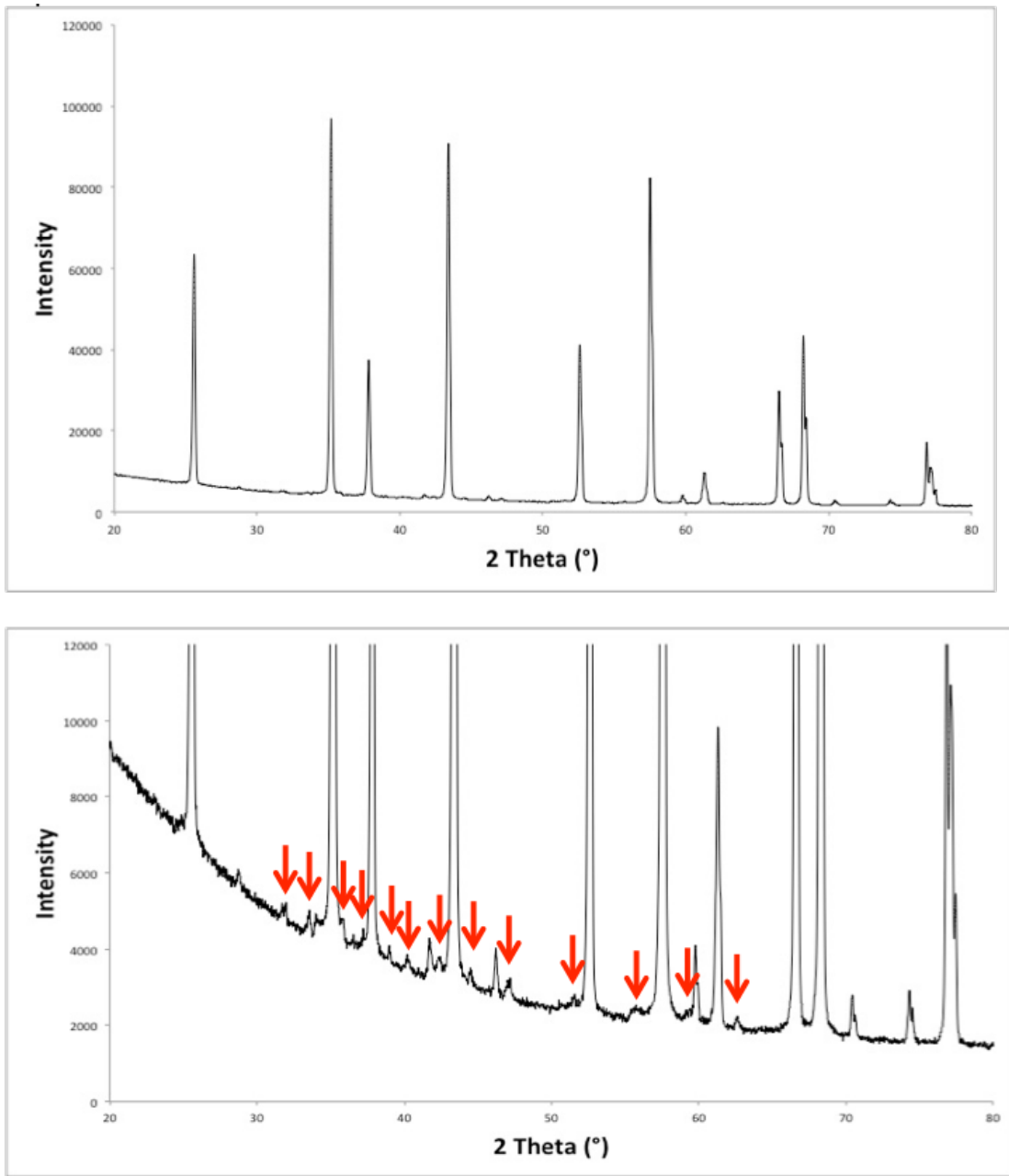


**Figure 5.9.** XRD pattern of a sample with 1060 ppm Na<sub>2</sub>O, 82 ppm SiO<sub>2</sub>, and 380 ppm MgO after sintering at 1525°C for 5 h. The red arrows indicate the peaks that can be assigned to  $\beta$ -Al<sub>2</sub>O<sub>3</sub>. The other peaks can be assigned to  $\alpha$ -Al<sub>2</sub>O<sub>3</sub>.

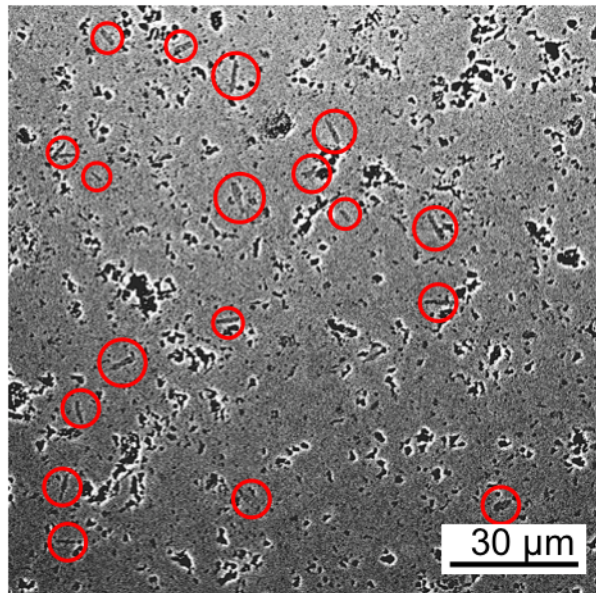


**Figure 5.10.** Micrograph showing  $\beta$ - $\text{Al}_2\text{O}_3$  grains (red circles) in an ultra high purity powder sample with 502 ppm  $\text{Na}_2\text{O}$ , 2 ppm  $\text{MgO}$ , and 11 ppm  $\text{SiO}_2$  after sintering at 1525°C for 0 h.

# Chapter 6 |

# A Critique of the Master Sintering Curve Analysis of Sintering Processes

## 6.1 Introduction

The master sintering curve (MSC) approach was developed by Su and Johnson [?] to generalize densification behavior of a sintering powder with a single curve for the entire sintering time/temperature profile. The MSC approach is based on a combined-stage sintering model developed by Hansen et al, [95] given as:

$$\frac{1}{\rho} \frac{d\rho}{dt} = \frac{3\gamma\Omega}{k_B T} \left( \frac{\delta D_b \Gamma_b}{G^4} + \frac{D_v \Gamma_v}{G^3} \right) \quad (6.1)$$

where  $\rho$  is relative density of the powder compact,  $d\rho/dt$  is densification rate,  $\gamma$  is surface energy,  $\Omega$  is molar volume,  $k_B$  is Boltzmann's constant,  $T$  is absolute temperature,  $G$  is grain size,  $D$  is diffusion coefficient,  $\delta$  is grain boundary thickness, and  $\Gamma$  is a geometric scaling factor. The subscripts  $b$  and  $v$  represent grain boundary and volume diffusion mechanisms, respectively. The MSC was originally derived to simplify the combined-stage sintering model (Eq. 6.1) to account for only a single diffusion mechanism, and by considering diffusion as thermally-activated with an activation energy  $Q$ . The resulting equation is given as:

$$\frac{1}{\rho} \frac{d\rho}{dt} = \frac{3\gamma\Omega}{k_B T} \left( \frac{D\Gamma}{G^n} \right) \quad (6.2)$$

where

$$D = D_0 e^{-Q/RT} \quad (6.3)$$

and  $R$  is the ideal gas constant. Eq. 6.2 is re-written to collect microstructural parameters on the left hand side and temperature dependent parameters on the right hand side:

$$\frac{k_B G^n}{3\rho\gamma\Omega\Gamma D_0} \frac{d\rho}{dt} = \frac{1}{T} \exp\left(-\frac{Q}{RT}\right) = \frac{d\Theta}{dt} \quad (6.4)$$

Eq. 4 can be integrated to give:

$$\frac{k_B}{\gamma\Omega\Gamma D_0} \int_{\rho_0}^{\rho} \frac{(G(\rho))^n}{3\rho\Gamma(\rho)} d\rho = \int_0^t \frac{1}{T} \exp\left(-\frac{Q}{RT}\right) dt = \Theta \quad (6.5)$$

Equation 6.5 describes the sintering behavior for an arbitrary time-temperature profile, and the integral over this profile with respect to time is termed the work of sintering  $\Theta$ . The MSC is obtained by plotting  $\rho$  versus  $\Theta$ . The left hand side of Eq. 6.4 is not solved, because many of the parameters are unknown. However, as long as these parameters are independent of time and temperature, data plotted in this way will collapse into a single continuous curve for a single value of  $Q$ . It is interesting to note that the MSC analysis is independent of the sintering mechanism and, as a generalized model, was applied to other thermally activated process such as grain growth [96] and binder decomposition [97, 98].

In practice,  $Q$  is a fitting parameter for which the best-fit MSC is obtained over a range of heating rates by determining the minimum mean residual. Assuming arbitrary values for  $Q$  in Eq. 6.5, the mean residual square is calculated by [99]

$$\text{Mean residual square} = \sqrt{\frac{1}{\rho_s - \rho_0} \int_{\rho_0}^{\rho_s} \frac{\sum_{i=1}^N \left( \frac{\Theta_i}{\Theta_{avg}} - 1 \right)^2}{N} d\rho} \quad (6.6)$$

where  $N$  is the number of experimental data points gathered at a series of heating rates and a sintered density  $\rho_s$ , and  $Q_{avg}$  is the average of all  $Q_i$  over  $N$ . The  $Q$  value that yields the minimum mean residual square is the  $Q$  value at which the MSC trajectories obtained from the densification curves at different heating rates yield the best fit and converge onto a single curve. Because of the mechanistic nature of the model, the  $Q$  parameter is usually referred to in the literature as the

'activation energy' for sintering.

MSC analysis has been applied to ceramic powders formed and densified by a variety of techniques. For high purity alumina, the reported  $Q$  values vary drastically, as seen in Table 6.1. In Su and Johnson's original work [100],  $Q$  values of 440 and 488 kJ/mol were determined by minimum mean residuals and isostrain analysis, respectively, for an ultrafine, ultrahigh purity alumina (AKP-50, Sumitomo Chemical America, Inc.), showing that the activation energy obtained from minimum mean residuals is in close agreement with the activation energies determined by conventionally used methods. Using the same powder, Tatami et al. [101] determined a  $Q$  of 555 kJ/mol, and when the powder was doped with 2000 ppm MgO, a  $Q$  of 880 kJ/mol was determined. Pouchly et al. [102] estimated the  $Q$  of two different ultrahigh purity alumina powder graded (Taimicron TM-DAR, Taimei Chemicals and RC-HP DBM, Reynolds Chemicals) to be 770 and 640 kJ/mol, respectively, and attributed the difference in  $Q$  to the difference in particle size of 110 nm and 240 nm, respectively. Aminzare et al. [103], reported  $Q$  values of 700 and 605 kJ/mol for alumina (Taimicron TM-DAR, Taimai Chemicals) samples prepared by dry pressing and pressure filtration, respectively. Using the same alumina powder grade (Taimicron TM-DAR, Taimai Chemicals), Guillou and Langer [104] reported a  $Q$  of 290 kJ/mol for  $\text{Al}_2\text{O}_3$  densified by spark plasma sintering (SPS). They attributed the lower  $Q$  value to the effect of the high heating rates of 35  $^{\circ}\text{C}/\text{min}$  during SPS.  $Q$  values of up to 1064 kJ/mol were reported by Shao et al. [105] for granulated and dry pressed alumina powder (350 nm, 99.9%, Dalian Luming Nanometer Material Ltd.). They explained the higher  $Q$  values as an effect of slower heating rates (0.5 and 5  $^{\circ}\text{C}/\text{min}$ ) on densification.

The effect of heating rate on densification was explained by Harmer and Brook [106] as due to the relative time the material is heated under conditions favoring surface and grain boundary diffusion. They reasoned that a slow heating process favors surface diffusion and particle coarsening because surface diffusion usually has a lower activation energy than densifying mechanisms like grain and volume diffusion. Samples heated at slow rates spend relatively longer times at lower temperatures and, therefore, experience more particle coarsening prior to reaching the temperatures where densification occurs. Thus, the sintering driving force from surface area is higher during the densification stage when ceramics are fired at higher heating rates since these samples do not undergo as much coarsening prior

to densification. In MSC analysis, these relative changes in mechanism result in lower  $Q$  values at faster heating rates. However, it is assumed in the MSC analysis that sintering occurs by a single mechanism for the heating conditions used to collect densification data. Since data for MSC analysis is performed by heating samples at different heating rates, the contributions from surface diffusion and grain boundary diffusion vary, and it is questionable if the  $Q$  values obtained can be used for mechanistic interpretations. Furthermore, it is not apparent why there is so much variability of the reported  $Q$  values.

In this chapter, we investigate how forming techniques and powder chemistry affect the  $Q$  parameter and the shape of the MSC for a commercial specialty alumina powder. We explore how forming process-induced differences in relative green density, microstructural homogeneity and shrinkage anisotropy affect the value of  $Q$ . We also investigate how the assumption of a constant microstructure (i.e., grain size) at high density affects the MSC fit and  $Q$  value. A series of Na<sub>2</sub>O-doped samples were studied to determine how changes in densification mechanism affect the value of  $Q$ . Based on these experiments, we discuss the limits and accuracy of the MSC approach and then determine how MSC can be used in a constructive, practical way to predict the sintering of a specific powder.

## 6.2 Experimental Procedure

To examine the impact of the forming technique on the MSC, we prepared undoped alumina (CT3000LS-SG, Almatis, Inc., Leetsdale, PA) samples by dry pressing, slip casting and tape casting. The powder was a Bayer process alumina (99.8%) with an average particle diameter of 0.3  $\mu\text{m}$ . Two sets of samples were prepared by uniaxial dry pressing. For one set, the as-received powder was sieved to -106  $\mu\text{m}$  and uniaxially dry pressed at 30 MPa. The powder handling for the second set was designed to produce a soft, granulated powder by dispersing it in ethanol with 5 wt.% polyethylene glycol (PEG 600 (?), Alfa Aesar, Ward Hill, MA, USA). After ball milling for 24 h, the dried powder was sieved to -106  $\mu\text{m}$  and samples were lightly pressed at 30 MPa. Both sample types were isopressed at 200 MPa after removing the organic processing aids by heating at 600°C for 12 h in air.

For tape casting, a slurry was prepared by ball milling 68.14 wt.% alumina powder with 15.31 wt.% xylene (ACS Reagent grade, Avantor Performance Materials,

Inc., Center Valley, PA, USA), 15.31 wt.% ethanol (200 proof), and 1.24 wt.% blown menhaden fish oil (Grade Z-3, Tape Casting Warehouse, Morrisville, PA, USA). After 24 h, 3.09 wt.% polyvinyl butyral (PVB B-98, Tape Casting Warehouse, Morrisville, PA, USA), 1.55 wt.% polyalkylene glycol (PAG, UCON50HB2000, Tape Casting Warehouse, Morrisville, PA, USA) and 1.55 wt.% butyl benzyl phthalate (BBP S-160, Tape Casting Warehouse, Morrisville, PA, USA) were added and the mixture was ball milled for another 24 h, before 1 drop of cyclohexane (99+%, Alfa Aesar, Ward Hill, MA, USA) per 20 g of alumina powder was added and the slurry was stirred for an additional 45 min. The slurry was tape cast on a silicone-coated Mylar<sup>TM</sup> carrier tape using a doctor blade gap height of 305  $\mu\text{m}$ . After drying, the tape was cut, stacked, uniaxially pressed at 70°C for 10 min at minimal pressure to tack the layers together, and then isostatically laminated at 74°C and 20 MPa for 30 min.

For non-aqueous slip casting, 65.3 wt.% powder was dispersed in Xylene with 2 wt.% Menhaden fish oil, ball milled for 24 h, and slip cast. For aqueous slip casting 76 wt.% alumina powder was dispersed in deionized water with 3 wt.% Darvan C (R. T. Vanderbilt Company, Inc., Norwalk, CT, USA). The pH of the Darvan and water mixture was adjusted to 11 using 5 M NH<sub>4</sub>OH before the alumina powder was added. The slurry was ball milled for 24 h and then slip cast. In both cases the mold consisted of a PVC tube (20 mm diameter) on a plaster of Paris plate.

The polymer processing aids were burned out of all samples by heating at 600°C for 12 h in air. All samples were cold isostatically pressed at 200 MPa (CIP, Autoclave Engineers, Erie, PA). The samples were subsequently cut and ground into 3 x 3 x 15 mm<sup>3</sup> bars for dilatometry studies. The long axis of the dilatometry samples corresponds to the pressing direction during uniaxial compaction, the casting direction during slip casting, and the casting direction for tape cast samples. The bars were heated to 1525°C or 1600°C at 5, 10, and 20°C/min in a thermomechanical analyzer (TMA; Linseis PT1600, Robbinsville, NJ) to record the linear shrinkage of the samples. The thermal expansion contribution of the samples to the dilatometry curves was subtracted from the dimensions measured in-situ using the cooling curves of the samples measured in the TMA.

To examine how changes in chemistry affect the MSC analysis, we studied a series of dry pressed Na<sub>2</sub>O-doped aluminas. The alumina powder was doped with up to 1000 ppm Na<sub>2</sub>O using sodium acetate (NaC<sub>2</sub>H<sub>3</sub>O<sub>2</sub>\*3H<sub>2</sub>O, ACS grade, BDH,

West Chester, PA). The detailed doping procedure is reported in chapter 2.

## 6.3 Results and Discussion

### 6.3.1 The effect of forming on $Q$

During initial studies, we observed different degrees of anisotropic shrinkage as a function of the forming method. For example, the dilatometry curves of the non-aqueous slip cast samples during heating to 1525°C at 5, 10, and 20°C/min are shown in Figure 6.1. The shrinkage was measured in the z-direction, i.e., the direction parallel to the capillary (i.e. shear) force of the plaster of Paris mold during slip casting, and in the x/y-direction, perpendicular to the capillary force. Anisotropic shrinkage was observed for all heating rates. Samples heated at 5°C/min have a higher shrinkage in the z-direction than in the x/y-direction throughout the entire sintering process, whereas samples heated at 10 and 20°C/min show slightly more shrinkage in the x/y-direction in the initial stage of densification followed by a crossover in the shrinkage and much more shrinkage in the z-direction at higher densities. The anisotropic shrinkage was quantified with a shrinkage anisotropy factor  $k$ , which is the ratio of the shrinkage in the z-direction to the shrinkage in x/y-direction. Figure 6.2 shows how  $k$  changes as a function of relative density and heating rate for the non-aqueous slip cast samples heated at different heating rates during densification. Interestingly, the shrinkage anisotropy factor changes significantly as a function of heating rate during densification and there is much less change in  $k$  at the slowest heating rate. Relative density was calculated using the shrinkage anisotropy factor and is plotted as a function of temperature in Figure 6.3. The mean residuals were calculated as a function of  $Q$  (Eq. 6.6), and the minimum is at  $Q = 550$  kJ/mol (Figure 4.4). The relatively sharp minimum provides evidence that a single MSC curve is a good fit for the measured TMA data.

When shrinkage in the z-direction is assumed to represent isotropic shrinkage (i.e.  $k=1$ ), then  $Q$  increases to 625 kJ/mol. Figure 6.5 compares the MSCs obtained when the shrinkage anisotropy was accounted for (550 kJ/mol) or by assuming isotropic shrinkage (no correction for anisotropy). This example demonstrates the importance of determining whether the sample shrinks anisotropically during the

density measurements used to construct the MSC, and the need to correct for anisotropic shrinkage to determine an accurate value  $Q$  and MSC. Note that the curves at all 3 heating rates coincide.

Figure 6.6 shows the corresponding MSC curves of samples formed by various techniques and heated to 1525°C. The measurements were corrected for shrinkage anisotropy as described above. The total shrinkage anisotropy was  $\sim 0.75$  for slip cast and tape cast samples, and  $\sim 0.92$  for dry pressed samples. It is clear that  $Q$  changes as a function of forming technique, which is, in part, due to different green densities. The sample prepared by non-aqueous slip casting has a green density of 59% and the lowest  $Q$  (550 kJ/mol), followed by the sample prepared by aqueous slip casting with a green density of 58% and a  $Q$  of 650 kJ/mol. The samples prepared by dry pressing (no PEG) and tape casting have green densities of 57% and 55%, respectively, and both samples have a  $Q$  of 730 kJ/mol. The dry pressed sample with 5 wt.% PEG has a green density of 55% and the highest activation energy with 810 kJ/mol. It can thus be observed that  $Q$  decreases as the green density increases and that the shape and position of the MSC changes as a function of forming technique (Figure 6.6). Aminzare et al. [103] also observed that  $Q$  is sensitive to the forming technique and concluded that samples prepared by pressure filtration have a lower  $Q$  than dry pressed samples as a result of better sample homogeneity as evidenced by the higher green density. As shown in this work, the effect of green density on  $Q$  is complicated. For example, the samples prepared by tape casting and dry pressing with 5 wt.% PEG have the same green density of 55%, but different  $Q$  values of 730 kJ/mol and 810 kJ/mol, respectively, and different MSC shapes. This suggests that other sample characteristics, in addition to green density, influence  $Q$ , such as pore size, pore size distribution, and particle/pore orientation.

### 6.3.2 MSC at high densities

The final densities used in the MSC analysis of the samples discussed above are  $\leq 90\%$ . Above 90% density we observed that the MSC curves for different heating rates diverge and thus which dramatically influences the value of  $Q$ . Figure 6.7a shows the densification curves of dry pressed samples sintered to  $>95\%$  density when heated to 1600°C at different heating rates. The minimum mean residual

analysis yielded  $Q = 700$  kJ/mol (Figure 6.7b) and Figure 6.7c shows the resulting MSC. It can be seen that  $Q = 700$  kJ/mol gives a good fit at low densities, but the trajectories begin to diverge at densities  $>90\%$  (see Fig 6.7c insert).

To account for the effect of bulk density on densification we determined the activation energy at some relative densities by plotting  $\ln(-T \frac{d\rho}{dt})$  vs.  $1/T$  and determining the slopes of the resulting linear curves of the isodensities. Figure 6.8 shows the development of the apparent activation energy obtained from iso-density analysis,  $Q_{iso}$ , and it can be seen that  $Q_{iso}$  is  $\sim 700$  kJ/mol and increases slightly with increasing relative density. At densities  $>85\%$   $Q_{iso}$  increases somewhat more rapidly, and at densities  $>95\%$   $Q_{iso}$  increases drastically to  $>1800$  kJ/mol. This change in  $Q_{iso}$  explains the divergence of the MSC trajectories obtained from the different heating rates using  $Q_{MSC} = 700$  kJ/mol.

At densities  $<90\%$  the activation energy obtained from the minimum mean residuals  $Q_{MSC}$ , which is used to obtain the MSC, is reasonably close to the activation energies obtained from the iso-density analysis,  $Q_{iso}$ , resulting in a good fit at all heating rates. However, at densities  $>90\%$  where we observe divergence in the MSCs, the values of  $Q_{iso}$  are  $>100$  kJ/mol greater than the  $Q_{MSC}$  value used to construct the MSC. Although the idea of variable activation energy is understandable, it is not physically realistic to consider that the activation energy for sintering is intrinsically a function of  $\rho$ . It is more likely that this increase in  $Q_{iso}$  and the divergence of the MSC at high densities is caused by microstructural or mechanistic changes that are not accounted for in the MSC model.

### 6.3.3 Quantification of the MSC shape

A way to account for microstructural changes is analyzing the shape of the MSC, since it is determined by the evolution of the microstructural parameters in the left hand side of Eq. 6.5. Microstructural evolution can be described quantitatively by:

$$C = \frac{k_B G^n}{3\gamma\Omega\Gamma D_0} \quad (6.7)$$

By rearranging Eq. 6.4  $C$  can be determined as a function of relative density:

$$C = \rho \frac{d\Theta}{d\rho} \quad (6.8)$$

In Figure 6.9 it can be seen that  $C$  increases by more than 5 orders of magnitude between 57% and 98% relative density. The increase in  $C$  is partially due to the 8-fold increase in grain size from 0.3 to 2.4  $\mu\text{m}$  during sintering of the sample to 98% relative density. Assuming that grain boundary diffusion controls densification ( $n=4$ ), the coarsening of the microstructures accounts for an increase in  $C$  of  $\sim 3.5$  orders of magnitude. The remaining  $\sim 2$  orders of magnitude increase in  $C$  are most likely due to an increase in the geometric factor  $\Gamma$ , since it is a function of relative density and the only parameter that is expected to change considerably with temperature. Note that the obtained trajectories for  $C$  also diverge above 90% relative density, similar to the MSCs.

#### 6.3.4 Influence of powder chemistry

Figure 6.10 shows the MSCs of  $\text{Na}_2\text{O}$ -doped samples formed by non-aqueous slip casting. It can be seen that  $Q$  changes as a function of  $\text{Na}_2\text{O}$  concentration and increases from 550 kJ/mol for samples with no  $\text{Na}_2\text{O}$  dopant to 700 and 730 kJ/mol for samples doped with 250 and 500 ppm  $\text{Na}_2\text{O}$ , respectively.  $Q$  decreases to 690 kJ/mol when the concentration is further increased to 1000 ppm  $\text{Na}_2\text{O}$ . The position of the MSC changes as a function of  $\text{Na}_2\text{O}$  concentration as well, but the effect of  $\text{Na}_2\text{O}$  concentration on the MSC is complicated.

#### 6.3.5 Limitations of the MSC analysis

Anisotropic shrinkage is commonly observed in slip cast parts since the capillary force and settling cause particles in the slurry to align during slip casting. It should be noted that the degree of shrinkage anisotropy strongly depends on the particle morphology and forming technique (i.e. magnitude of shear force exerted on the particles and ease of reorientation). For samples that were prepared by colloidal forming techniques, such as slip casting and tape casting, the degree anisotropic shrinkage has to be taken into account during the MSC analysis, otherwise the densities calculated from the dilatometry data alone are inaccurate and thus the calculated value of  $Q$  and the shape of the MSC are incorrect. Likewise, samples formed by uniaxial pressing are often anisotropic but not to the same degree as slurry processed ceramics.

The above results show that a variety of factors such as forming technique and

powder chemistry affect the value of  $Q$  and the shape of the MSC in a complicated way, and the reason for this complicated relation lies in the assumption in MSC analysis that sintering is influenced by only one single mechanism. Making this assumption allows MSC analysis to assign an activation energy for sintering that corresponds to this specific sintering mechanism. If this assumption held true, variations in forming technique or chemistry could be analyzed using the MSC approach and using  $Q$  as an indicator for how the sinterability of a powder changes as a function of powder chemistry and forming technique. However, sintering is typically divided into different stages, all of which are governed by different sintering mechanisms. When multiple mechanisms are involved, each mechanism can be affected differently by such changes and  $Q$  loses its physical meaning as an activation energy for a specific sintering mechanism. As a result,  $Q$  appears to be a function of relative density (Figure 6.8) and the changes in  $Q$  and MSC shape as a function of powder chemistry and forming technique are complicated.

For example, we know that initial pore size, pore size distribution, and pore/-particle orientation in a green body are highly dependent on the forming technique. Changes in these parameters affect different sintering stages in different ways. For example, during initial stage sintering the sinter undergoes a particle rearrangement process that is driven by capillary forces and therefore highly sensitive to the aforementioned parameters. During final stage sintering the concentration of large pores that can only slowly be eliminated is determined by the forming technique. Mechanistic changes as such can affect  $Q$  in different ways.

Similarly, powder chemistry affects initial stage sintering and intermediate stage sintering in different ways. In previous chapters, it was observed that the onset temperature of sintering increases with higher  $\text{Na}_2\text{O}$  concentration, which has the effect of increasing  $Q$ . The further development of densification was shown to depend heavily on additional factors. For example, samples with  $\text{Na}_2\text{O}/\text{SiO}_2$  ratios  $\sim 1.0$  densify faster during intermediate stage sintering than samples with  $\text{Na}_2\text{O}/\text{SiO}_2$  ratios  $\sim 0.1$  for the same  $\text{SiO}_2$  concentration because  $\text{Na}_2\text{O}$  decreases the viscosity of the siliceous liquid grain boundary phase, and, therefore, enhances diffusion, which would decrease  $Q$ . This demonstrates that powder chemistry influences fundamental sintering mechanisms at different sintering stages and in different ways.

Since the processes and mechanisms of all sintering stages are lumped into one

$Q$  value during MSC analysis, forming technique and powder chemistry may affect the value of  $Q$  and the shape of the MSC, but the changes in sintering behavior and mechanisms cannot be sufficiently described using  $Q$  and the MSC. Therefore, the MSC approach is judged to be insufficient to evaluate forming and powder chemistry effects on sintering. It is recommended that  $Q$  values obtained by MSC analysis for different powder grades (i.e. chemistries, forming techniques, particle size, etc.) should not be compared or used to draw conclusions about sintering mechanisms.

### 6.3.6 Practical use of the MSC analysis

Even though MSC analysis is insufficient to analyze fundamental differences in sintering behavior due to differences in powder chemistry and forming technique, choosing an appropriate  $Q$  value converges the trajectories of samples obtained from different heating rates onto one MSC, and this  $Q$  value and the obtained MSC can be used to predict densification. As explained in the literature [107, 108], the  $Q$  value obtained is an apparent activation energy for the entire sintering process of a sinter and accounts for densification (regardless of mechanism), the retardation of densification due to grain growth, surface diffusion in the early sintering stages, and other processes that potentially influence densification. Consequently,  $Q$  is a fitting parameter that is composed of a variety of factors that influence densification, including the activation energies for sintering of all involved mechanisms.

One of the practical objectives of MSC analysis is to predict the sintered density of samples prepared from a given powder for an arbitrary time/temperature condition. The MSC data provided above and Eq. 6.5 can be used to construct equivalent time/temperature diagrams to predict the density of samples for known heating conditions. Fig 6.11 is an example of the equivalent time/temperature conditions leading to equivalent densities for non-aqueous processed powder dry pressed samples heated at 10°C/min. The contours shown in Figure 6.11 indicate the equivalent relationships between particular time/temperature treatments and relative densities of 80, 85, 90, and 95%. For example, a relative density of 85% is reached after heating a dry pressed sample at 10°C/min to 1460°C with no hold time. The same density is reached after heating a dry pressed sample from the same powder at 10°C/min to 1400°C and holding for 29 min. It should be noted that

the predicted MSC response for >90% sintered density has some inaccuracy due to the discrepancies we noted above for MSC data analysis at >90% density. Despite earlier reservations and limitations, the predictions for equivalent time/temperature conditions leading to 95% density are insightful and, at least, give a semiquantitative measure of the effect of time and temperature on sintering.

## 6.4 Summary

MSC analysis results in two pieces of information; a  $Q$  value and the MSC curve itself.  $Q$  should not be interpreted as the activation energy for sintering, since multiple mechanisms contribute to its value and processing history and powder chemistry can drastically affect the  $Q$  value and the shape of the MSC curve. Therefore, comparing  $Q$  between different chemistries is not an appropriate means to interpret fundamental, mechanistic changes in sintering behavior.

It is evident that the MSC is only useful for characterizing the sintering behavior of the specific ceramic powder studied. A number of factors need to be accounted for to obtain accurate  $Q$  values and MSCs including sample shrinkage anisotropy, and limiting the density range to < 90% density to avoid microstructural changes that are not accounted for in the MSC analysis. With more accurate  $Q$  values the MSC approach is a useful tool and "a practical approach to sintering" as originally proposed by Su and Johnson, but is not sufficient to explain fundamental changes in sintering behavior, or to determine the "activation energy" for sintering.

**Table 6.1.**  $Q$  values obtained by MSC analysis for different alumina powders.

Alumina grade	Forming technique	Heat rates (°/min)	$Q$ (kJ/mol)	Ref
AKP-50 Sumitomo Chemicals	CIP (270 MPa)	60 to 750°C 8-45 to 1500°C	440	[100]
AKP-50 Sumitomo Chemicals	Uniaxial pressing (50 MPa) CIP (200 MPa)	3-20 to 1400°C	555	[101]
AKP-50 + 2000 ppm MgO Sumitomo Chemicals	Uniaxial pressing (50 MPa) CIP (200 MPa)	3-20 to 1400°C	880	[101]
Taimicron TM-DAR Taimei Chemicals	CIP (300 MPa)	2-20 to 1500°C	770	[102]
RC-HP DBM Reynolds Chemicals	CIP (300 MPa)	2-20 to 1500°C	640	[102]
Taimicron TM-DAR Taimei Chemicals	Uniaxial pressing (50 MPa) CIP (200 MPa)	2-25 to 1400°C	700	[103]
Taimicron TM-DAR Taimei Chemicals	Pressure filtration (40 MPa)	2-25 to 1400°C	605	[103]
Taimicron TM-DAR Taimei Chemicals	SPS (50 MPa)	35-150 to 1200°C	290	[104]
99.9%, Dalian Luming Nanometer Materials	Uniaxial pressing (80 MPa) CIP (250 MPa)	0.5-5 to 1640°C	1064	[105]

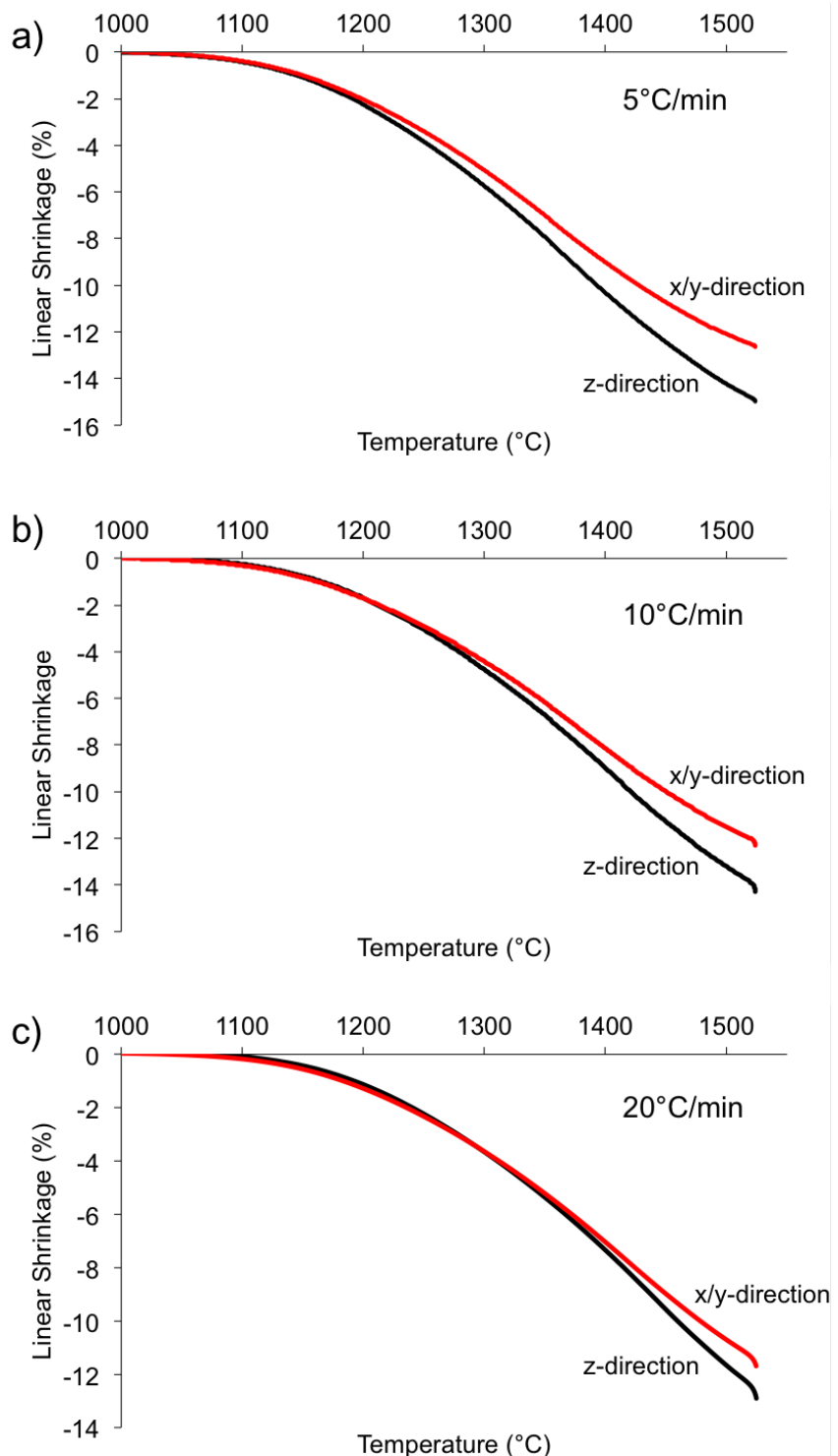


**Figure 6.1.** Dilatometry curves of non-aqueous slip cast CT3000LS-SG samples heated at a) 5°C/min, b) 10°C/min, and c) 20°C/min to 1525°C measured parallel to (z-direction) and perpendicular to (x/y-direction) the capillary force acting during slip casting.

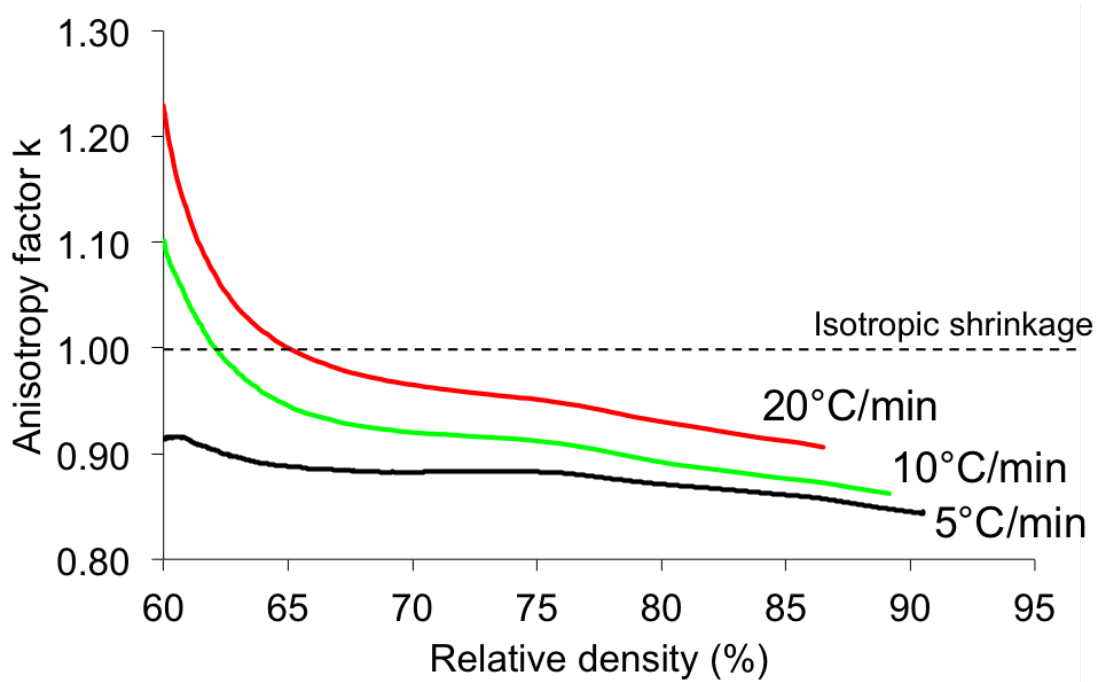


**Figure 6.2.** Development of the shrinkage anisotropy factor for shrinkage,  $k$ , during densification of non-aqueous slip cast samples as a function of relative density for CT3000LS-SG samples heated at different rates.

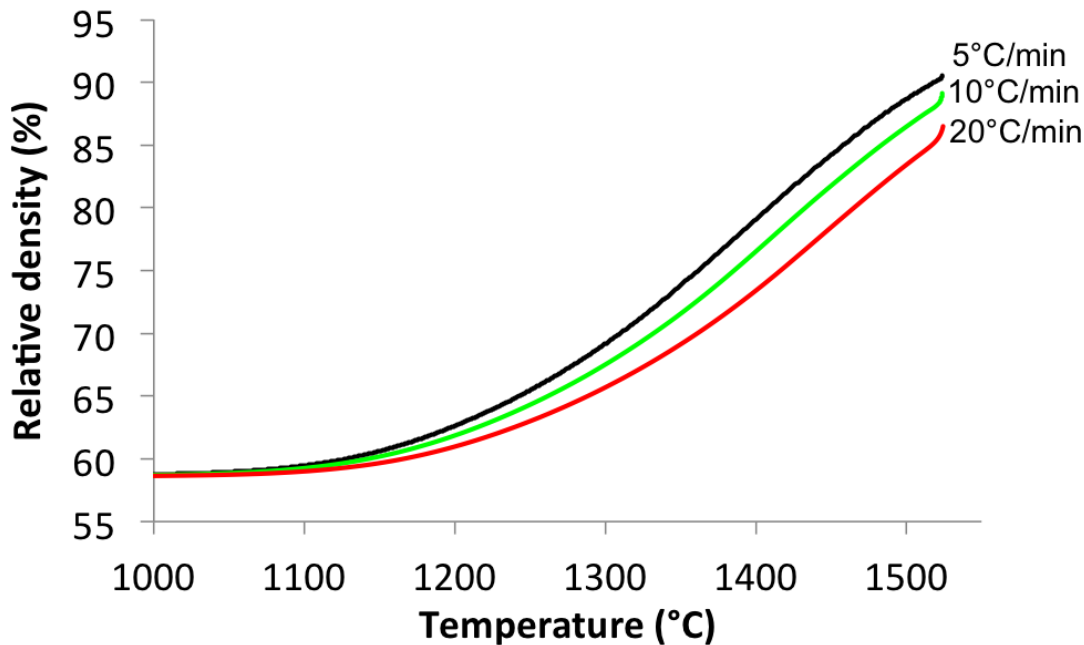


**Figure 6.3.** Development of the relative density corrected for shrinkage anisotropy as a function of temperature for non-aqueous slip cast CT3000LS-SG samples heated at different rates.

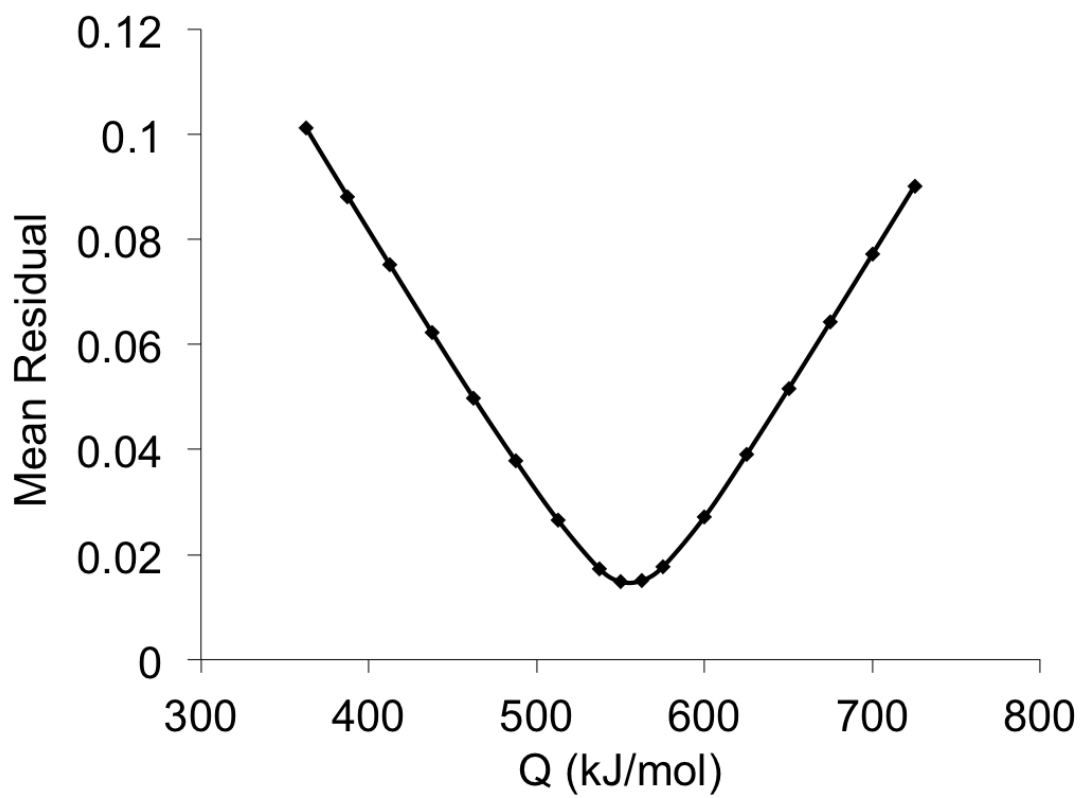


**Figure 6.4.** Mean residuals of the MSC curves assuming different values for  $Q$  for non-aqueous slip cast CT3000LS-SG samples.

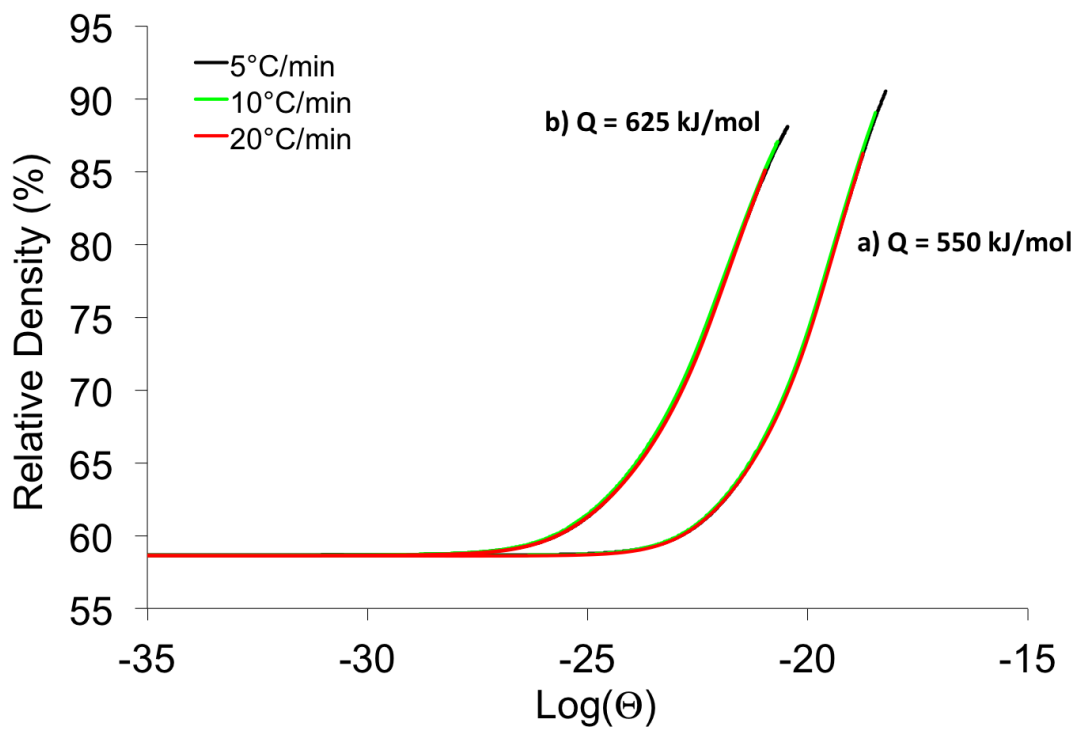


**Figure 6.5.** MSC curves of CT3000LS-SG samples prepared by non-aqueous slip casting using a) the  $Q$ -value obtained by accounting for shrinkage anisotropy ( $Q=550 \text{ kJ/mol}$ ) and b) using  $Q$ -value when shrinkage anisotropy was uncorrected for ( $Q = 625 \text{ kJ/mol}$ ).

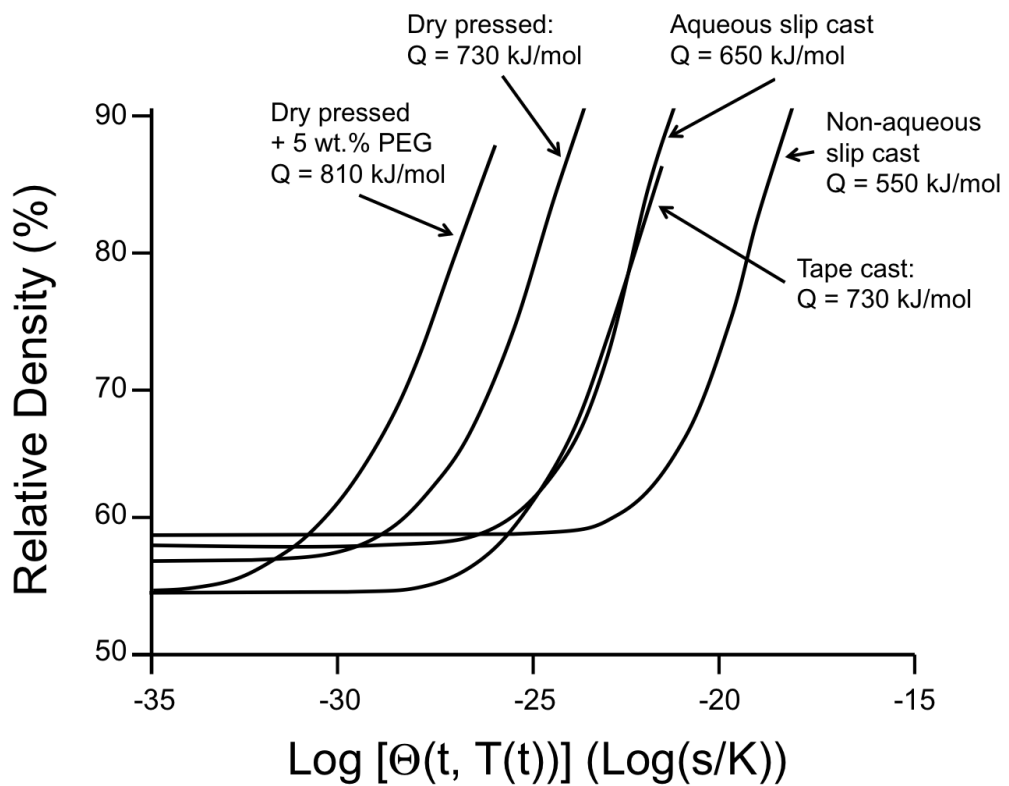


**Figure 6.6.** MSC curves and  $Q$ -values of CT3000LS-SG samples obtained from the minimum mean residuals for samples prepared by different forming techniques and accounting for shrinkage anisotropy.

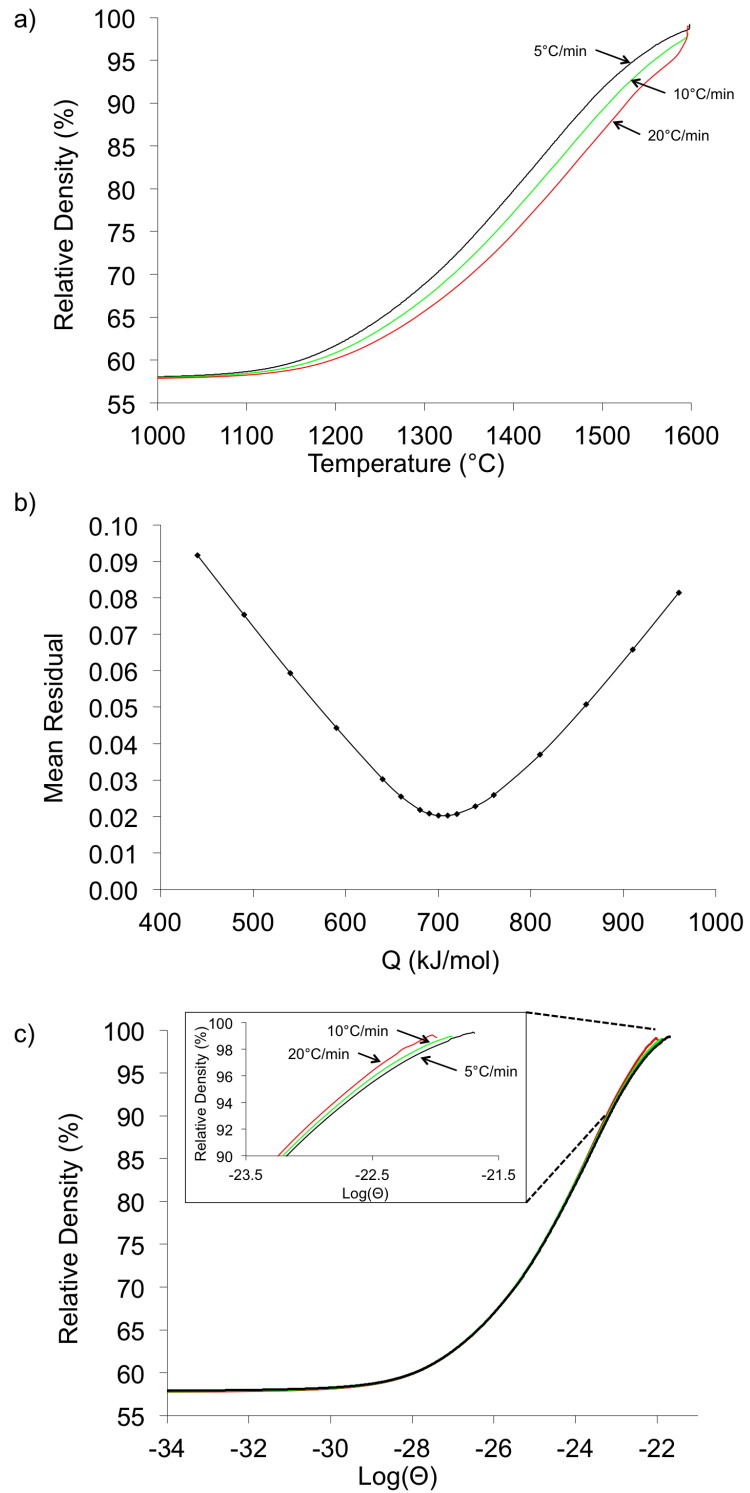


**Figure 6.7.** Densification of dry pressed CT3000LS-SG samples at different heating rates, b) mean residuals as a function of  $Q$ , and c) MSC for  $Q = 700$  kJ/mol obtained from the minimum mean residuals, showing divergence at densities >90%.

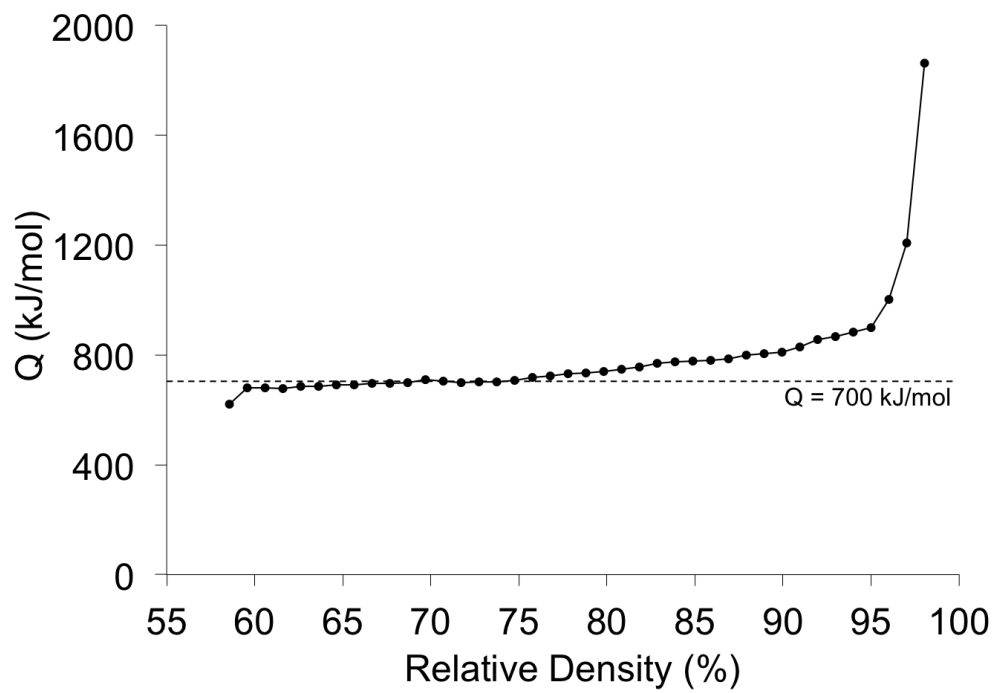


**Figure 6.8.**  $Q$ -values for dry pressed CT3000LS-SG samples as a function of relative density obtained from iso-density analysis.

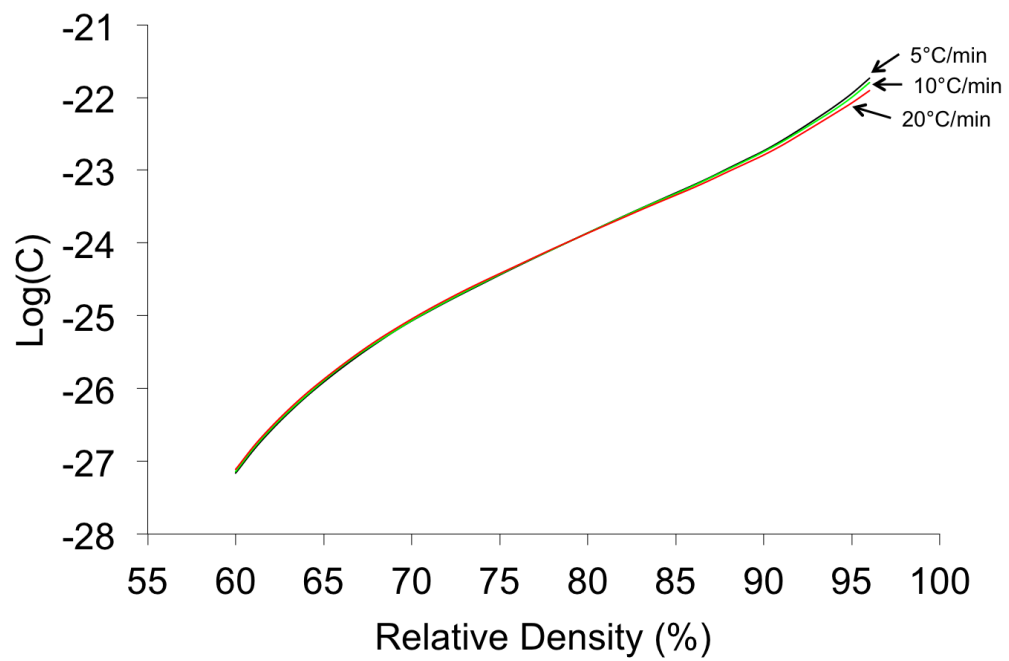


**Figure 6.9.** Development of the microstructural parameters, summarized in the  $C$  parameter, as a function of relative density for a dry pressed CT3000LS-SG sample.

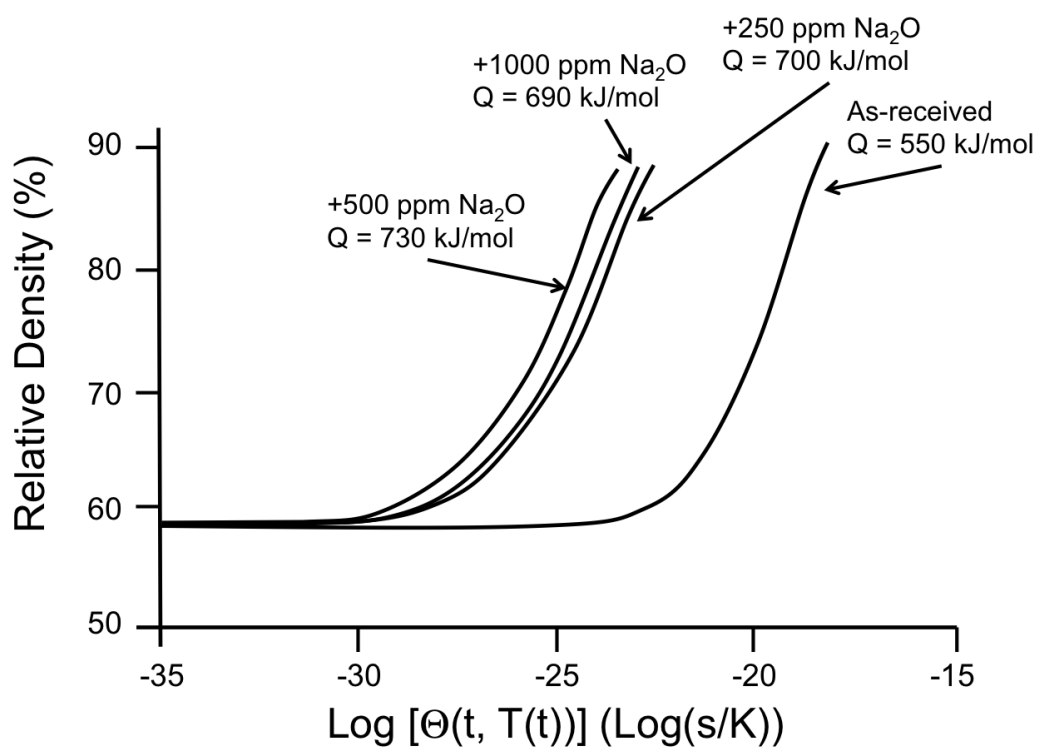


**Figure 6.10.** MSCs and  $Q$ -values for CT3000LS-SG samples prepared by non-aqueous slip casting with different  $\text{Na}_2\text{O}$  concentrations.

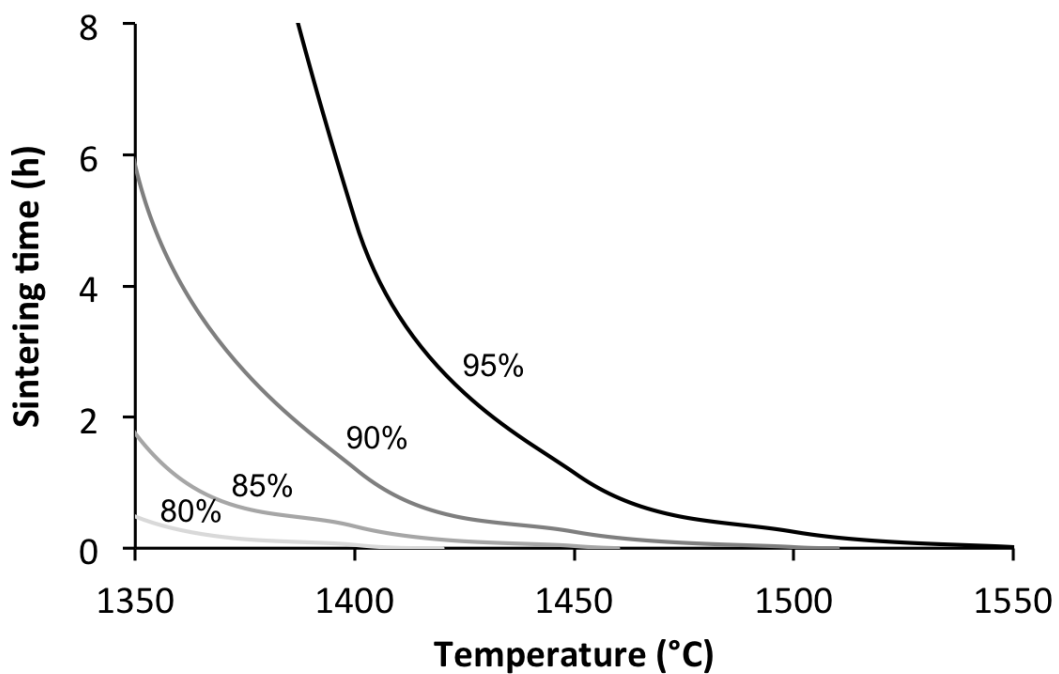


**Figure 6.11.** Equivalent time/temperature diagram for CT3000LS-SG samples prepared by non-aqueous slip casting heated at 10°C/min. The contours may be used to predict heat treatments requirements to achieve a desired density.

# **Chapter 7 |**

# **Summary and Future Work**

## **7.1 Introduction**

When in the Course of human events, it becomes necessary for one people to dissolve the political bands which have connected them with another, and to assume among the powers of the earth, the separate and equal station to which the Laws of Nature and of Nature's God entitle them, a decent respect to the opinions of mankind requires that they should declare the causes which impel them to the separation.

## **7.2 More Declaration**

We hold these truths to be self-evident, that all men are created equal, that they are endowed by their Creator with certain unalienable Rights, that among these are Life, Liberty and the pursuit of Happiness. —That to secure these rights, Governments are instituted among Men, deriving their just powers from the consent of the governed, —That whenever any Form of Government becomes destructive of these ends, it is the Right of the People to alter or to abolish it, and to institute new Government, laying its foundation on such principles and organizing its powers in such form, as to them shall seem most likely to effect their Safety and Happiness. Prudence, indeed, will dictate that Governments long established should not be changed for light and transient causes; and accordingly all experience hath shewn, that mankind are more disposed to suffer, while evils are sufferable, than to right themselves by abolishing the forms to which they are accustomed. But when a long train of abuses and usurpations, pursuing invariably the same Object evinces

a design to reduce them under absolute Despotism, it is their right, it is their duty, to throw off such Government, and to provide new Guards for their future security. —Such has been the patient sufferance of these Colonies; and such is now the necessity which constrains them to alter their former Systems of Government. The history of the present King of Great Britain [George III] is a history of repeated injuries and usurpations, all having in direct object the establishment of an absolute Tyranny over these States. To prove this, let Facts be submitted to a candid world.

# Bibliography

- [1] GAVRILOV, K. L., S. J. BENNISON, K. R. MIKESKA, J. M. CHABALA, and R. LEVI-SETTI (1999) “Silica and magnesia dopant distributions in alumina by high-resolution scanning secondary ion mass spectrometry,” *Journal of the American Ceramic Society*, **82**(4), pp. 1001–1008.
- [2] BAE, I.-J. and S. BAIK (1997) “Abnormal grain growth of alumina,” **56**(192101), pp. 1149–1156.
- [3] COMPSON, C., N. ROSENBERGER, and M. SPREIJ (2013) “The Effect of SiO<sub>2</sub> and Na<sub>2</sub>O content on the Sintering Behavior of Calcined Specialty Aluminas for the Ceramics Industry,” *CFI-Ceramic Forum International*, **90**(3), pp. E17–E22.
- [4] COBLE, R. L. (1961) “Sintering crystalline solids,” *Journal of applied physics*, **32**(5), pp. 787–799.
- [5] ——— (1962) “Sintering alumina: effect of atmospheres,” *Journal of the American Ceramic Society*, **45**(3), pp. 123–127.
- [6] ——— (1962), “Transparent alumina and method of preparation,” .
- [7] JORGENSEN, P. J. and J. H. WESTBROOK (1964) “Role of Solute Segregation at Grain Boundaries During Finalâ€-Stage Sintering of Alumina,” *Journal of the American Ceramic Society*, **47**(7), pp. 332–338.
- [8] JORGENSEN, P. J. (1965) “Modification of sintering kinetics by solute segregation in Al<sub>2</sub>O<sub>3</sub>,” *Journal of the American Ceramic Society*, **48**(4), pp. 207–210.
- [9] LÜCKE, K. and K. DETERT (1957) “A quantitative theory of grain-boundary motion and recrystallization in metals in the presence of impurities,” *Acta Metallurgica*, **5**(11), pp. 628–637.
- [10] CAHN, J. W. (1962) “The impurity-drag effect in grain boundary motion,” *Acta metallurgica*, **10**(9), pp. 789–798.

- [11] JOHNSON, W. C. and R. L. COBLE (1978) “A Test of the Second-Phase and Impurity Segregation Models for MgO-Enhanced Densification of Sintered Alumina,” *Journal of the American Ceramic Society*, **61**(3–4), pp. 110–114.
- [12] ZUO, F., C. CARRY, S. SAUNIER, S. MARINEL, and D. GOEURIOU (2013) “Comparison of the microwave and conventional sintering of alumina: effect of MgO doping and particle size,” *Journal of the American Ceramic Society*, **96**(6), pp. 1732–1737.
- [13] BAE, S. I. and S. BAIK (1993) “Determination of critical concentrations of silica and/or calcia for abnormal grain growth in alumina,” *Journal of the American ceramic society*, **76**(4), pp. 1065–1067.
- [14] ——— (1993) “Sintering and grain growth of ultrapure alumina,” *Journal of Materials Science*, **28**(15), pp. 4197–4204.
- [15] HANDWERKER, C. A., P. A. MORRIS, and R. L. COBLE (1989) “Effects of chemical inhomogeneities on grain growth and microstructure in Al<sub>2</sub>O<sub>3</sub>,” *Journal of the American Ceramic Society*, **72**(1), pp. 130–136.
- [16] KAYSER, W. A., M. SPRISLER, C. A. HANDWERKER, and J. E. BLENDELL (1987) “Effect of a liquid phase on the morphology of grain growth in alumina,” *Journal of the American Ceramic Society*, **70**(5), pp. 339–343.
- [17] AHN, J. H., J. LEE, S. HONG, N. HWANG, and D. KIM (2003) “Effect of the Liquid-Forming Additive Content on the Kinetics of Abnormal Grain Growth in Alumina,” *Journal of the American Ceramic Society*, **86**(8), pp. 1421–1423.
- [18] HANSEN, S. C. and D. S. PHILLIPS (1983) “Grain boundary microstructures in a liquid-phase sintered alumina ( $\alpha$ -Al<sub>2</sub>O<sub>3</sub>),” *Philosophical Magazine A*, **47**(2), pp. 209–234.
- [19] HARMER, M. P. (1984) “Use of solid-solution additives in ceramic processing,” *Advances in ceramics*, **10**, p. 679.
- [20] BATEMAN, C. A., S. J. BENNISON, and M. P. HARMER (1989) “Mechanism for the role of magnesia in the sintering of alumina containing small amounts of a liquid phase,” *Journal of the American Ceramic Society*, **72**(7), pp. 1241–1244.
- [21] SONI, K. K., A. M. THOMPSON, M. P. HARMER, D. B. WILLIAMS, J. M. CHABALA, and R. LEVISETTI (1995) “Solute segregation to

- grain boundaries in MgO-doped alumina," *Applied physics letters*, **66**(21), pp. 2795–2797.
- [22] BENNISON, S. J. and M. P. HARMER (1983) "Effect of MgO solute on the kinetics of grain growth in Al<sub>2</sub>O<sub>3</sub>," *Journal of the American Ceramic Society*, **66**(5).
- [23] ——— (1990) "Effect of Magnesia Solute on Surface Diffusion in Sapphire and the Role of Magnesia in the Sintering of Alumina," *Journal of the American Ceramic Society*, **73**(4), pp. 833–837.
- [24] BAE, S. I. and S. BAIK (1994) "Critical concentration of MgO for the prevention of abnormal grain growth in alumina," *Journal of the American Ceramic Society*, **77**(10), pp. 2499–2504.
- [25] ROY, S. K. and R. L. COBLE (1968) "Solubilities of magnesia, titania, and magnesium titanate in aluminum oxide," *Journal of the American Ceramic society*, **51**(1), pp. 1–6.
- [26] DILLON, S. J., M. P. HARMER, and G. S. ROHRER (2010) "Influence of interface energies on solute partitioning mechanisms in doped aluminas," *Acta Materialia*, **58**(15), pp. 5097–5108.
- [27] DILLON, S. J. and M. P. HARMER (2007) "Multiple grain boundary transitions in ceramics: a case study of alumina," *Acta Materialia*, **55**(15), pp. 5247–5254.
- [28] ROHRER, G. S., M. AFFATIGATO, M. BACKHAUS, R. K. BORDIA, H. M. CHAN, S. CURTAROLO, A. DEMKOV, J. N. ECKSTEIN, K. T. FABER, and J. E. GARAY (2012) "Challenges in ceramic science: a report from the workshop on emerging research areas in ceramic science," *Journal of the American Ceramic Society*, **95**(12), pp. 3699–3712.
- [29] DILLON, S. J., M. TANG, W. C. CARTER, and M. P. HARMER (2007) "Complexion : A new concept for kinetic engineering in materials science," **55**, pp. 6208–6218.
- [30] SUMITA, S. and H. K. BOWEN (1988) "Effects of foreign oxides on grain growth and densification of sintered Al<sub>2</sub>O<sub>3</sub>," *Ceramic Powder Science II. Transactions Westerville, Oh., 1988,,* **1**, pp. 840–847.
- [31] SMOTHERS, W. J. and H. J. REYNOLDS (1954) "Sintering and grain growth of alumina," *Journal of the American Ceramic Society*, **37**(12), pp. 588–595.
- [32] CAHOON, H. P. and C. J. CHRISTENSEN (1956) "Sintering and Grain Growth of Alpha-Alumina," *Journal of the American Ceramic Society*, **39**(10), pp. 337–344.

- [33] LOUET, N., M. GONON, and G. FANTOZZI (2005) “Influence of the amount of Na<sub>2</sub>O and SiO<sub>2</sub> on the sintering behavior and on the microstructural evolution of a Bayer alumina powder,” *Ceramics International*, **31**(7), pp. 981–987.
- [34] JUDD, M., B. PLUNKETT, and M. POPE (1974) “The thermal decomposition of calcium, sodium, silver and copper (II) acetates,” *Journal of Thermal Analysis and Calorimetry*, **6**(5), pp. 555–563.
- [35] LAMBOTTE, G. and P. CHARTRAND (2013) “Thermodynamic modeling of the (Al<sub>2</sub>O<sub>3</sub>+Na<sub>2</sub>O), (Al<sub>2</sub>O<sub>3</sub>+Na<sub>2</sub>O+SiO<sub>2</sub>), and (Al<sub>2</sub>O<sub>3</sub>+Na<sub>2</sub>O+AlF<sub>3</sub>+NaF) systems,” *The Journal of Chemical Thermodynamics*, **57**, pp. 306–334.
- [36] BROWNMILLER, L. and R. BOGUE (1932) “System CaO-Na<sub>2</sub>O-Al<sub>2</sub>O<sub>3</sub>,” *Bureau of Standards Journal of Research*, **8**, pp. 289–307.
- [37] PABLOÁRGALAN, L. and W. R. FOSTER (1959) “Investigation of Role of Beta Alumina in the System Na<sub>2</sub>O-Al<sub>2</sub>O<sub>3</sub>-SiO<sub>2</sub>,” *Journal of the American Ceramic Society*, **42**(10), pp. 491–498.
- [38] RANKIN, G. A. and H. E. MERWIN (1916) “THE TERNARY SYSTEM CaO-Al<sub>2</sub>O<sub>3</sub>-MgO.” *Journal of the American Chemical Society*, **38**(3), pp. 568–588.
- [39] RIDGWAY, R. R., A. A. KLEIN, and W. J. O’LEARY (1936) “The Preparation and Properties of So-called α-Alumina,” *Transactions of the Electrochemical Society*, **70**(1), pp. 71–88.
- [40] DUNCAN, J. H. and W. E. C. CREYKE (1969) “The formation and stability of beta-Al<sub>2</sub>O<sub>3</sub> in alpha-Al<sub>2</sub>O<sub>3</sub> Ceramics,” *Trans. Brit. Ceram. Soc.*, pp. 137–144.
- [41] SUTORIK, A. C., S. S. NEO, D. R. TREADWELL, and R. M. LAINE (1998) “Synthesis of Ultrafine β-Alumina Powders via Flame Spray Pyrolysis of Polymeric Precursors,” *Journal of the American Ceramic Society*, **81**(6), pp. 1477–1486.
- [42] STEVENS, R. and J. G. P. BINNER (1984) “Structure, properties and production of β-alumina,” *Journal of materials science*, **19**(3), pp. 695–715.
- [43] CHRISTIE, J. R., A. J. DARNELL, and D. F. DUSTIN (1978) “Reaction of molten sodium carbonate with aluminum oxide,” *J. Phys. Chem.;(United States)*, **82**(1).

- [44] VRIES, R. C. and W. L. ROTH (1969) “Critical Evaluation of the Literature Data on Beta Alumina and Related Phases: I, Phase Equilibria and Characterization of Beta Alumina Phases,” *Journal of the American Ceramic Society*, **52**(7), pp. 364–369.
- [45] TERAI, R. and R. HAYAMI (1975) “Ionic diffusion in glasses,” *Journal of Non-Crystalline Solids*, **18**(2), pp. 217–264.
- [46] KWON, O. and G. L. MESSING (1990) “Kinetic Analysis of Solution-precipitation During Liquid-Phase Sintering of Alumina,” *Journal of the American Ceramic Society*, **73**(2), pp. 275–281.
- [47] KWON, O.-H. and G. L. MESSING (1991) “A theoretical analysis of solution-precipitation controlled densification during liquid phase sintering,” *Acta metallurgica et materialia*, **39**(9), pp. 2059–2068.
- [48] PARK, C. W. and D. Y. YOON (2000) “Effects of SiO<sub>2</sub>, CaO<sub>2</sub>, and MgO additions on the grain growth of alumina,” *Journal of the American ceramic society*, **83**(10), pp. 2605–2609.
- [49] DAY, D. E. and G. E. RINDONE (1962) “Properties of soda aluminosilicate glasses: I, refractive index, density, molar refractivity, and infrared absorption spectra,” *Journal of the American Ceramic Society*, **45**(10), pp. 489–496.
- [50] WU, G., E. YAZHENSKIKH, K. HACK, and M. MÜLLER (2015) “Viscosity model for oxide melts relevant to fuel slags. Part 2: The system SiO<sub>2</sub>-Al<sub>2</sub>O<sub>3</sub>-CaO-MgO-Na<sub>2</sub>O-K<sub>2</sub>O,” *Fuel Processing Technology*, **138**, pp. 520–533.
- [51] POPOVIC, A., L. BENCZE, J. KORUZA, B. MALIC, and M. KOSEC (2012) “Knudsen effusion mass spectrometric approach to the thermodynamics of Na<sub>2</sub>O-Nb<sub>2</sub>O<sub>5</sub> system,” *International Journal of Mass Spectrometry*, **309**, pp. 70–78.
- [52] GALLUP, J. (1935) “The transformation of aluminum oxide from the beta to the alpha form,” *Journal of the American Ceramic Society*, **18**(1–12), pp. 144–148.
- [53] BENNISON, S. J. and M. P. HARMER (1990) “A history of the role of MgO in the sintering of alpha-Al<sub>2</sub>O<sub>3</sub>,” in *Ceramic Transactions 7, Sintering of Advanced Ceramics* (C. A. Handwerker, J. E. Blendell, and W. A. Kaysser, eds.), Am. Ceram. Soc., Westerville, pp. 13–49.
- [54] HEUER, A. H. (1979) “The role of MgO in the sintering of alumina,” *Journal of the American Ceramic Society*, **62**, pp. 317–318.

- [55] PARK, C. W. and D. Y. YOON (2000) “Grain growth of alumina,” **609**(3), pp. 2605–2609.
- [56] SHANG, S., Y. WANG, D. KIM, and Z.-K. LIU (2010) “First-principles thermodynamics from phonon and Debye model: Application to Ni and Ni<sub>3</sub>Al,” *Computational Materials Science*, **47**(4), pp. 1040–1048.
- [57] WANG, Y., Z.-K. LIU, and L.-Q. CHEN (2004) “Thermodynamic properties of Al, Ni, NiAl, and Ni<sub>3</sub>Al from first-principles calculations,” *Acta Materialia*, **52**(9), pp. 2665–2671.
- [58] LIU, X. L., B. K. VANLEEUWEN, S. SHANG, Y. DU, and Z.-K. LIU (2015) “On the scaling factor in Debye–Grüneisen model: A case study of the Mg–Zn binary system,” *Computational Materials Science*, **98**, pp. 34–41.
- [59] SHANG, S., Y. WANG, and Z.-K. LIU (2007) “First-principles elastic constants of alpha- and theta-Al<sub>2</sub>O<sub>3</sub>,” *Applied Physics Letters*, **90**(10), pp. 101909–1–101909–3.
- [60] KRESSE, G. and J. FURTHMÜLLER (1996) “Efficiency of ab-initio total energy calculations for metals and semiconductors using a plane-wave basis set,” *Computational Materials Science*, **6**(1), pp. 15–50.
- [61] KRESSE, G. and D. JOUBERT (1999) “From ultrasoft pseudopotentials to the projector augmented-wave method,” *Physical Review B*, **59**(3), pp. 1758–1775.
- [62] BLÖCHL, P. (1994) “Projector augmented-wave method,” *Physical Review B*, **50**(24), p. 17953.
- [63] PERDEW, J. and Y. WANG (1992) “Accurate and simple analytic representation of the electron-gas correlation energy,” *Physical Review B*, **45**(23), p. 13244.
- [64] MONKHORST, H. and J. PACK (1976) “Special points for Brillouin-zone integrations,” *Physical Review B*, **13**(12), pp. 5188–5192.
- [65] ATKINSON, K. J. W., R. W. GRIMES, M. R. LEVY, Z. L. COULL, and T. ENGLISH (2003) “Accommodation of impurities in  $\alpha$ -Al<sub>2</sub>O<sub>3</sub>,  $\alpha$ -Cr<sub>2</sub>O<sub>3</sub> and  $\alpha$ -Fe<sub>2</sub>O<sub>3</sub>,” *Journal of the European Ceramic Society*, **23**(16), pp. 3059–3070.
- [66] GRIMES, R. W. (1994) “Solution of MgO, CaO, and TiO<sub>2</sub> in  $\alpha$ -Al<sub>2</sub>O<sub>3</sub>,” *Journal of the American Ceramic Society*, **77**(2), pp. 378–384.
- [67] LAGERLÖF, K. P. D. and R. W. GRIMES (1998) “The defect chemistry of sapphire ( $\alpha$ -Al<sub>2</sub>O<sub>3</sub>),” *Acta materialia*, **46**(16), pp. 5689–5700.

- [68] XIANG, X., G. ZHANG, X. WANG, T. TANG, and Y. SHI (2015) “A new perspective on the process of intrinsic point defects in  $\alpha$ -Al<sub>2</sub>O<sub>3</sub>,” *Physical Chemistry Chemical Physics*, **17**(43), pp. 29134–29141.
- [69] SARSAM, J., M. W. FINNIS, and P. TANGNEY (2013) “Atomistic force field for alumina fit to density functional theory,” *The Journal of chemical physics*, **139**(20), p. 204704.
- [70] MAO, H., O. FABRICHNAYA, M. SELLEBY, and B. SUNDMAN (2005) “Thermodynamic assessment of the MgO-Al<sub>2</sub>O<sub>3</sub>-SiO<sub>2</sub> system,” *Journal of Materials Research*, **20**(04), pp. 975–986.
- [71] SUBRAMANIAM, A., C. T. KOCH, R. M. CANNON, and M. RÜHLE (2006) “Intergranular glassy films: An overview,” *Materials Science and Engineering A*, **422**(1-2), pp. 3–18.
- [72] JAIN, A., S. ONG, G. HAUTIER, W. CHEN, W. RICHARDS, S. DACEK, S. CHOLIA, D. GUNTER, D. SKINNER, and G. CEDER (2013) “The Materials Project: A materials genome approach to accelerating materials innovation,” *Apl Materials*, **1**(1), p. 11002.
- [73] “Materials Project,” .  
URL <http://www.materialsproject.org>
- [74] GRAHAM, J. (1960) “Lattice spacings and colour in the system alumina - chromic oxide,” *Journal of Physics and Chemistry of Solids*, **12**, pp. 349–350.
- [75] BERGERHOFF, G., R. HUNDT, R. SIEVERS, and I. D. BROWN (1983) “The inorganic crystal structure data base,” *Journal of Chemical Information and Computer Sciences*, **23**(2), pp. 66–69.
- [76] KARLSRUHE, F. I. Z., “Inorganic Crystal Structure Database,” .
- [77] RAGHAVAN, V. (2010) “Al-Fe-O (Aluminum-iron-oxygen),” *Journal of Phase Equilibria and Diffusion*, **31**(4), p. 367.
- [78] CLARKE, D. R., T. M. SHAW, A. P. PHILIPSE, and R. G. HORN (1993) “Possible electrical double-layer contribution to the equilibrium thickness of intergranular glass films in polycrystalline ceramics,” *Journal of the American Ceramic Society*, **76**(5), pp. 1201–1204.
- [79] CLARKE, D. R. (1987) “On the equilibrium thickness of intergranular glass phases in ceramic materials,” *Journal of the American Ceramic Society*, **70**(1), pp. 15–22.
- [80] KINGERY, W. D. (2004) “Densification during sintering in the presence of a liquid phase. I. Theory,” *Journal of Applied Physics*, **30**1(1959).

- [81] LEE, S.-M. and S.-J. L. KANG (1998) “Theoretical analysis of liquid-phase sintering: Pore filling theory,” *Acta Materialia*, **46**(9), pp. 3191–3202.
- [82] SHAW, T. M. (1986) “Liquid redistribution during liquid-phase sintering,” *Journal of the American Ceramic Society*, **69**(1), pp. 27–34.
- [83] SVOBODA, J., H. RIEDEL, and R. GAEBEL (1996) “A model for liquid phase sintering,” *Acta Materialia*, **44**(8), pp. 3215–3226.
- [84] GERMAN, R. M. (2016) “Sintering trajectories: Description on how density, surface area, and grain size change,” *Jom*, **68**(3), pp. 878–884.
- [85] ISRAELACHVILI, J. (2011) *Intermolecular and Surface Forces*.
- [86] HSIEH, C., H. JAIN, and E. I. KAMITSOS (1996) “Correlation between dielectric constant and chemical structure of sodium silicate glasses,” *Journal of Applied Physics*, **80**(3), pp. 1704–1712.
- [87] LYON, K. (1942) “Calculation of surface tensions of glasses,” *Journal of The American Ceramic Society-Lyon*, **27**(6), pp. 25–28.
- [88] ZHANG, S. and S. H. GAROFALINI (2005) “Molecular dynamics computer simulations of the interface structure of calcium-alumino-silicate intergranular films between combined basal and prism planes of  $\alpha$ -Al<sub>2</sub>O<sub>3</sub>,” *Journal of the American Ceramic Society*, **88**(1), pp. 202–209.
- [89] TANAKA, I., H.-J. KLEEBE, M. K. CINIBULK, J. BRULEY, D. R. CLARKE, and M. RÜHLE (1993) “Calcium concentration dependence of the intergranular film thickness in silicon nitride,” *Journal of the American Ceramic Society*, **77**(4), pp. 911–914.
- [90] TOPLIS, M. J., D. B. DINGWELL, and T. LENCI (1997) “Peraluminous viscosity maxima in Na<sub>2</sub>O.Al<sub>2</sub>O<sub>3</sub>.SiO<sub>2</sub> liquids: The role of triclusters in tectosilicate melts,” *Geochimica et Cosmochimica Acta*, **61**(13), pp. 2605–2612.
- [91] LITTON, D. A. and S. H. GAROFALINI (1999) “Atomistic structure of sodium and calcium silicate intergranular films in alumina,” *Journal of Materials Research*, **14**(4), pp. 1418–1429.
- [92] STILLWELL, C. V. (1926) “The Color of the Ruby,” *J. Phys. Chem.*, **30**, pp. 1441–1466.

- [93] KUMMER, J. T. (1972) “Beta-alumina electrolytes,” in *Prog. Solid State Chemistry* (H. Reiss and J. O. McCaldin, eds.), 7 Pergamon Press, New York, pp. 141–175.
- [94] RAY, A. K. and E. C. SUBBARAO (1975) “Synthesis of sodium beta and beta” alumina,” **10**(6), pp. 583–590.
- [95] HANSEN, J. D., R. P. RUSIN, M.-H. TENG, and D. L. JOHNSON (1992) “Combined-Stage Sintering Model,” *Journal of the American Ceramic Society*, **75**(5), pp. 1129–1135.
- [96] PARK, S. J., J. M. MARTIN, J. F. GUO, J. L. JOHNSON, and R. M. GERMAN (2006) “Grain Growth Behavior of Tungsten Heavy Alloys Based on the Master Sintering Curve Concept,” **37**(November), pp. 9–16.
- [97] DIANTONIO, C. B., K. G. EWSUK, and D. BENCOE (2005) “Extension of Master Sintering Curve Theory to Organic Decomposition,” **2728**, pp. 2722–2728.
- [98] AGGARWAL, G., S.-J. PARK, I. V. I. SMID, and R. M. GERMAN (2007) “Master Decomposition Curve for Binders Used in Powder Injection Molding,” (Mdc).
- [99] BLAINE, D. C., S. J. PARK, P. SURI, and R. M. GERMAN (2006) “Application of work-of-sintering concepts in powder metals,” *Metallurgical and Materials Transactions A: Physical Metallurgy and Materials Science*, **37**(9), pp. 2827–2835.
- [100] SU, H. and D. L. JOHNSON (1996) “Master Sintering Curve: a practical approach to sintering,” *J. Am. Ceram. Soc*, **79**(12), pp. 3211 – 3217.
- [101] TATAMI, J., Y. SUZUKI, T. WAKIHARA, T. MEGURO, and K. KOMEYA (2006) “Control of Shrinkage during Sintering of Alumina Ceramics Based on Master Sintering Curve Theory,” *Key Engineering Materials*, **317-318**, pp. 11–14.
- [102] POUCHLY, V. and K. MACA (2009) “Master sintering curves of two different alumina powder compacts,” *Processing and Application of Ceramics*, **3**(4), pp. 177–180.
- [103] AMINZARE, M., F. GOLESTANI-FARD, O. GUILLON, M. MAZAHERI, and H. R. REZAIE (2010) “Sintering behavior of an ultrafine alumina powder shaped by pressure filtration and dry pressing,” *Materials Science and Engineering A*, **527**(16-17), pp. 3807–3812.

- [104] GUILLON, O. and J. LANGER (2010) “Master sintering curve applied to the Field-Assisted Sintering Technique,” *Journal of Materials Science*, **45**(19), pp. 5191–5195.
- [105] SHAO, W. Q., S. O. CHEN, D. LI, H. S. CAO, Y. C. ZHANG, and S. S. ZHANG (2009) “Prediction and control of microstructure evolution for sub-microscale beta-Al<sub>2</sub>O<sub>3</sub> during low-heating-rate sintering based on the master sintering curve theory,” *Journal of the European Ceramic Society*, **29**(1), pp. 201–204.
- [106] HARMER, M. P. and R. J. BROOK (1981) “Fast firing - Microstructural benefits,” *Trans. Brit. Ceram. Soc.*, **80**, p. 147.
- [107] WANG, S.-Y. and M.-H. TENG (2010) “Why a master sintering curve model can be applied to the sintering of nano-sized particles ?” *Journal of Alloys and Compounds*, **504**, pp. S336–S339.
- [108] REITERER, M. W. and K. G. EWSUK (2009) “An Analysis of Four Different Approaches to Predict and Control Sintering,” *Journal of the American Ceramic Society*, **92**, pp. 1419–1426.

# **Vita**

**Tobias Frueh**

The details of my childhood are so epic that if I tell you then I will have to kill you.